Challenge Journal of STRUCTURAL MECHANICS

Vol.1 No.3 (2015)

ISSN 2149-8024

TULPAR ACADEMIC PUBLISHING

Challenge Journal of Structural Mechanics

E-mail: *cjsmec@challengejournal.com*

Web page: *cjsmec.challengejournal.com*

TULPAR Academic Publishing
www.tulparpublishing.com

Challenge Journal of Structural Mechanics

CONTENTS

Performance-based fire protection of office buildings: A case study based on the collapse of WTC 7
Robert Korol, Frank Greening, Paul Heerema **96**

Dynamic analysis of pre-stressed elastic beams under moving mass using different beam models
Volkan Kahya **106**

Vertical ground motion influence on seismically isolated & unisolated bridges
Naim Eser Reyhanoğulları, Uğurhan Akyüz **117**

Envelope analysis equations for two-span continuous girder bridges
Daud Abdoh **124**

Warning time analysis for emergency response in Sakarya city, Turkey against possible Marmara earthquake
Hüseyin Serdar Küyük **134**

Minimum weight design of prestressed concrete beams by a modified grid search technique
İsmail Hakkı Çağatay **140**

Reliability of concrete box culverts designed for vertical loads
Sami Oğuzhan Akbaş, Süleyman Bahadır Yüksel **145**

Defining parameters for concrete damage plasticity model
Yusuf Sümer, Muharrem Aktaş **149**

TULPAR ACADEMIC PUBLISHING

Challenge Journal of Structural Mechanics

Performance-based fire protection of office buildings: A case study based on the collapse of WTC 7

Robert Korol [a,*], Frank Greening [b], Paul Heerema [a]

[a] *Department of Civil Engineering, McMaster University, Hamilton, Ontario L8S 4L7, Canada*
[b] *CTSNA Consulting, Kincardine, Ontario N2Z 2Y7, Canada*

ABSTRACT

This article points out the benefits of employing a performance based analysis approach for ascertaining the likelihood that travelling fires in an office building could induce a localized failure that might trigger its collapse. The case study chosen is Building 7 of the World Trade Center complex. Based on the parametric study undertaken, our findings were that the fire-protected steel floor beam, identified as the initiator of the cascade of events that followed, could not have done so, virtually under any circumstance.

ARTICLE INFO

Article history:
Received 2 July 2015
Accepted 29 July 2015

Keywords:
Collapse initiation
Steel structures
Fire loadings
Fire protection
Thermal analysis
Heat release rates

1. Introduction

While the collapse of the WTC twin towers on 9/11 received the lion's share of publicity and, and rightly so, considering the thousands who lost their lives that day, the mystery of why the 47 storey steel framed building, WTC 7, that collapsed several hours later remains to this day a mystery in several respects. Indeed, the official National Institute of Standards and Technology (NIST) report on that collapse was finally made public some seven years later in August 2008 (NIST, 2008a). Despite a couple of fuel tanks in the lower part of the building, the fires that precipitated collapse were claimed to have been caused by incendiary debris that catapulted from a plummeting WTC 1, severing columns and breaking windows on the south face of #7 during its collapse. These flaming remnants then caused combustible materials within office areas to burn and spread from area to area, weakening structural members and causing thermal expansion of an identified floor beam claimed to have dislodged the end of a particular girder resulting in "walk-off" its column support. The analysis by NIST purportedly then caused a locally unsupported column to buckle, precipitating an array of failures that very quickly cascaded into storey-by-storey collapses leading to global collapse of the entire structure.

Without laying blame on anyone, NIST attempted, through its strong working relationship with ASCE, to propose recommendations meant to ameliorate perceived weaknesses in building codes to avoid such tragedies from happening in future, with particular attention on ways to protect occupants and to preserve a structure's integrity when severe fires occur. This initiative resulted in NIST setting out 30 recommendations (NIST, 2008b) that ranged from developing "consensus standards and code provisions" to "academic, professional short-courses, and web-based training programs".

Since the collapse of WTC 7 represents the first time in history that a steel-framed building of significance succumbed to fire loadings alone, it has given rise to much discussion among those in structural engineering and architecture. A software package known as Fire Dynamics Simulator (FDS) was developed by NIST to incorporate the vast array of information that is needed to design or make predictions about an existing structure's safety when subjected to extreme fire loading events. However in either case, there are circumstances for which less sophistication is appropriate. A simplified

* *Corresponding author*. Tel.: +1-905-525-9140 ; Fax: +1-905-529-9688 ; E-mail address: korol@mcmaster.ca (R. Korol)
ISSN: 2149-8024 / DOI: http://dx.doi.org/10.20528/cjsmec.2015.07.028

performance-based design (PBD) fire analysis, based on the laws of thermodynamics and structural engineering principles, able to include several parameters, and which examines specific details of a design may require such an approach, consistent with the time-temperature models such as described by Petterson et al. (1976). In our view, such an approach is appropriate with the initiation of the collapse of Building 7, to be examined in this paper.

2. Basic Principles for Passive Resistance to Fire Loads

For many decades, structural engineers relied solely upon fire resistance ratings to ascertain the passive protection needed for a steel frame structure, however, since 9/11, an alternative method known as Performance-Based Design (PBD) has evolved, with the objective being to enhance our understanding of fire events in buildings and to employ methods, as needed, to provide protection. Frater and Kleinfeldt (2001) provide very useful introductory material in this regard. Other important papers appear in the Journal of Fire Sciences, of which the recent forum article by Quintiere and Williams (2014) suggests that the FDS method employed by NIST is "weak" in support of its rationale for the collapse. However, before launching into our own PBD analysis in connection with Building 7's collapse, a few basic principles and assumptions are presented as follows.

2.1. Heat energy release rate

When combustible materials burn in air, the heat release rate generated, Q_C, is expended both as that which causes a change in temperature in the gases themselves, known as sensible heat, Q_S, and radiant heat, Q_R, which directly causes heating of the adjacent surfaces that are exposed. As such, the heat generated from a prescribed amount of combustible material is given by Gray and Muller (1974) as:

$$Q_C = Q_{S+}Q_R\,. \tag{1}$$

For typical office fires, Q_S, the sensible heat term, is mostly dissipated by hot exhaust combustion gases that involve three parameters, one of which is the chemical reaction gas mass combustion rate m_G, a parameter which brings into play the conversion of a combustible material into a variety of gases released in the process. The equation that is applicable is given by;

$$Q_S = m_G c_p \Delta T\,, \tag{2}$$

where, c_p is the heat capacity of the combustion gases at constant pressure, and ΔT is the increase in the temperature of the combustion gases due to the fires from an initial temperature T_i to a higher temperature T_G.

The quantity m_G may be derived from a consideration of the combustible material consumption rate, modified by the addition of oxygen. Such materials generally consist of wood products or one form or other of plastic compounds. A common type of the latter may be represented by polystyrene, while the former is generally chemically equivalent to cellulose. In the case of polystyrene, its complete combustion in an oxygen environment is governed by the chemical formula;

$$[C_8H_8]_n + 10n[O_2] = 8n[CO_2] + 4n[H_2O]\,, \tag{3a}$$

where n denotes the number of moles associated with each compound, while the reaction of burning cellulose is governed by

$$[C_6H_{10}O_5]_n + 6n[O_2] = 6n[CO_2] + 5n[H_2O]\,. \tag{3b}$$

The combustion of 1 kg of polystyrene therefore requires 3 kg of oxygen (Eq. (3a)), while that for 1 kg of cellulose necessitates 1.19 kg of O_2 (Eq. (3b)).

However, since we are dealing with combustion reactions in air, each mole of O_2 supplied to the fire is accompanied by 3.76 moles of N_2, thus resulting in a reaction involving 5.1 kg of air per kg of the wood equivalent (cellulose). Since each kilogram of fuel adds 1 kg of mass to the reaction products, we have a total of 6.1 kg of combustion gases released per kg of cellulose burned. In the case of polystyrene, a similar mass balance computation will show that 14 kg of air is required for each kg of the plastic equivalent material resulting in 15 kg of combustion gases produced. Of course, we do not know the precise composition of the combustible materials in typical office building fires. Taking an average between the two materials considered, we may assume that the combustion of one kilogram of a wide variety of fuels is accompanied by a total release of about 10 kg of "exhaust" gases consisting of a mixture of CO_2, H_2O and N_2. It is reasonable to assume that for typical combustion gas mixtures, an average value for c_p of 1.2 kJ/kg°C is appropriate since the heat capacity for the above-mentioned gases is close to 1 kJ/kg°C, while that of water vapor is much higher at about 1.9 kJ/kg°C. It is important to mention that incomplete combustion may involve other gases that could be classified as toxic such as carbon monoxide and would therefore dissipate more heat than that which we have described above. Our primary objective, of course, is to utilize an expression for Q_R that will allow computation of the temperature of the steel floor beam alleged to have triggered collapse as a function of fire duration.

2.2. Radiant heat release rate

As noted in Eq. (1), Q_R can be determined once Q_C and Q_S have been identified. However, each of Q_R and Q_S depends on the temperature of the gases emanating from the flames within the prescribed compartments that are producing hot fires. Assuming that the combustibles are located below the partition height of typical cubicles, i.e. about ½ the floor-to-ceiling height, it is reasonable to conceive of the flames, on average reached that level, as noted in Fig. 1(a). Noted also, is a conceptual steel beam at the ceiling level above the work station. To determine the temperature at the flame tip interface, T_G, it is convenient to employ the Stefan-Boltzmann equation (Gray and Muller, 2008) that expresses the radiant heat release rate, Q_R, due to burning materials in a compartment fire, noted as:

$$Q_R = \epsilon A \sigma T_G^4 \,, \tag{4}$$

where ϵ is the emissivity of the gas, A is the surface area of hot gas to air interface (assumed at the top of a partition wall), σ is the Stefan-Boltzmann constant and T_G is the absolute temperature of the hot gases in degrees Kelvin. Since T_G–T_i is also equal to ΔT in Eq. (2), it follows that T_G can be computed if the other parameters in Eqs. (1) and (4) are specified. It will be assumed that T_i is room temperature of 20°C, i.e. 293 K, with other values being: σ = 5.67x10^{-8} W/m^{2}K^4, ϵ = 0.7 (Gray and Muller, 1974) while A is expressed in m^2.

Substituting the above into Eq. (1) results in the following quartic algebraic equation

$$\epsilon A \sigma T_G^4 + m_G c_p T_G = Q_C + m_G c_p T_i \,. \tag{5}$$

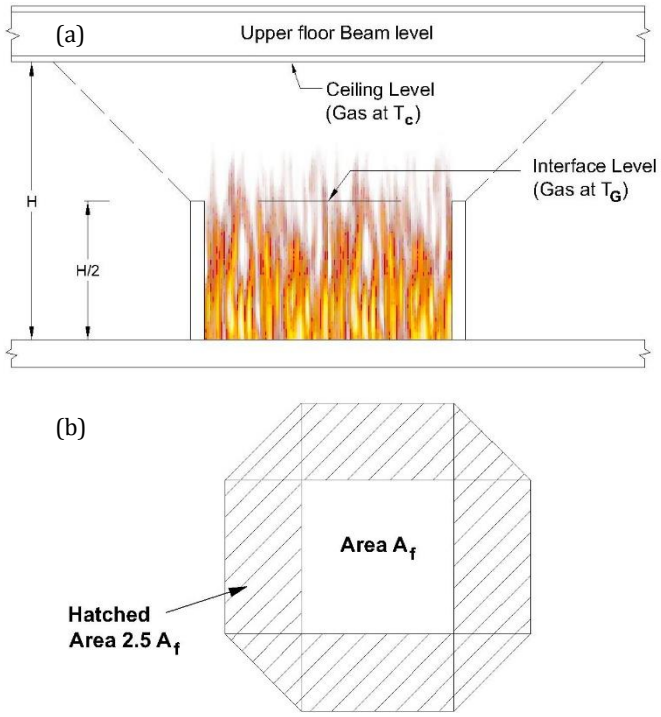

Fig. 1. Work area enclosure and surroundings (a) Conceived fires and impacted local domain (b) Footprints of floor and heated ceiling areas.

Once Q_C is selected, we can then solve for T_G. In that regard, we need both an estimate of the heat capacity of the combustible materials in question, and an estimate of the mass consumption rate during typical office fires in order to compute T_G. For the WTC fires, NIST estimated a duration of 25 minutes as being a reasonable estimate for a burn rate period (NIST, 2008c). Fundamental to computing a maximum temperature for a particular structural member is an estimate of the fuel load that is either typical of office buildings, or which has been established from earlier studies. Our focus is to employ the simple approach laid out through the set of equations quoted above to the floor beam that is claimed to have expanded sufficiently to cause column 79 at the 13th floor of WTC 7 to lose lateral support and hence trigger the collapse of the entire building. A sketch of the subject connection detail that is the focus of our case study is shown in Fig. 2 (Frankel Steel Limited, 1985a).

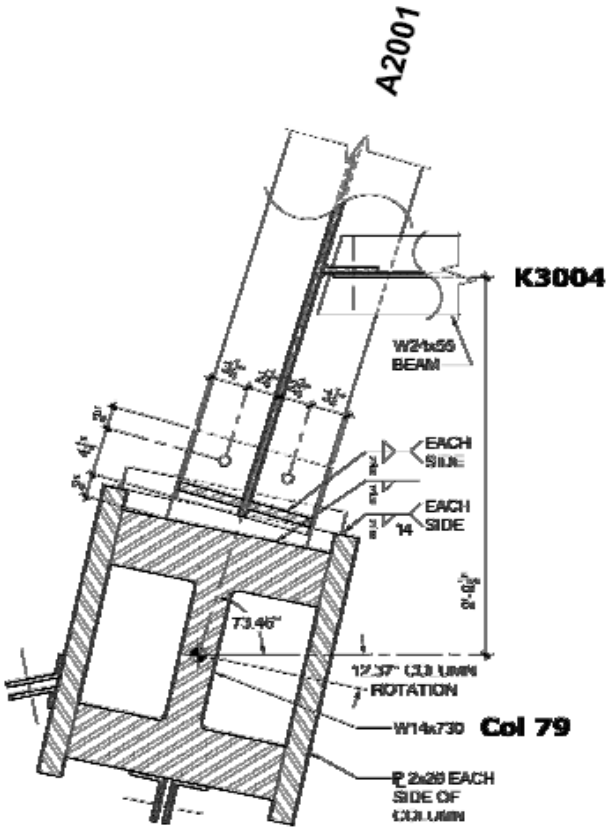

Fig. 2. Plan view of member intersection at column 79 (Data from Frankel Steel Limited, 1985b).

If we adopt the NIST heat of combustion average value of 16 MJ/kg, a value that virtually coincides with that of Feasey and Buchanan (2002) and the 25 minute burn period noted above, 22.5 kg/m^2 will generate a heat release rate, Q_C of 240 KW, the assumption being that the mass of combustible materials would diminish at a constant rate of 0.015 kg/sec. This appears to be a reasonable estimate, as the assumed amount of wood and plastic materials equivalent per m^2 is often cited as 20 kg/m^2 (typical for office buildings). On the other hand, this estimate, although reasonable for most office buildings, may not account for the unusual situation wherein excessively high fuel loading may result in some compartments versus that in others. Indeed, the NIST report indicates a loading of 32 kg/m^2 to be appropriate, a case to be examined, together with an even higher value of 45 kg/m^2. This latter estimate is included to account for the case of travelling fires, shown to augment the maximum temperature at a specific location by virtue of "far afield" fires (Jonsdottir et al., 2010). The heat release rates for these two fuel loadings are 341.3 and 480 KW respectively.

For each fuel loading, we will undertake an array of analyses for a 16.2 m (53 foot) long W24x55 floor beam, an end shown in Fig. 2, is alleged to have triggered the cascade of failures and noted in Frankel Steel's erection

drawing as K3004 (Frankel Steel Limited, 1985b). These will include unprotected steel cases, and three thicknesses of sprayed-on fire resisting material (SFRM), 13, 20 and 40 mm, representing NIST's estimate, an intermediate value, and 2 hours of fire protection (Jonsdottir et al., 2010) respectively, when subjected to the standard fire curve. The aim of such protection is to limit the maximum steel temperature from exceeding the critical value of 620°C (893°Kelvin), deemed to weaken such a member to the point of failure (Jowsey and Scott, 2014).

2.3. Combustion gas temperatures

As noted earlier, the hot gas temperatures, generated at the interface of the zones above and below the cubicle partition level (Fig. 1(a)) can be determined by solving Eq. (5). The results obtained are as follows: 22.5 kg/m^2 gives T_G = 1188°K; 32 kg/m^2 gives T_G = 1249°K, and 45 kg/m^2 results in a temperature of 1306°K, based on a constant heat release rate during a 25 minute period of combustion.

3. Ceiling Room Temperatures

The science of gas dynamics, fluid motion and heat transfer mechanisms indeed constitute a complex subject as they relate to burning fires in any environment. In the case of square-shaped cubicle-style compartments, we will assume that the heat generated from burning combustibles disperses outwards above such office enclosures at 45 degrees as noted in Fig. 1, with the result that the heat affected ceiling zone, A_c is 3.5 times the floor area, A_f, assumed to be square and of size H by H. This value is based on a ½ partition to ceiling height ratio, with triangles connecting the off-set rectangles at the corners of a rectangular office layout as noted in the figure. We further assume that the heat generated at the flame interface, A_f, is then uniformly spread out over that cubicle's heat affected ceiling area, A_c.

However, if several work stations are placed back-to-back, the ceiling area footprint, A_c, is reduced relative to A_f due to fanned overlapping of impacted ceiling areas. So, for example, an array of three aligned cubicles results in A_c/A_f = 2.67, while for five, the value is 2.4. In the case of WTC 7, it seems reasonable to assume that material in 3 work stations, aligned with the floor beam K3004 might have been burning intensely simultaneously. If we assume, therefore, that the radiated heat, Q_R, is fully absorbed by the ceiling, its temperature, T_C, based on Eq. (4) is then computed as $T_G/[\sqrt[4]{(A_c/A_f)}] = T_G/1.278$. So, for the three fuel loadings noted above, the 22.5 kg/m^2 case results in a ceiling temperature, T_C, of 930°K, the 32 kg/m^2 case gives a value of 977°K, while 45 kg/m^2 has a computed value of 1022°K. These computed temperatures provide an estimate of the temperatures that the structural members would experience for fires generating a constant heat release rate over a period of 25 minutes, after which burn out is presumed in a prescribed location. The steps to follow are the computation of steel temperatures of K3004 over time, followed by a determination of that member's elongation at the end of the burn period.

4. Unprotected Steel

In the case of heating of unprotected steel members, the following incremental equation is applicable (Jonsdottir et al., 2010):

$$\Delta T_S = \frac{F}{V}\frac{\Delta T}{\rho_S c_S}\{h_c(T_C - T_S) + \sigma\epsilon(T_C^4 - T_S^4\}, \quad (6)$$

in which T_S represents the steel's temperature at time t due to a fire, the temperature of which at the level of the ceiling is T_C, while the other quantities are defined as:

F/V, the member's section factor, computed for top flange embedment in floor slab concrete = 103 m^{-1} (W 24x 55 floor beam) represents an average mid-depth of the member, while ρ_S is the density of steel (7820 kg/m^3), c_S is its specific heat (460 J/kg K, where K being temperature in Kelvin), while h_C is the convective heat transfer coefficient (7 W/m^2 K (Oetelaar and Johnston, 2012)). The factors σ and ϵ are the Stefan-Boltzmann and emissivity constants respectively, having values of 5.67x10^{-8} W/m^2 K^4 and 0.7, noted earlier. In calculations to follow, $h_C(T_C - T_S)$ was much smaller than the $\sigma\epsilon(T_C^4 - T_S^4)$ term, but was included nonetheless for completeness.

4.1. Fuel loading = 22.5 kg/m²

This is the fuel loading case which most closely adheres to standards of combustible materials in office building compartments. Since the ceiling gas temperature was estimated to be 930°K, a time step of 1 minute (60 sec), following commencement of the fire, results in ΔT_{S1} to compute as 58.2 degrees (K or C). The steel temperature at the beginning of the next one minute step is therefore 351.2°K and results in ΔT_{S2} calculated to be 56.9°K. Finally, at the end of the fire period, ΔT_{S25} computes as 2.1°K, with the last time step of 60 sec. resulting in a final steel temperature of 925°K, or very near to the temperature of the ceiling gases. A plot of the steel temperature-time curve is shown in Fig. 3, and represents the lowest one (22.5 kg/m^2).

4.2. Fuel loading = 32 kg/m²

This is the case that NIST deemed to be the basis for their fire dynamics simulator (FDS) program. Since the burn time remains the same as in the previous case, i.e. 25 minutes, a higher ceiling exposure temperature was expected, and computed to be 977°K. A similar pattern of temperature steps resulted from calculations, with T_S computed to be 975.9°K. Its values are plotted in the figure as curve 32 kg/m^2.

4.3. Fuel loading = 45 kg/m²

We recognize that there are unusual circumstances in which moveable materials may be temporarily stored in certain areas of a building during renovations, repairs or for operational reasons and hence we doubled 22.5 kg scenario's value for such a possibility. In this case, T_C = 1022°K, with the maximum steel temperature reaching

1020°K. The uppermost curve in Fig. 3 shows a plot of this case. The final steel temperature for all three scenarios, i.e. between 650 and 750°C, exceeds the critical temperature of 620°C. As such, the computed carrying capacity of a given unprotected steel member would be exceeded and would likely cause a floor beam or girder to fail. A weakness in a connection detail, i.e. the way in which a member is joined to another, is oftentimes the reason for a localized failure and will be addressed subsequently.

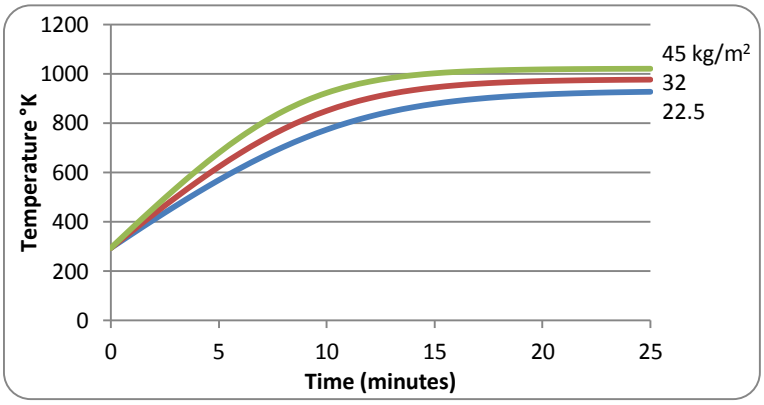

Fig. 3. Unprotected steel for a 25 minute fire.

5. Protected Steel

To protect steel framed buildings and their occupants from the devastating effects of a major fire, the standard procedure for design is to provide fire proofing material in accordance with prescriptive code requirements. Such protection was apparently applied to all structural members in WTC 7 and as such, the heating of the earlier identified floor beam is analyzed employing three thicknesses of SFRM (Sprayed-on Fire Resisting Material). For steel members that are provided with fire protection, the governing equation as noted by Jonsdottir et al. (2010) is:

$$\Delta T_s = \frac{F}{V d_i} \Delta t k_i (T_C - T_S) / \{\rho_S c_S + d_i \rho_i c_i F / 2V\}, \qquad (7)$$

where k_i is the thermal conductivity of the insulation, d_i its thickness, ρ_i the density, and c_i its specific heat. Appropriate values for low density spray type fire proofing as noted in the Steel Design Guide of AISC (Ruddy et al., 2002), were adopted in our computations as, k_i = 0.135 W/(m°K), ρ_i = 293 kg/m^3, and c_i = 754 J/(kg°K), while thicknesses offering a reasonable range of estimates are noted as, d_i = 13, 20 and 40 mm, respectively. As noted for the unprotected steel cases, those scenarios pertaining to protected steel assumed a constant high intensity 25 minute burn period. Note that the same step-by-step procedure noted for the unprotected steel scenarios was utilized for the same fuel load cases noted in the previous section. Fig. 4 shows the plotted temperature-time results for the three fuel loading and three insulation thickness cases noted above while Table 1 summarizes the peak temperature values of the floor beam after a 25 minute burn period.

5.1. Fuel loading = 22.5 kg/m², T_C = 930°K

In the case of the 13 mm SFRM scenario, it was found from Eq. (7) that the steel temperature, T_{S25} was 518°K after 25 minutes of a constant heat release rate from burning combustibles of 240 KW/m^2. When 20 mm of SFRM is employed, the steel temperature T_{S25} is reduced to 447°K, while the 40 mm thickness case was only 370°K. This latter circumstance appears to be consistent with the prescriptive standard for floor assemblies at the time that WTC 7 was constructed, i.e. at least a 2 hour fire rating (Jonsdottir et al., 2010). Clearly, such a temperature (97°C) would not pose a threat to a floor beam's ability to carry design dead and live loadings.

5.2. Fuel loading = 32 kg/m², T_C = 977°K

These cases appear to correspond to the fuel loading and burn time duration assumptions made in the NIST report (NIST, 2012). When 13 mm of SFRM is employed, the floor beam's average temperature gradually rises as shown in Fig. 4(b), reaching a maximum value of 535°K at the end of the 25 minute period. Increasing the protection to a thickness of 20 mm reduced the maximum temperature to 458°K while a value d_i = 40 mm lowered T_{S25} even further, i.e. down to 376°K. As noted, this case, and the other two noted in the sub-title are associated with a ceiling gas temperature of 977°K. The lowermost curve represents a most likely scenario, based on NIST information, assuming, of course, that the contractors and inspectors fulfilled their respective obligations during construction of the building.

5.3. Fuel loading = 45 kg/m², T_C = 1022°K

As noted earlier, the cases that follow under this heading are very extreme in the nature of combustible loadings, and would only be plausible in the most extraordinary circumstances. For the case of 13 mm SFRM, it turns out that the steel floor beam would have experienced a maximum temperature of 551°K.

By increasing the thickness of SFRM to 20 and 40 mm respectively, the time-temperature calculations indicate maximum values of T_S = T_{S25} = 469 and 381°K respectively.

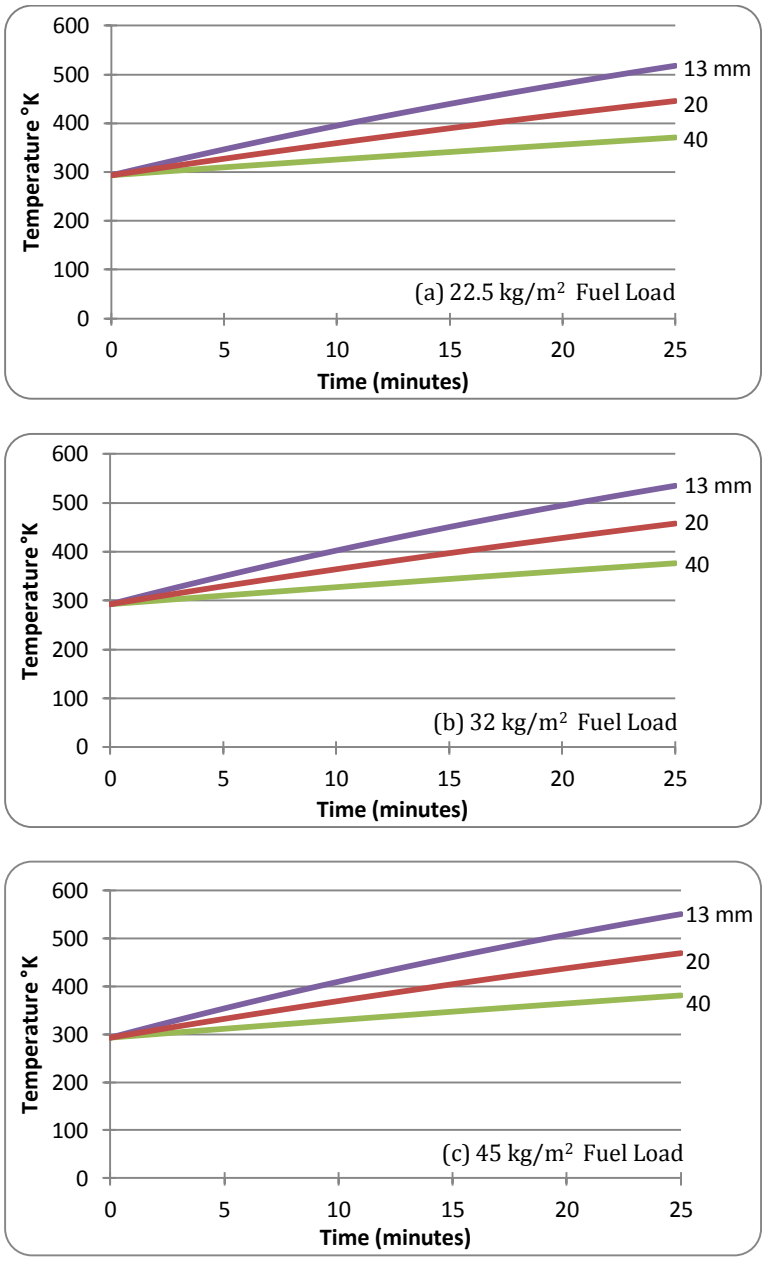

Fig. 4. SFRM protected steel (25 minute fire) - Results corresponding to T_C = 977°K.

Table 1. 25 minute burn period (protected steel).

Fuel Load	22.5 kg/m²			32 kg/m²			45 kg/m²		
T_G °K	1188			1249			1306		
T_C °K	930			977			1022		
d_i (mm)	13	20	40	13	20	40	13	20	40
T_{S25} °K	518	447	370	535	458	376	551	469	381

A summary of the key information associated with the above analyses is presented in Table 1. Note an interesting observation with respect to the degree of insensitivity existing among all cases having a prescribed thickness of protection to the fuel loading parameter. For example, doubling the fuel load from 22.5 to 45 kg/m² for the 13 mm case, increases the temperature of the floor beam by only 33°K, with an even more modest difference of 11°K obtained for 40 mm of insulation. If we make a supposition that NIST's estimate of the fire duration of 25 minutes might actually have been on the low side, what increase or decrease would be expected in steel temperatures for the previous cases described above for the same fuel loadings? After all, the duration time was

based on outside- the- building viewing, and hence it's of interest to postulate the possibility that travelling fires may have resided in one area for 30 minutes rather than 25. Doing such an analysis is very simple if one employs a PBD analysis approach, rather than NIST's FDS method which is costly and time-consuming.

6. Sensitivity of Steel Temperatures to Fire Duration Time

For a given amount of combustible materials, there is a fixed amount of heat energy available for release to the environment. Since the heat release rate of combustible materials is dependent on several factors, such as, the ventilation factor, material composition, moisture content, and the average heat of combustion etc., it's of interest to investigate the effect of increasing the burn time while maintaining the fuel combustion capacity at 16 MJ/kg. Indeed, NIST was uncertain about the time of intense burning and mentions in their report (NIST, 2008a) an estimated burn period of 20 to 30 minutes. An increase from 25 to 30 minutes will therefore result in a reduced heat release rate which is proportional to the burn time period.

Repeating the calculations, then, for a 30 minute period results in somewhat lower values of interface of flame-to-air layer temperatures, T_G, and hence correspondingly reduced values of ceiling gas temperatures, T_C. For example, Q_C reduces from 240 KJ/sec to 200 KJ/sec, with the consequence that T_G in Eq. (5) reduces from 1188°K to 1155°K for the 22.5 kg/m^2 cases. Similar reductions occur for the 32 and 45 kg/m^2 scenarios. Subsequent T_C values have proportional reductions since the ceiling to floor area factor $(8/3)^{0.25}$ is the same for all cases.

Fig. 5 presents plots of time-steel temperature curves for identical cases utilized in Fig. 4. As such, the curves look very similar with final temperatures being at the maximum values at the end of the burn period, in this case, 30 minutes. A summary of the same data shown in Table 1 is given in Table 2 for the 30 minute scenarios. Note that all final temperatures are slightly higher than their counterparts in Table 1, indicating that duration time weighs more heavily than does gas temperature. We do not claim that this trend would extend out to an infinite burn time, of course, since such a scenario would result in gas temperatures that would hardly exceed the ambient air temperature T_i.

7. Consequences of Steel Floor Beam Heating

Any of the scenarios above would have been theoretically possible, but many are highly unlikely. Those cases in which the steel is totally unprotected are meant to highlight the benefits achieved in providing insulating material that meets fire rating requirements. Since tenants in office buildings are generally free to utilize space in an unrestricted manner, it seems prudent to over-estimate, rather than to under-estimate fuel loads in fire engineering design. The 22.5 kg/m^2 fuel load is close to the norm in office buildings, the 32 value was judged by NIST to be more appropriate, and the 45 kg/m^2 value is clearly on the high side of what one would expect from the type of business and confidentiality attributes that are pertinent to tenancies involving finance and business, in general. In the case described, it is the 12th storey of WTC 7, i.e. beam K3004 on the 13th floor that was at issue.

It is well known that temperatures of structural steel in excess of about 893°K (620°C) will reduce member strength to a level below that which will support in-service loads. Hence, for the unprotected steel scenarios, Fig. 3 provides us with some insight into the times at which a hot fire consuming combustible materials would potentially result in failures. We noted earlier that such rates varied from a minimum of 0.015 kg/sec (22.5 kg/m^2), to the maximum value of 0.03 kg/sec (45 kg/m^2).

As observed from the figure, a potential failure state could be predicted after 18 minutes for the least amount of combustibles considered, 13 minutes for the middle case (32 kg/m^2), and 10 minutes for the 45 kg/m^2 case (uppermost curve). Since the fires were presumed to last for 25 minutes, we may conclude that floor beam K3004 would have failed. However, we have confidence that SFRM was applied properly, with adequate thicknesses, either for a 2 hour fire rating, or at least a one hour. The question therefore is the extent to which elongation of the noted floor beam occurred, and thence whether such expansion could have triggered a cascading sequence of failures that resulted in the entire building's demise. This matter is explored in the next section.

Table 2. 30 minute burn period (protected steel).

Fuel Load	22.5 kg/m^2			32 kg/m^2			45 kg/m^2		
T_G °K	1155			1217			1275		
T_C °K	904			952			998		
d_i (mm)	13	20	40	13	20	40	13	20	40
T_{S25} °K	542	465	381	561	479	388	580	492	394

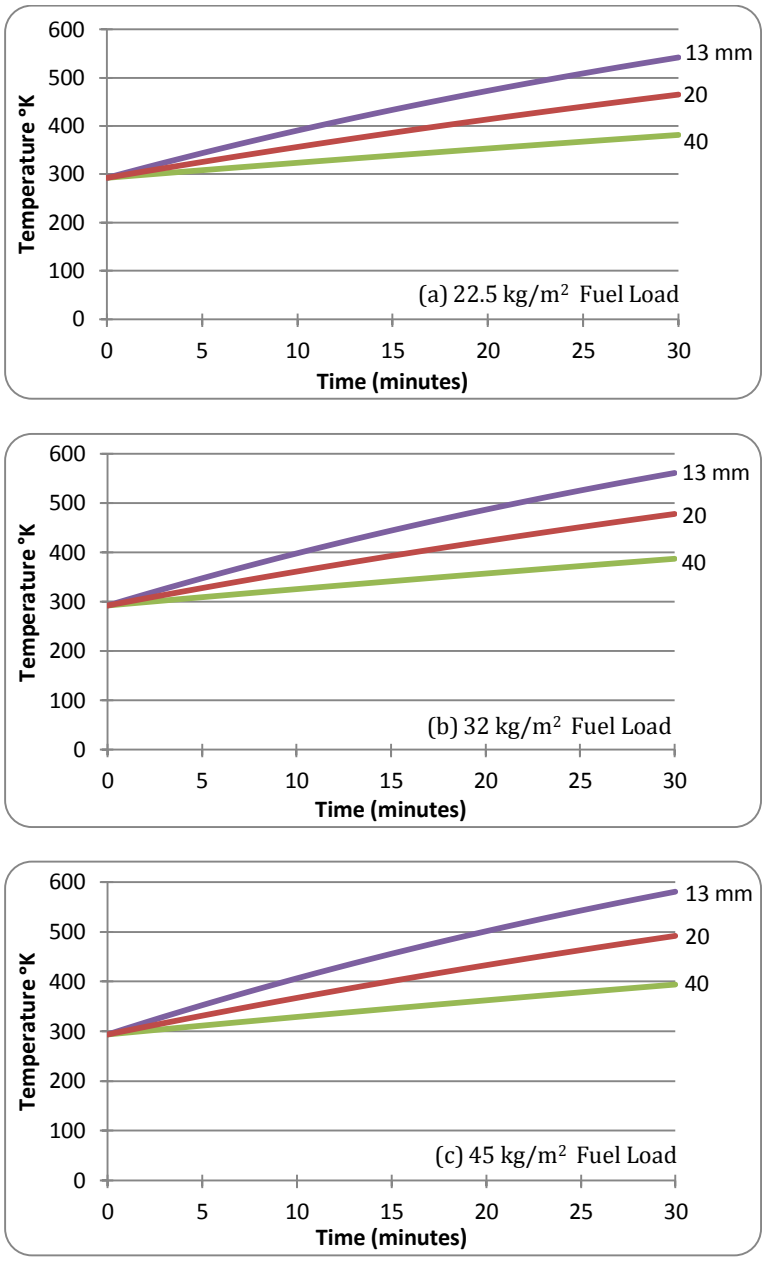

Fig. 5. SFRM protected steel (30 minute fire) - Results corresponding to T_C = 952°K.

8. Protected Steel Floor Beam Elongation

Fig. 4 shows plots of computed steel temperature curves for fire exposure times ranging over the full 25 minute period. As expected, the steel temperature is highest when the fuel load is at 45 kg/m^2, and the SFRM is 13 mm in thickness. However, at 25 minutes, we only obtain a temperature of 551°K (278°C) for this case, which is well below the critical strength value. When we examine the results for a 30 minute fire, the maximum temperature is 580°K for 13 mm of SFRM. Again, the issue of strength is not in question, but it does raise the issue of what thermal elongation would one obtain is such a scenario?

If a structural member is free to elongate as a consequence of a temperature increase, its elongation is simply the product of α_T, the coefficient of linear expansion with the associated length and change in temperature. In the case of the floor beam designated as K3004 in Frankel Steel's set of drawings, it was connected to girder A2001 (Fig. 2) that is alleged to have fallen off its shelf bearing plate support on column 79. The length of the floor beam was noted as being 53 feet (16.2 m). Roaming fires are unlikely to have the same intensity of temperature over that full length, but perhaps a half-length of 8.1 m would be a reasonable estimate. Assuming that displacement was essentially prevented at the perimeter column end yet unrestrained to move longitudinally at the girder end, the displacement would be 13.0 x 10^{-6} x 8.1 x ΔT °C (expressed in meters). For the case noted here for the 30 minute fire, and a 45 kg/m^2 fuel load ΔT = (580 – 293) °C = 287°C, and so the floor beam elongation computes as 30.2 mm (1.19 in). By taking the unrealistic circumstance that the fire caused the entire length of the beam to reach 580°K (307°C) results in the elongation being 60.4 mm (2.38"), a displacement << 152.4 mm (6"), i.e.

the half width of the bearing plate shelf angle support. Clearly, the lateral displacement of girder A2001 then would not have been in jeopardy since walk-off would require the web of the girder reaching beyond the bearing plate's edge (Fig. 2). Indeed, if one computes the elongation value of the one end free (col.79) and the other fully restrained, and employs the temperature increase suggested by NIST of 400°C over the full length, an unrestrained elongation of 84 mm (3.3 in) results, which is again much less that the walk-off lateral displacement of the girder.

9. Discussion

The assumptions noted above, pertaining to the walk-off displacement of girder A2001, presupposed that it was free to displace laterally on its bearing seat support. In fact, displacements noted above, would have been further reduced by virtue of the composite action of the girder with the floor slab that involved ¾" shear studs, spaced 18" along its length, as noted by Salvarinas (1986). It is well known by professional engineers who are involved in composite construction that shear studs rarely "shear off" when horizontal shear forces are activated by external loadings. They resist such forces by bending during conditions in which relative differences in horizontal displacements between a steel member and a concrete slab takes place, and as such are able to utilize their axial ultimate resistances. A similar situation exists for the floor beams. If a floor system employs composite construction, all major structural members in contact with a given floor slab will be connected with shear studs. If, as NIST indicated, such connectors were missing in girder A2001, such an omission might have been construed as a serious flaw in inspection. On the other hand, our calculations suggest that it matters not whether shear studs were or were not present – there would not have been walk-off in either instance.

For the girder A2001 to column 79 connection to even be a point of issue with respect to triggering collapse of WTC 7, it raises the question of whether such a detail is desirable or not. Fastening the girder by two bolts on its bottom flange to a welded seat support, seems to be inappropriate when large differential displacements are possible. It would appear to be more prudent to use a bearing seat support for erection purposes only, and employ double girder web angles, or equivalent, to secure that member to the column. Perhaps NIST might wish to recommend to steel structural code committees that for unusual forms of member layouts for floors (as was the case with WTC 7) a more robust form of connecting steel members to one another may be justified.

10. Conclusions

By applying the principles inherent in performance-based design to a localized area of a structure deemed to have been the trigger that resulted in cascading failures and thence collapse of a building (WTC 7), our investigation was meant to confirm or deny such a conclusion reached by NIST based on their costly and time-consuming Fire Dynamics Simulator software package. By employing basic thermodynamic principles, equations appropriate to heat flow, together with the combustion properties of materials of wood and plastic-based fuel sources, and normal structural and fire resisting material properties, we came to the opposite conclusion to that of NIST, namely that, regardless of fuel loading chosen, or which of three thicknesses of SFRM selected, fires alone could not have caused the commencement of the collapse of Building 7 at the location cited.

To arrive at such a conclusion, we made the key assumption, not challenged by NIST, that SFRM was employed and was intact during the fire event on 9/11. We also made the assumption that the heat release rates of fires were intense and constant for duration times of 25 or 30 minutes and impinged structural surfaces in the form of radiation and circulating hot gases with a constant temperature determined by the fuel load assumed and the distance of the ceiling above any given cubicle's partition height. At the end of the burn period, we concluded that floor beam K3004, located on the 13th floor, and which was exposed to hot flames in the 12 storey, either over its half length or even its full length, could not have elongated enough to cause a crucial walk-off of its adjoining girder. This conclusion is valid, whether or not shear connectors were present or not.

References

Feasey R, Buchanan A (2002). Post flashover fires for structural design. *Fire Safety Journal*, 37, 83-105.

Frankel Steel Limited (1985a). Erection Drawing E12.13, 7 World Trade Center.

Frankel Steel Limited (1985b). Fabrication Shop Drawing, 7 World Trade Center.

Frater G, Kleinfeldt C (2001). Fire protection of steel structures. *Advantage Steel*, 16-19.

Gray WA, Muller R (1974). Engineering Calculations in Radiative Heat Transfer, Pergamon Press, Oxford.

Jonsdottir AM, Stern-Gottfried J, Rein G (2010). Comparison of resultant steel temperatures using travelling fires and traditional methods: Case study for the informatics forum building. *Proceedings of the 12th International Interflam Conference*, Nottingham, U.K.

Jowsey A, Scott P (2014). Structural Steel Protection: Engineered Solutions, AkzoNobel International.

NIST (2008a). Final Report on the Collapse of World Trade Center Building 7. NIST-NCSTAR 1A, National Institute of Standards and Technology, Gaithersburg, Md.

NIST (2008b). Status of NIST's Recommendations Following the Federal Building and Fire Investigation of the World Trade Center Disaster, National Institute of Standards and Technology, Gaithersburg, Md.

NIST (2008c). Structural Fire Response and Probable Collapse Sequence of World Trade Center Building 7, NCSTAR 1-9, National Institute of Standards and Technology, Gaithersburg, Md.

NIST (2012). Changes to the NIST Reports of the Federal Building and Fire Investigation of the World Trade Center Disaster, NCSTAR 1-9, National Institute of Standards and Technology, Gaithersburg, Md.

Oetelaar TA, Johnston CR (2012). Determination of the convective heat transfer coefficient of hot air rising through terracotta flues. *CSME Transactions*, 36 (4), 413.

Quintierre JG, Williams FA (2014). Comments on the NIST investigation of the world trade center fires. *Journal of Fire Sciences*, 32, 281-291.

Petterson O, Magnusson S-E, Thor J (1976). Fire Engineering Design of Steel Structures. Swedish Institute of Steel Structures, Publication 50.

Ruddy J, Marlo JP, Ioannides SA, Alfawakhiri F (2002). Fire Resistance of Structural Steel Framing. AISC Steel Design Guide 19, Chicago, Il.

Salvarinas JJ (1986). Seven world trade center, New York, fabrication and construction aspects. *Canadian Structural Engineering Conference Proceedings*, Canadian Steel Construction Council, Willowdale, Ontario, pp 11-1 to 11-44.

Challenge Journal of Structural Mechanics

Dynamic analysis of pre-stressed elastic beams under moving mass using different beam models

Volkan Kahya *

Department of Civil Engineering, Karadeniz Technical University, 61080 Trabzon, Turkey

ABSTRACT

This study presents dynamic analysis of pre-stressed elastic beams under the action of moving mass loads by using Bernoulli-Euler, Rayleigh, and shear beam models. It is assumed the mass moves with a constant speed and is in continuous contact with the beam during its motion. Discrete equations of motion with time-dependent coefficients are obtained by using the assumed mode method for each beam models considered. Numerical calculations are made by Newmark method to obtain dynamic response of the beam. Effects of the pre-stressing force, rotatory inertia and transverse shear on the results for the dynamic deflection and bending moment of the beam and the interaction force between the mass and the beam are studied by depending on mass weight and speed of the moving mass.

ARTICLE INFO

Article history:
Received 11 May 2015
Accepted 26 June 2015

Keywords:
Moving mass
Pre-stressed beams
Bernoulli-Euler beam
Rayleigh beam
Shear beam

1. Introduction

Dynamics of beam structures under the action of moving loads and moving masses has been extensively studied for over a century in relation to the design of railroad tracks and bridges, and also machining processes. It is well known the inertia effects of a moving load cannot be ignored in the analysis when the mass weight of the moving load is large compared to the mass of the beam even if the speed of the moving mass is relatively small (Sadiku and Leipholz, 1987; Lee, 1996). Jeffcott (1929) was the first to consider inertial effects of both the moving load and the beam by the method of successive approximations. Frýba (1972) presented a comprehensive literature survey which contains analytical solutions to a large number of problems on the dynamic analysis of solids and structures under moving loads.

On the basis of the Bernoulli-Euler beam theory, Ting et al. (1974), Sadiku and Leipholz (1987), and Foda and Abduljabbar (1998) dealt with the moving mass problem of elastic beams by the use of Green's function. Stanišić (1985) derived an exact, closed form solution for a simple beam carrying a single moving mass by means of expansion of the eigenfunctions in a series. Akin and Mofid (1989) presented an analytical-numerical method to determine the dynamic behavior of beams with different boundary conditions carrying a moving mass. Assuming the solution in the form of a series in terms of eigenfunctions of the beam, they transformed the governing differential equation into a series of coupled ordinary differential equations. Esmailzadeh and Ghorashi (1995) studied the dynamic response of simply supported beams to uniform partially distributed moving masses. They found that increase in the load length makes more important the inertial effects of the moving mass. Michaltsos et al. (1996) considered the dynamic response of a simply supported beam under a moving mass with constant magnitude and speed. Using a series solution for the dynamic deflection of the beam in terms of normal modes, effects of the mass weight and speed of the moving load and other parameters were fully assessed. A new solution technique so-called discrete element method was proposed by Mofid and his co-workers for the moving mass problem of simple beams. They applied this method to Bernoulli-Euler beams with different boundary conditions under moving mass loads (Mofid and Akin, 1996; Mofid and Shadnam, 2000). Lee (1996) gave solution to the moving mass problem of an

* *Corresponding author*. Tel.: +90-462-3772631 ; Fax: +90-462-3772606 ; E-mail address: volkan@ktu.edu.tr (V. Kahya)
ISSN: 2149-8024 / DOI: http://dx.doi.org/10.20528/cjsmec.2015.06.018

elastic beam. He formulated the equation of motion in matrix form by using the Lagrangian approach and the assumed mode method. According to his study, there is a possibility of the loss of contact between the mass and the beam during the course of the motion. Another study pointing out separation between the mass and the beam was carried out by Lee (1998). He investigated the onset of the separation between the mass and the beam, and took into account its effect in calculating the interaction forces and the dynamic response of the beam. A technique using combined finite element and analytical methods for determining the dynamic responses of structures to moving loads was presented by Wu et al. (2001). Bilello et al. (2004) gave an experimental investigation of a simple beam under a moving mass. They designated a small-scale model to satisfy both static and dynamic similitude with a selected prototype bridge structure. More recently, Bowe and Mullarkey (2008) used a modal and finite element model to solve the problem of moving unsprung mass traversing a beam with different boundary conditions. They highlighted the drastic effects of omitting the convective acceleration terms from the formulation of unsprung moving mass problem.

On the basis of Timoshenko beam theory, Mackertich (1992) considered dynamic response of a simply supported beam excited by a moving mass. He reported that the effect of shear deformation and rotatory inertia are significant in determining the dynamic response of a beam subjected to a high-speed moving mass. The analysis of a Timoshenko beam under the action of moving mass was studied by Esmailzadeh and Ghorashi (1997). They solved the equations of motion by using a finite difference based algorithm. They investigated effects of shear deformation, rotatory inertia and the length of distributed load on the beam response. Yavari et al. (2002) analyzed the moving mass problem of Timoshenko beams using discrete element method. Lou et al. (2006) studied response of a Timoshenko beam to a moving mass by using the finite element method in which the inertial effects of the mass are incorporated into the finite element model. In a recent study, Kiani et al. (2009) presented a comprehensive assessment of design parameters such as dynamic deflection and bending moment of elastic beams subjected to a moving mass under different boundary conditions for Bernoulli-Euler, Timoshenko and higher-order shear beam theories. They gave detailed results to clarify effects of important parameters such as beam slenderness and boundary conditions as well as the change in weight and velocity of the moving mass.

Concrete bridges are common in the world and some of them were constructed by using pre-stressed concrete which works well for long-span bridges. Due to pre-tensioning, tensile stresses appearing in the beam are reduced to desired degree or vanished completely. The physical effect of pre-stressing is to provide an additional compressive stress in structures to resist tensile stresses occurring due to external loads (Chan and Yung, 2000). Although the effects of axial loading on the vibration characteristics of beams have been well investigated, studies related to the forced vibrations of beams with axial loading under moving loads are fewer. Frýba (1972) studied the response of a Bernoulli-Euler beam subjected to an axial force and a moving load. He gave analytical solutions of two different problems: First is the moving concentrated force problem in which inertia effect of the mass is ignored, and the second is the moving continuous load problem in which inertia effect of the mass is considered. Forced vibration of a viscoelastic Bernoulli-Euler beam subjected to an eccentric compressive force and a moving harmonic load was studied by Kocatürk and Şimşek (2006a), and was extended to the cases based on Timoshenko and higher-order beam theories in their subsequent papers (Kocatürk and Şimşek, 2006b; Şimşek and Kocatürk, 2007). In a recent study by Şimşek and Kocatürk (2009), dynamic analysis of an eccentrically pre-stressed damped beam under a moving harmonic concentrated force was studied by considering geometric nonlinearity. Kahya (2009) considered inertial effect of the moving mass in analyzing dynamic behavior of a simply supported pre-stressed elastic beam. According to the studies mentioned above, pre-stressing force has remarkable effect on the beam response. However, to the author's knowledge, inertial effects of moving loads on the dynamic response of beams with axial loading by also considering rotatory inertia and shear deformation have not been studied yet.

This study presents dynamic analysis of a simply supported elastic beam subjected to an axial load and a moving mass. Using the assumed mode method, discrete equations of motion with time-dependent coefficients is derived in matrix form for Bernoulli-Euler, Rayleigh and shear beam models to investigate effects of rotatory inertia and transverse shear on the beam response. The matrix equation of motion is solved numerically by using Newmark method. Effects of pre-stressing force, rotatory inertia and transverse shear on the dynamic deflection and bending moment of the beam and the interaction force between the mass and the beam are studied by depending on weight and speed of the moving mass and the beam length.

2. Definition of the Problem

A simply supported elastic beam shown in Fig. 1 is subjected to an axial force N at its ends and a mass M moving with a constant velocity v from left to right along the beam. At the beginning of motion ($t = 0$), the beam is at rest and it is assumed the moving mass keeps contact with the beam during its motion. The pre-stressed tendon is assumed straight and unbonded with the concrete. For a pre-stressed structure with a straight tendon, the structure is under the effect of an axial force and a bending moment at its ends. Chan and Yung (2000) reported that neglecting the moments due to pre-stressing in the governing equations is a reasonable approach. Therefore, only the axial pre-stressing force is considered in the governing equations of the system.

3. Mathematical Formulations

The dynamic behavior of the beam under the action of moving mass load is expressed by three different bam models: (a) Bernoulli-Euler beam model, (b) Rayleigh

beam model, and (c) Shear beam model. For each model, discrete governing equations of motion are derived by using the assumed mode method in subsequent sections.

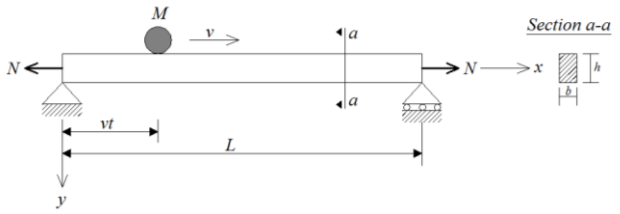

Fig. 1. Moving mass on a simply supported elastic beam with an axial load.

3.1. Bernoulli-Euler beam formulation

According to Bernoulli-Euler beam theory, governing differential equation of the beam shown in Fig. 1 can be written as follows.

$$EIy^{iv}(x,t) - Ny''(x,t) + cy'(x,t) + m\ddot{y}(x,t) = p(x,t), \quad (1)$$

where primes and dots represent derivatives with respect to spatial coordinate x and time t, respectively. $y(x,t)$ is the dynamic deflection, EI is the flexural rigidity, c is the damping coefficient and m is mass per unit length of the beam. N is the axial force (pre-stressing force) at the ends of the beam and $p(x,t)$ is transverse external force which can be defined as

$$p(x,t) = \{Mg - M[\ddot{y}(x,t) + 2v\dot{y}'(x,t) + v^2y''(x,t)]\}\delta(x,vt), \quad (2)$$

where g is the gravitational acceleration and $\delta(\dots)$ is the Dirac delta function.

In order to solve the governing differential equation given in Eq. (1), the solution $y(x,t)$ can be assumed as

$$y(x,t) = \sum_{i=1}^{\infty} \phi_i(x) q_i(t), \quad (3)$$

where $\phi_i(x)$ and $q_i(t)$ represent modal shape function and generalized coordinate at ith mode, respectively. Substituting Eq. (3) into Eq. (1) with considering Eq. (2) gives:

$$\sum_{i=1}^{\infty} EI\,\phi_i^{iv}(x)q_i(t) - \sum_{i=1}^{\infty} N\phi_i''(x)q_i(t) + \sum_{i=1}^{\infty} c\phi_i(x)\dot{q}_i(t) + \sum_{i=1}^{\infty} m\phi_i(x)\ddot{q}_i(t) = (Mg - M\sum_{i=1}^{\infty}[\phi_i(x)\ddot{q}_i(t) + 2v\phi_i'(x)\dot{q}_i(t) + v^2\phi_i''(x)q_i(t)])\delta(x - vt). \quad (4)$$

Multiplying each term of Eq. (4) by $\phi_j(x)$, integrating it with respect to x over the beam length, and interchanging the order of integration and summation gives

$$EI\sum_{i=1}^{\infty} q_i(t)\int_0^L \phi_i^{iv}(x)\phi_j(x)dx - N\sum_{i=1}^{\infty} q_i(t)\int_0^L \phi_i''(x)\phi_j(x)dx + c\sum_{i=1}^{\infty}\dot{q}_i(t)\int_0^L \phi_i(x)\phi_j(x)dx + m\sum_{i=1}^{\infty}\ddot{q}_i(t)\int_0^L \phi_i(x)\phi_j(x)dx = Mg\,\phi_j(vt) - M\sum_{i=1}^{\infty}\{\phi_i(vt)\phi_j(vt)\ddot{q}_i(t) + 2v\phi_i'(vt)\phi_j(vt)(t)\dot{q}_i(t) + v^2\phi_i''(vt)\phi_j(vt)q_i(t)\}, \quad (5)$$

Note that the following property of the Dirac delta function is considered to obtain right-hand side of Eq. (5)

$$\int_a^b f(x)\delta(x-\xi)dx = f(\xi) \quad (a < \xi < b). \quad (6)$$

For simply supported beams, modal shape function can be written as

$$\phi_i(x) = sin\frac{i\pi x}{L}. \quad (7)$$

Substituting Eq. (7) into Eq. (4), using modal orthogonality, and carrying out integrations yield the following matrix equation of motion with time-dependent coefficients.

$$M\ddot{q} + C\dot{q} + Kq = F, \quad (8)$$

where

$$M = I + \frac{2M}{mL}diag[\phi_i(x)]\Phi,$$

$$C = diag[2\xi_i\omega_{E,i}] + \frac{4M}{mL}vdiag[\phi_i(x)]\Phi',$$

$$K = diag[\omega_{E,i}^2] + \frac{2M}{mL}v^2diag[\phi_i(x)]\Phi'',$$

$$F = \frac{2Mg}{mL}\{\phi_1(vt)\phi_2(vt)\dots\phi_n(vt)^T\}, \quad (9)$$

where ξ_i and $\omega_{E,i}$ is the damping ratio and the circular natural frequency for ith mode, respectively. I is unit matrix, $diag(\dots)$ is a diagonal matrix. The matrix Φ can be defined as

$$\Phi = \begin{bmatrix} \phi_1(vt) & \phi_2(vt) & \cdots & \phi_n(vt) \\ \vdots & \ddots & & \vdots \\ \vdots & & \ddots & \vdots \\ \phi_1(vt) & \phi_2(vt) & \dots & \phi_n(vt) \end{bmatrix}. \quad (10)$$

For a Bernoulli-Euler beam with axial load, $\omega_{E,i}$ can be defined as

$$\omega_{E,i}^2 = \frac{EI}{m}\frac{i^4\pi^4}{L^4} + \frac{N}{m}\frac{i^2\pi^2}{L^2}, \quad i = 1, 2, \dots, n, \quad (11)$$

where n is total number of modes considered in the analysis. Bending moment for Bernoulli-Euler beam can be expressed by

$$M(x,t) = -EIy''(x,t). \quad (12)$$

3.2. Rayleigh beam formulation

Rayleigh beam model considers only rotatory inertia of the beam. The governing differential equation can thus be written as

$$EIy^{iv}(x,t) - Ny''(x,t) + c\dot{y}(x,t) - mr^2\ddot{y}''(x,t) + m\ddot{y}(x,t) = p(x,t)\,. \quad (13)$$

Here, $r = \sqrt{\pi I/A}$ denotes the radius of gyration where I and A are the second moment of area and cross-sectional area of the beam, respectively.

Assuming the solution $y(x,t)$ as given in Eq. (3) and following the same procedure just described for Bernoulli-Euler beams yields

$$M\ddot{q} + C\dot{q} + Kq = F\,, \quad (14)$$

where

$$M = diag\left[\mu_{R,i}\right] + \frac{2M}{mL}diag[\phi_i(x)]\Phi\,,$$

$$C = diag\left[2\xi_i\omega_{R,i}\right] + \frac{4M}{mL}v\,diag[\phi_i(x)]\Phi'\,,$$

$$K = diag\left[\omega_{E,i}^2\right] + \frac{2M}{mL}v^2 diag[\phi_i(x)]\Phi''\,,$$

$$F = diag\,\frac{2Mg}{mL}\{\phi_1(vt)\phi_2(vt)\ldots\phi_n(vt)^T\}\,, \quad (15)$$

where

$$\mu = 1 + \frac{i^2\pi^2 r^2}{L^2}\ ,\ \omega_{R,i}^2 = \frac{\omega_{E,i}^2}{\mu_{R,i}}\ ,\ i = 1,2,\ldots.,n\ , \quad (16)$$

which is the circular natural frequency for a Rayleigh beam with axial load. Bending moment of a Rayleigh beam is also expressed by Eq. (12).

3.3. Shear beam formulation

When only the effect of transverse shear on the dynamic behavior of the beam is considered, the following couple of governing differential equations can be written.

$$m\ddot{y}(x,t) + c\dot{y}(x,t) - kAG[y''(x,t) - \theta'(x,t)] - Ny''(x,t) = p(x,t)\,,$$

$$EI\theta''(x,t) + kAG[y'(x,t) - \theta(x,t)] = 0\,, \quad (17)$$

where k is the shear correction factor that depends on the shape of the cross-section of the beam, G is shear modulus and $\theta(x,t)$ is the rotation of the cross-section of the beam.

Solutions for the dynamic deflection $y(x,t)$ and the rotation $\theta(x,t)$ can be assumed as

$$y(x,t) = \sum_{i=1}^{\infty}\phi_i(x)q_i(t)\ ,\ \theta(x,t) = \sum_{i=1}^{\infty}\psi_i(x)s_i(t)\,, \quad (18)$$

where $q_i(t)$ and $s_i(t)$ are generalized coordinates, and $\phi_i(t)$ and $\psi_i(t)$ are modal shape functions which can be defined as

$$\phi_i(x) = sin\frac{i\pi x}{L}\ \ ,\ \theta\psi_i(x) = cos\frac{i\pi x}{L}\,, \quad (19)$$

for simply supported beams. Substituting Eq. (18) into Eq. (17) gives

$$m\sum_{i=1}^{\infty}\ddot{q}_i(t) + c\sum_{i=1}^{\infty}\phi_i(x)\dot{q}_i(t) - kAG[\sum_{i=1}^{\infty}\phi_i''(x)q_i(t) - \sum_{i=1}^{\infty}\psi_i'(x)s_i(t)] - N\sum_{i=1}^{\infty}\phi_i''(x)q_i(t) = (Mg - M\sum_{i=1}^{\infty}[\phi_i(x)\ddot{q}_i(t) + 2v\phi_i'(x)\dot{q}_i(t) + v^2\phi_i''(x)q_i(t)])\delta(x - vt)\,,$$

$$EI\sum_{i=1}^{\infty}\psi_i''(x)s_i(t) + kAG[\sum_{i=1}^{\infty}\phi_i'(x)q_i(t) - \sum_{i=1}^{\infty}\psi_i'(x)s_i(t)\,] = 0\,. \quad (20)$$

Multiplying the first equation of (20) by $\phi_j(x)$ and the second by $\psi_j(x)$, integrating them over the beam length, and interchanging the order of integration and summation yields

$$m\sum_{i=1}^{\infty}\ddot{q}_i(t)\int_0^L\phi_i(x)\,\phi_j(x)dx + c\sum_{i=1}^{\infty}\dot{q}_i(t)\int_0^L\phi_i(x)\,\phi_j(x)dx - kAG\left[\sum_{i=1}^{\infty}q_i(t)\int_0^L\phi_i''(x)\,\phi_j(x)dx - \sum_{i=1}^{\infty}s_i(t)\int_0^L\psi_i'(x)\,\phi_j(x)dx\right] - N\sum_{i=1}^{\infty}q_i(t)\int_0^L\phi_i''(x)\,\phi_j(x)dx = Mg\,\phi_j(vt) - M\sum_{i=1}^{\infty}\{\phi_i(vt)\phi_j(vt)\ddot{q}_i(t) + 2v\phi_i(vt)\phi_j(vt)\dot{q}_i(t) + v^2\phi_i''(vt)\phi_j(vt)q_i(t)\}\,,$$

$$EI\sum_{i=1}^{\infty}s_i(t)\int_0^L\psi_i''(x)\,\psi_j(x)dx + kAG\left[\sum_{i=1}^{\infty}q_i(t)\int_0^L\phi_i'(x)\,\psi_j(x)dx - \sum_{i=1}^{\infty}s_i(t)\int_0^L\psi_i'(x)\,\psi_j(x)dx\right] = 0\,. \quad (21)$$

Substituting Eq. (19) into Eq. (21), carrying out integrals, and using modal orthogonality, the following coupled matrix equations of motion with time-dependent coefficients can be obtained.

$$\left\{I + \frac{2M}{ml}diag[\phi_i]\Phi\right\}\ddot{q} + \left\{diag\left[2\xi_i\omega_{s,i}\right] + \frac{4M}{mL}v\,diag[\phi_i(x)]\Phi'\right\}\dot{q} + \left\{diag\left[\frac{N+kAG}{m}\frac{i^2\pi^2}{L^2}\right] + \frac{2M}{mL}v^2 diag[\phi_i(x)]\Phi''\right\}q - diag\left[\frac{kAG}{m}\frac{i\pi}{L}\right]s = F\,,$$

$$diag\left[\frac{kAG}{m}\frac{i\pi}{L}\right]q - diag\left[\frac{EI}{m}\frac{i^2\pi^2}{L^2} + \frac{kAG}{m}\right]s = 0\,. \quad (22)$$

From the second equation of (22)

$$s = \frac{diag\left[\frac{kAGi\pi}{m\ L}\right]}{diag\left[\frac{EIi^2\pi^2}{m\ L^2}+\frac{kAG}{m}\right]} q \,. \tag{23}$$

Using Eq. (23) into the first equation of (22), after some arrangements, the following matrix equation of motion can be obtained in terms of q.

$$M\ddot{q} + C\dot{q} + Kq = F \,, \tag{24}$$

where

$$M = I + \frac{2M}{mL} dia[\phi_i(x)]\Phi \,,$$

$$C = diag\left[2\xi_i\omega_{s,i}\right] + \frac{4M}{mL} v\, diag[\phi_i(x)]\Phi' \,,$$

$$K = diag\left[\omega_{s,i}^2\right] + \frac{2M}{mL} v^2 diag[\phi_i(x)]\Phi'' \,,$$

$$F = \frac{2Mg}{mL}\ \{\phi_1(vt)\ \phi_2(vt) \dots\ \phi_n(vt)^T\} \,, \tag{25}$$

where $\omega_{s,i}$ is the circular natural frequency for a shear beam with axial load and can be defined as

$$\omega_{s,i}^2 = \frac{1}{1+\frac{EI}{kAG}\frac{i^2\pi^2}{L^2}} \left\{\left(1+\frac{N}{kAG}\right)\frac{EI}{m}\frac{i^4\pi^4}{L^4} + \frac{N}{m}\frac{i^2\pi^2}{L^2}\right\} , i = 1, 2, \dots, n \,. \tag{26}$$

Bending moment for a shear beam can be expressed by

$$M(x,t) = -EI\theta'(x,t) \,. \tag{27}$$

4. Numerical Results

Since matrix equations of motion given by Eq. (8) for Bernoulli-Euler beam, Eq. (14) for Rayleigh beam and Eq. (24) for shear beam have time-dependent coefficients, a numerical solution algorithm is required for solution. In this study, Newmark method is employed to obtain dynamic deflection of the beam with axial load under moving mass. Once the dynamic deflection is obtained, the bending moment can easily be obtained by using Eq. (12) for Bernoulli-Euler and Rayleigh beams and Eq. (27) for shear beam.

The interaction (contact) force between the moving mass and the beam can be calculated by

$$F_c = Mg - M[\ddot{y}(x,t) + 2v\dot{y}'(x,t) + v^2 y''(x,t)]_{x=vt} \,, \tag{28}$$

which is defined to be positive if the force acting on the beam is pointing downward, i.e., in the positive y direction. Changing sign of the contact force from positive to negative would indicate that the mass separated from the beam (Lee, 1996).

Numerical calculations are made for n=10 modes, and the parameters of the beam are assumed to be E=35 GPa, v=0.2, m=1500 kg/m, b=0.4 m, h=0.4 m, and k=5/6 (Şimşek and Kocatürk, 2007). The damping ratio (ξ) is considered as 2.5% for all vibration modes.

Comparison of fundamental frequency of the beam for various slenderness ratios L/h according to different beam models is given in Table 1. Axial force is normalized by $N_{cr} = \pi^2 L^2/EI$ which is the critical buckling force for simply supported elastic beams. As seen in Eqs. (11), (16) and (26) which express natural frequencies for the considered beam models; the axial force has a direct effect on the natural frequency of the beam. As the axial force increases in tension, the fundamental frequency increases, too. On the other hand, the fundamental frequency decreases with increasing the axial force in compression. The latter case is called as the compression softening which can be explained as reduction in beam stiffness due to the pre-stressing (Chan and Yung, 2000; Şimşek and Kocatürk, 2007). In Table 2, critical velocities of the moving mass, which is defined as $v_{cr} = \omega_1 L/\pi$, are given for considered beam models and various L/h values. Variation of the critical velocity with the normalized axial force is similar to that of the fundamental frequency. From Tables 1 and 2, and Figs. 2 and 3, it can be said that shear beam model always gives smaller fundamental frequency and critical velocity in comparison to the other beam models when the slenderness ratio L/h of the beam is small

Table 1. Comparison of fundamental frequencies of the beam according to different beam models.

N/N_{cr}	$\omega_1/2\pi$ (Hertz)								
	L/h=5			L/h=10			L/h=20		
	BE	*R*	*S*	*BE*	*R*	*S*	*BE*	*R*	*S*
-1.0	-	-	-	-	-	-	-	-	-
-0.8	24.78	24.38	23.12	6.20	6.17	6.09	1.55	1.55	1.54
-0.6	35.05	34.49	33.10	8.76	8.73	8.63	2.19	2.19	2.18
-0.4	42.93	42.24	40.70	10.73	10.69	10.59	2.68	2.68	2.67
-0.2	49.57	48.77	47.09	12.39	12.34	12.23	3.10	3.09	3.09
0.0	55.42	54.53	52.71	13.85	13.80	13.68	3.46	3.46	3.45
0.2	60.68	59.74	57.79	15.18	15.11	14.98	3.79	3.80	3.78
0.4	65.56	64.51	62.45	16.34	16.32	16.19	4.10	4.09	4.09
0.6	71.10	69.00	66.79	17.52	17.45	17.31	4.38	4.38	4.37
0.8	74.34	73.15	70.87	18.59	18.51	18.35	4.65	4.64	4.63
1.0	78.36	77.11	74.72	19.59	19.51	19.35	4.90	4.89	4.88

Table 2. Comparison of critical velocities of the moving mass according to different beam models.

N/N_{cr}	v_{cr} (m/s)								
	L/h=5			L/h=10			L/h=20		
	BE	*R*	*S*	*BE*	*R*	*S*	*BE*	*R*	*S*
-1.0	-	-	-	-	-	-	-	-	-
-0.8	247.83	243.84	231.20	124.00	123.40	121.80	62.00	62.00	61.60
-0.6	350.52	344.87	331.01	175.20	174.60	172.60	87.6.0	87.60	87.20
-0.4	429.27	422.40	406.99	214.60	213.80	211.80	107.20	107.20	106.80
-0.2	495.66	487.79	470.94	247.80	246.80	244.60	124.00	123.60	123.60
0.0	554.18	545.26	527.14	277.00	276.00	273.60	138.40	138.40	138.00
0.2	606.18	597.41	578.01	303.60	302.20	299.60	151.60	152.00	151.20
0.4	655.60	645.07	624.56	326.80	326.40	323.80	164.00	163.60	163.60
0.6	701.04	689.95	667.79	350.40	349.00	346.20	175.20	175.20	174.80
0.8	743.40	731.50	708.70	371.80	370.20	367.00	186.00	185.60	185.20
1.0	783.60	771.10	747.20	391.80	390.20	387.00	196.00	195.60	195.20

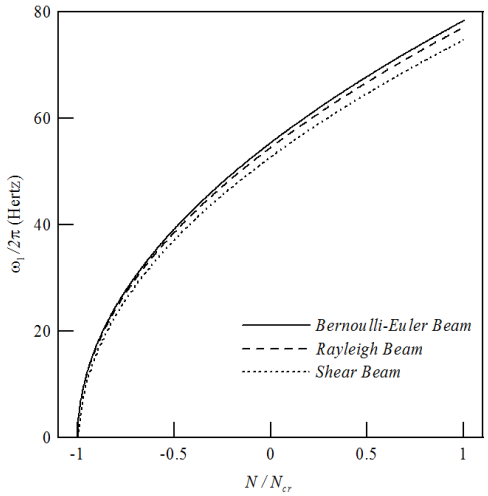

Fig. 2. Fundamental frequency of the beam vs. the normalized axial force for different beam models (L/h=5).

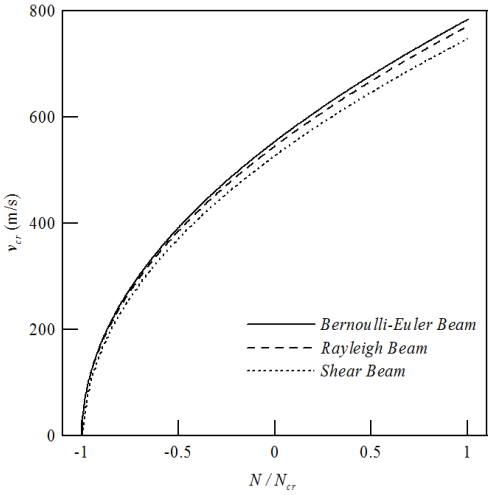

Fig. 3. Critical velocity of the moving mass vs. the normalized axial force for different beam models (L/h=5).

Figs. 4(a-b) show variation of maximum dynamic deflection and bending moment of the beam at its midspan with dimensionless velocity of the moving mass for Bernoulli-Euler beam, L/h=20 and M/mL=0.15, respectively.

When the axial compressive force increases, both the deflection and the bending moment increase because of the compression softening effect. On the contrary, the deflection and the bending moment decrease with increasing the axial force in tension.

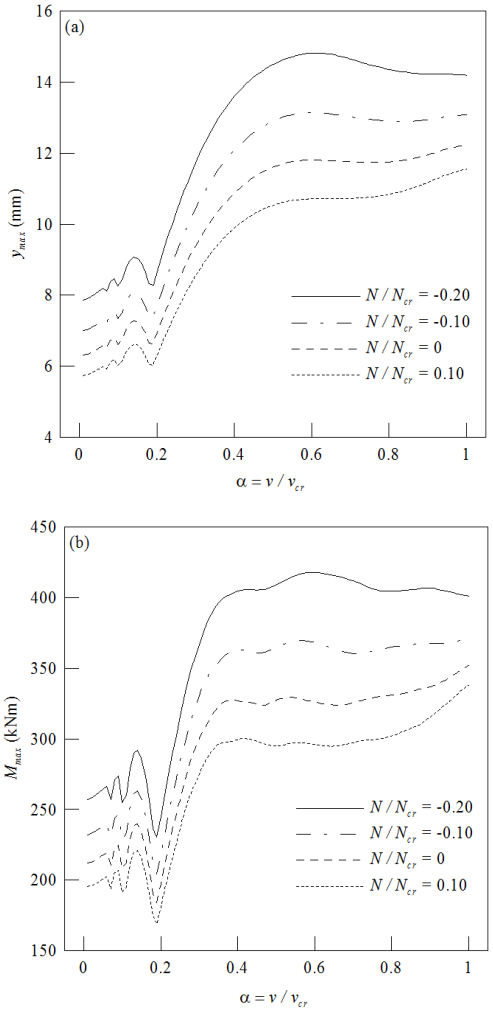

Fig. 4. Maximum dynamic response of the beam at its midspan vs. dimensionless velocity of the mass for different pre-stressing forces; (a) Deflection; (b) Bending moment (L/h=20, M/mL=0.15).

In Figs. 5 and 6, variation of maximum dynamic deflection and bending moment response of the beam with the dimensionless velocity for different beam models is shown for N/N_{cr}=-0.10, M/mL=0.15 and L/h=5, 10, 15 and 20. According to Fig. 5, rotatory inertia has almost no effect on deflection response of the beam at its midspan. However, shear deformation affects the midspan deflection considerably for shorter beams. Midspan deflections increase with increasing the slenderness ratio L/h. Deflection curves come closer to each other with increasing L/h since effect of shear deformation disappears for slender beams. According to Fig. 6, shear deformation has little effect on the bending moment response compared to the deflection response.

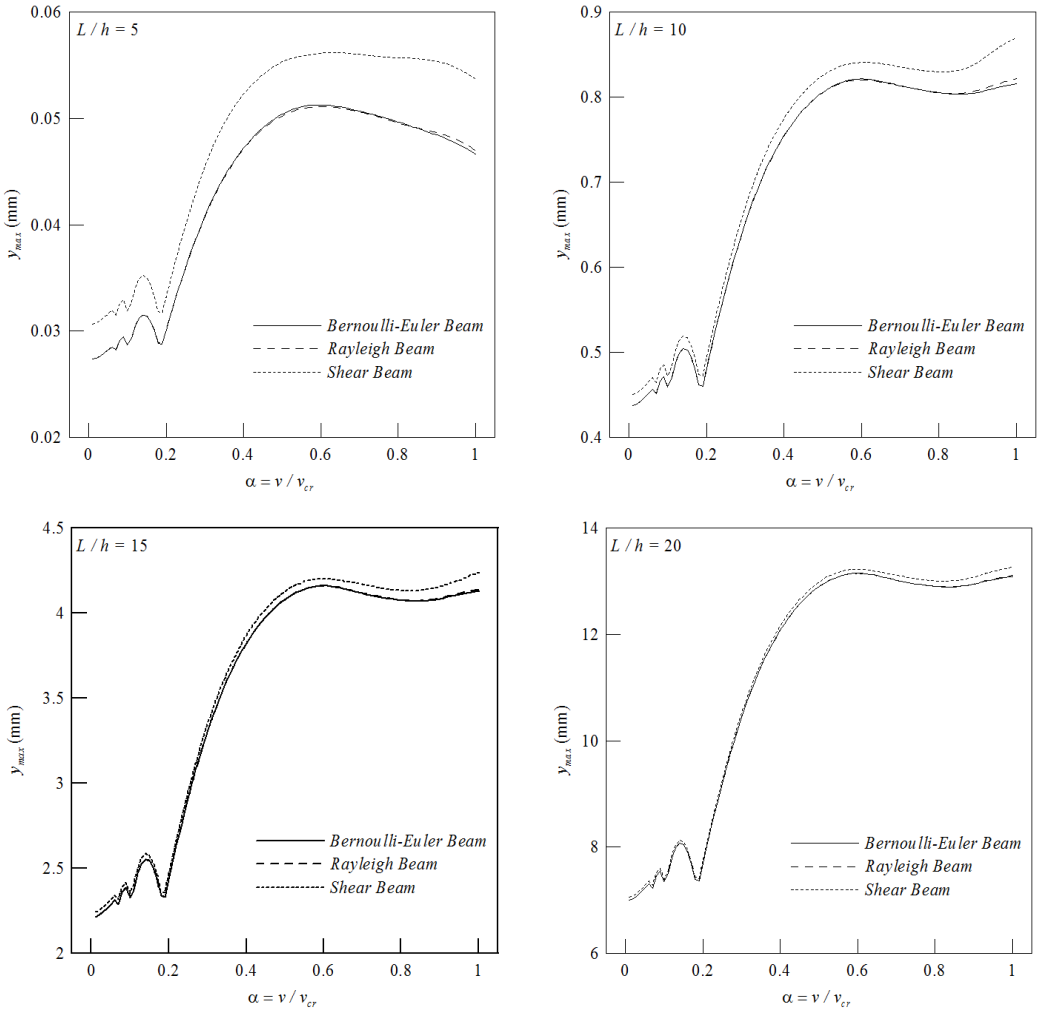

Fig. 5. Maximum deflection of the beam at its midspan vs. dimensionless velocity of the mass for different beam lengths (N/N_{cr}=-0.10, M/mL=0.15).

Variation of maximum deflection and bending moment of the beam at its midspan with the mass parameter M/mL is given in Fig. 7 for Bernoulli-Euler beam, L/h=20 and α=0.20. Both the deflection and the bending moment increase with increasing M/mL. As pre-stressing force increases, deflections and bending moments of the beam increase, too.

Figs. 8 and 9 give variation of maximum deflection and bending moment at midspan of the beam with M/mL for N/N_{cr}=-0.10, α=0.20, and L/h=5 and 10 considering different beam models. According to these figures, consideration of shear deformation in calculations increases both the deflection and the bending moment while rotatory inertia has almost no effect. Shear deformation has greater effect on the deflection response compared to the bending moment response, especially for beams with smaller L/h values.

When the mass moves along the beam length, the deflection and the bending moment at midspan and the contact force between the mass and the beam are given in Fig. 10 for various pre-stressing forces. Here, L/h=20, M/mL=0.15, α=0.20 and Bernoulli-Euler beam model is considered. As stated above, an increase in compressive axial forces (pre-stressing forces) causes greater deflections and bending moments. However, the contact force between the mass and the beam is not considerably affected by increasing pre-stressing forces.

In Fig. 11, a comparison of the deflection and the bending moment at midspan of the beam and the contact force distribution under the moving mass for different beam lengths is given for N/N_{cr}=-0.10, M/mL=0.15, α=0.20 considering different beam models. Results for the deflection and the bending moment in this figure are

in good agreement those of Figs. 5, 6, 8 and 9. As can be seen in these figures, midspan deflections significantly increase by considering shear deformation for short beams. However, shear deformation has little effect on the bending moment and the contact force compared to the deflection response.

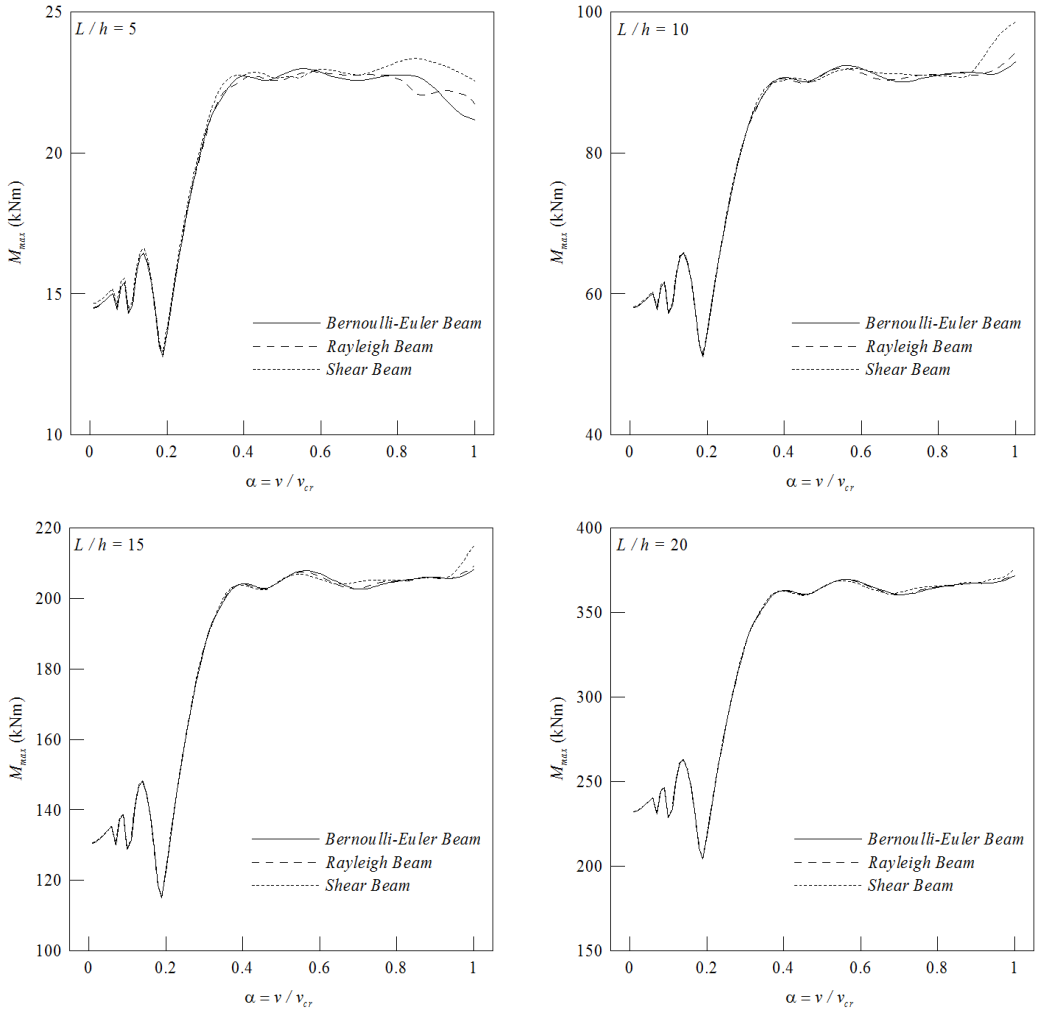

Fig. 6. Maximum bending moment at midspan of the beam vs. dimensionless velocity of the mass for different beam lengths (N/N_{cr}=-0.10, M/mL=0.15)

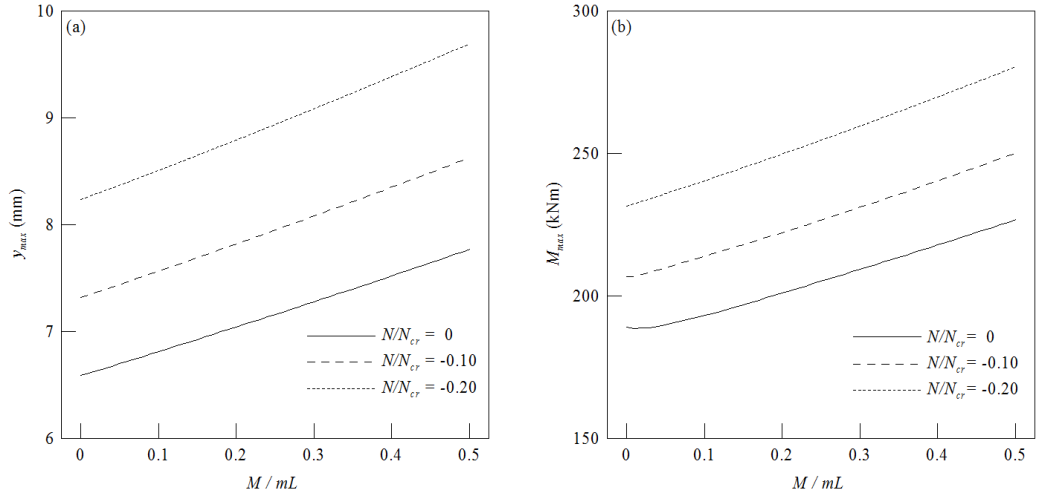

Fig. 7. Maximum dynamic response of the beam at its midspan vs. for various pre-stressing forces; (a) Deflection; (b) Bending moment (L/h=20, α=0.20)

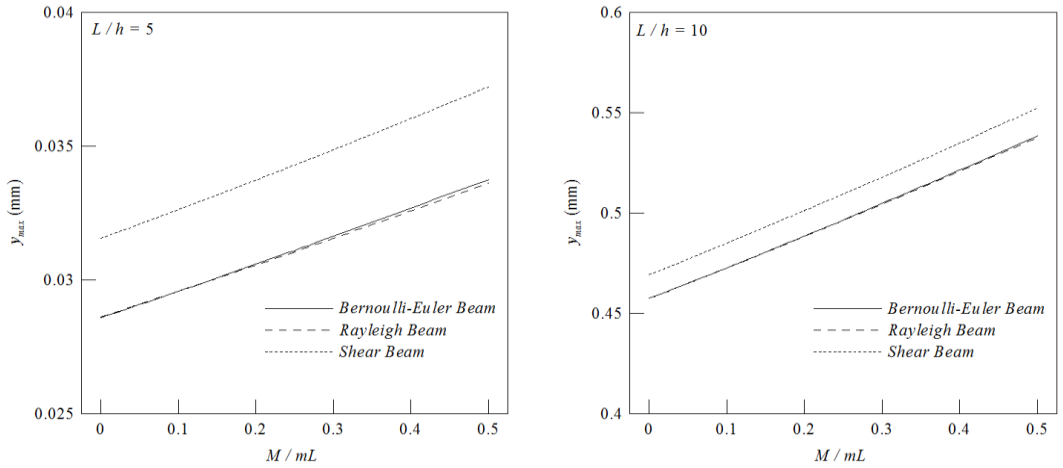

Fig. 8. Maximum deflection of the beam at its midspan vs. M/mL for different beam lengths (N/N_{cr}=-0.10, α=0.20)

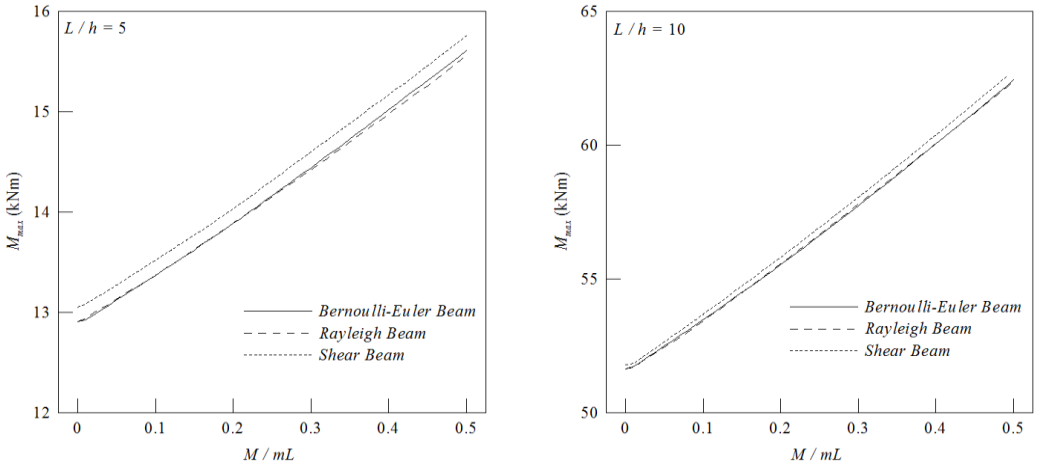

Fig. 9. Maximum bending moment at midspan of the beam vs. M/mL for different beam lengths (N/N_{cr}=-0.10, α=0.20)

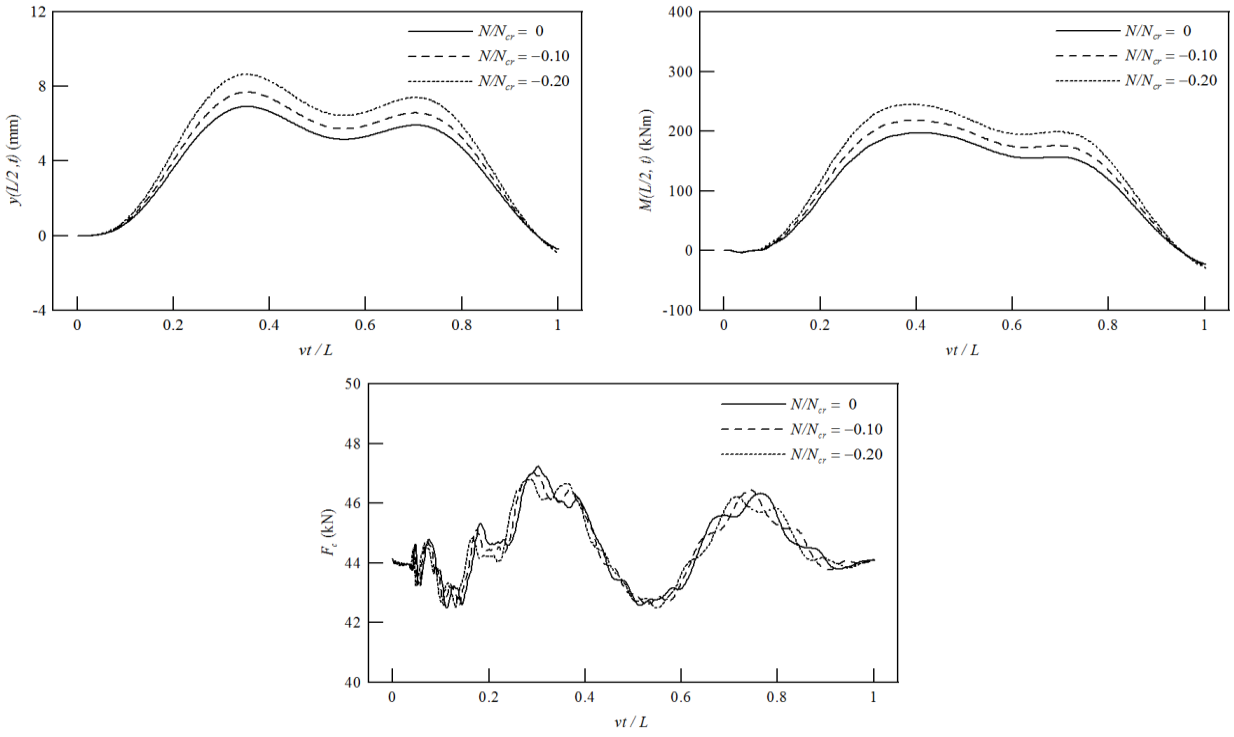

Fig. 10. Deflection, bending moment and contact force distributions under the moving mass for various pre-stressing forces (L/h=20, M/mL=0.15, α=0.20)

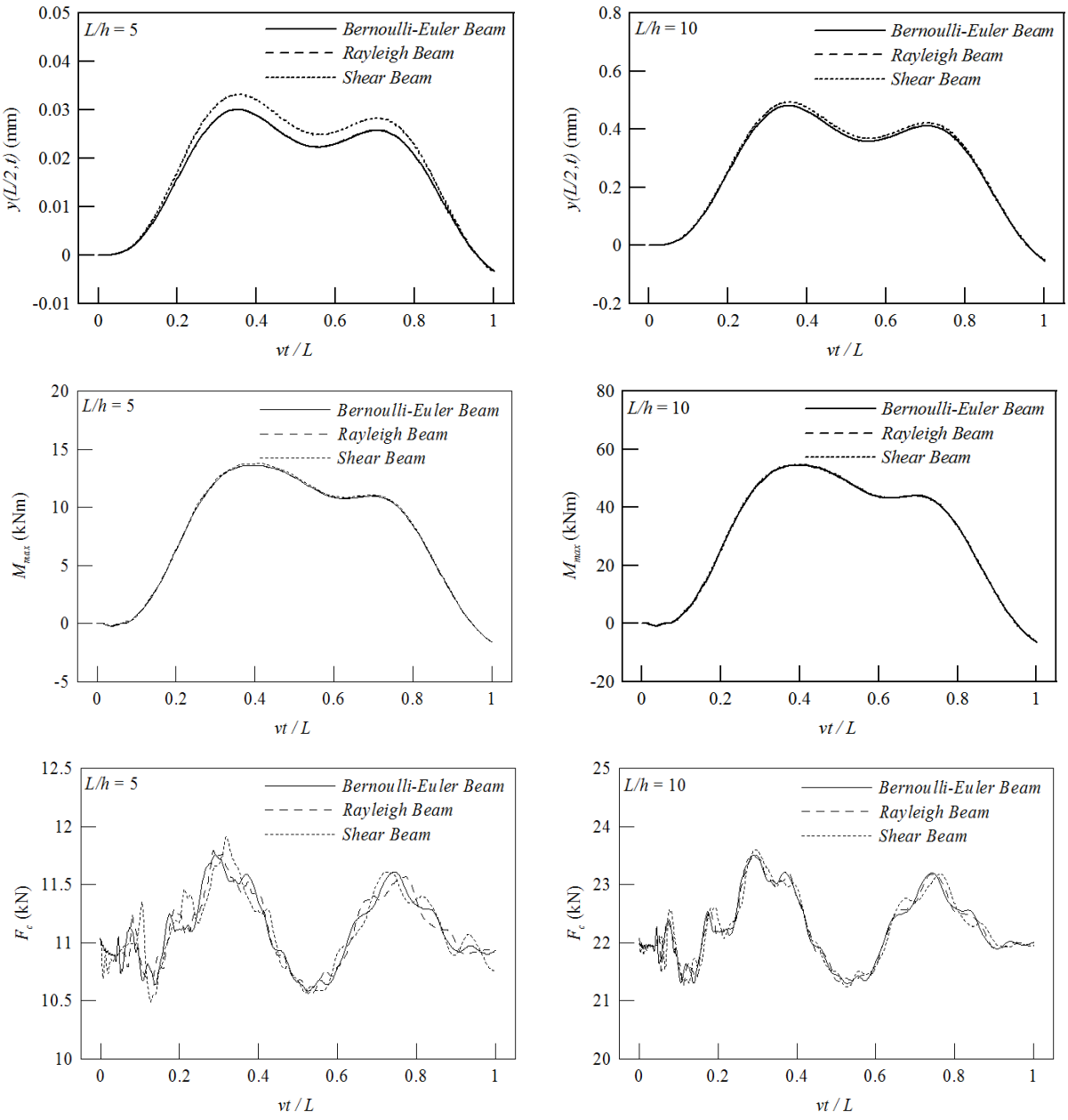

Fig. 11. Deflection, bending moment and contact force distributions under the moving mass for different beam lengths (N/N_{cr}=-0.10, M/mL=0.15, α=0.20)

5. Conclusions

This study presents analytical solution of moving mass problem for pre-stressed elastic beams using different beam models. The assumed mode method is used to derive equations of motion with time-dependent coefficients in matrix form. Numerical solution is, then, performed by using Newmark method to obtain dynamic deflections of the beam. Once deflections are obtained, the bending moment and the contact force between the mass and the beam are easily calculated. Effects of the axial force, rotatory inertia and shear deformation on dynamic behavior of the beam are studied by depending on several parameters such as weight and speed of the moving mass and the beam length.

Results show that axial force is important in calculation of beam deflections and bending moments. Results also show that shear deformation has considerable effect on the response of beams having small slenderness ratio, i.e., short beams, while rotatory inertia has almost no effect. The contact force is not affected significantly by axial force, rotatory inertia and shear deformation of the beam. In addition, results obtained from this study are also in good agreement with those of previous works.

References

Akin JE, Mofid M (1989). Numerical solution for the response of beams with moving mass. *ASCE Journal of Structural Engineering*, 115, 120-131.

Bilello C, Bergman LA (2004). Vibration of damaged beams under a moving mass: theory and experimental validation. *Journal of Sound and Vibration*, 274, 567-582.

Bowe CJ, Mullarkey TP (2008). Unsprung wheel-beam interactions using modal and finite element models. *Advances in Engineering Software*, 39, 911-922.

Chan THT, Yung TH (2000). A theoretical study of force identification using pre-stressed concrete bridges. *Engineering Structures*, 23, 1529-1537.

Esmailzadeh E, Ghorashi M (1995). Vibration analysis of beams traversed by uniform partially distributed moving masses. *Journal of Sound and Vibration*, 184, 9-17.

Esmailzadeh E, Ghorashi M (1997). Vibration analysis of a timoshenko beam subjected to a travelling mass. *Journal of Sound and Vibration*, 199, 615-628

Foda MA, Abduljabbar Z (1998). A dynamic green function formulation for the response of a beam structure to a moving mass. *Journal of Sound and Vibration*, 210, 295-306.

Frýba L (1972). Vibration of Solids and Structures Under Moving Loads. Nordhoff international Publishing, Groningen, The Netherlands.

Jeffcott HH (1929). On the vibration of beams under the action of moving loads. *Philosophical Magazine*, Series 7, 8, 66-67.

Kahya V (2009). Dynamic analysis of pre-stressed elastic beams under moving mass loads. *TUMTMK 16th National Mechanics Conference*, June 22-26, Kayseri, Turkey.

Kiani K, Nikkhoo A, Mehri B (2009). Prediction capabilites of classical and shear deformable beam models cited by a moving mass. *Journal of Sound and Vibration*, 320, 632-648.

Kocatürk T, Şimşek M (2006). Dynamic analysis of eccentrically prestressed viscoelastic timoshenko beams under a moving harmonic load. *Computers and Structures*, 84, 2113-2127.

Kocatürk T, Şimşek M (2006). Vibration of viscoelastic beams subjected to an eccentric compressive force and a concentrated moving harmonic force. *Journal of Sound and Vibration*, 291, 302-322.

Lee HP (1996). Dynamic response of a beam with a moving mass. *Journal of Sound and Vibration*, 191, 289-294.

Lee U (1998). Separation between the flexible structure and the moving mass sliding on it. *Journal of Sound and Vibration*, 209, 867-877.

Lou P, Dai GL, Zeng QY (2006). Finite-element analysis for a Timoshenko beam subjected to a moving mass. Proceedings of Institution of Mechanical Engineers-Part C: *Journal of Mechanical Engineering Science*, 220, 669-677.

Mackertich S (1992). Response of a beam to a moving mass. *Journal of Acoustical Society of America*, 92, 1766-1769.

Michaltsos G, Sophianopoulos D, Kounadis AN (1996). The effect of a moving mass and other parameters on the dynamic response of a simply supported beam. *Journal of Sound and Vibration*, 191, 357-362.

Mofid M, Akin JE (1996). Discrete element response of beams with travelling mass. *Advances in Engineering Software*, 25, 321-331.

Mofid M, Shadnam M (2000). On the response of beams with internal hinges, under moving mass. *Advances in Engineering Software*, 31, 323-328.

Sadiku S, Leipholz HHE (1987). On the dynamics of elastic systems with moving concentrated masses. *Ingenieur-Archiv*, 57, 223-242.

Stanišić MM (1985). On a new theory of the dynamic behavior of the structures carrying moving masses. *Ingenieur-Archiv*, 55, 176-185.

Şimşek M, Kocatürk T (2007). Dynamic analysis of eccentrically prestressed damped beam under moving harmonic force using higher order shear deformation theory. *ASCE Journal of Structural Engineering*, 133, 1733-1741.

Şimşek M, Kocatürk T (2009). Nonlinear dynamic analysis of an eccentrically pre-stressed damped beam under a concentrated moving harmonic load. *Journal of Sound and Vibration*, 320, 235-253.

Ting EC, Genin J, Ginsberg JH (1974). A general algorithm for moving mass problem. J*ournal of Sound and Vibration*, 33, 49-58.

Wu JJ, Whittaker AR, Cartmell MP (2001). Dynamic responses of structures to moving bodies combined finite element and analytical methods. *International Journal of Mechanical Sciences*, 43, 2555-2579.

Yavari A, Nouri M, Mofid M (2002). Discrete element analysis of dynamic response of Timoshenko beams under moving mass. *Advances in Engineering Software*, 33, 143-153.

Challenge Journal of Structural Mechanics

Vertical ground motion influence on seismically isolated & unisolated bridges

Naim Eser Reyhanoğulları *, Uğurhan Akyüz

Department of Civil Engineering, Middle East Technical University, 06531 Ankara, Turkey

ABSTRACT

In this study, influences of vertical ground motion on seismically isolated bridges were investigated for seven different earthquake data. One assessment of bearing effect involves the calculation of vertical earthquake load on the seismically isolated bridges. This paper investigates the influence of vertical earthquake excitation on the response of briefly steel girder composite bridges (SCB) with and without seismic isolation through specifically selected earthquakes. In detail, the bridge is composed of 30m long three spans, concrete double piers at each axis supported by mat foundations with pile systems. At both end of the spans there exists concrete abutments to support superstructure of the bridge. SCBs which were seismically isolated with ten commonly preferred different lead-rubber bearings (LRB) under each steel girder were analyzed. Then, the comparisons were made with a SCB without seismic isolation. Initially, a preliminary design was made and reasonable sections for the bridge have been obtained. As a result of this, the steel girder bridge sections were checked with AASHTO provisions and analytical model was updated accordingly. Earthquake records were thought as the main loading sources. Hence both cases were exposed to tri-axial earthquake loads in order to understand the effects under such circumstances. Seven near fault earthquake data were selected by considering possession of directivity. Several runs using the chosen earthquakes were performed in order to be able to derive satisfactory comparisons between different types of isolators. Analytical calculations were conducted using well known structural analysis software (SAS) SAP2000. Nonlinear time history analysis was performed using the analytical model of the bridge with and without seismic isolation. Response data collected from SAS was used to determine the vertical load on the piers and middle span midspan moment on the steel girders due to the vertical and horizontal component of excitation. Comparisons dealing with the effects of horizontal only and horizontal plus vertical earthquake loads were introduced.

ARTICLE INFO

Article history:
Received 16 May 2015
Accepted 11 July 2015

Keywords:
Seismic isolation
Bridges
Vertical ground motion
Nonlinear time history
Lead rubber bearing

1. Introduction

A structure should remain elastic during seismic excitation to avoid damage and should also retain the ability to undergo large deformations to facilitate energy dissipation. These demands seem paradoxical with the application of regular structural elements. Therefore, special structural elements should be considered to accomplish these crucial two extremes. The seismic isolation systems can be accounted for the special structural elements which provide structural elements stress levels in elastic range and energy dissipation by large deformation capability.

Vertical earthquake effect on bridges is a serious issue since it has considerable contribution to design stresses of structural members. This is why several studies regarding the vertical earthquake loads on bridges have been performed so far. Most of the studies focused on vertical ground motion influence on bridges without seismic base isolation.

* *Corresponding author*. E-mail address: reyhanogullari@yahoo.com (N. E. Reyhanoğulları)
ISSN: 2149-8024 / DOI: http://dx.doi.org/10.20528/cjsmec.2015.07.022

McRae and Tagawa (2002) undertook a dynamic inelastic time-history analyses of single-degree-of-freedom (SDOF) bilinear oscillators in order to determine the ability of the Coefficient Method (FEMA273/FEMA356) and the Capacity Spectrum Method (ATC-40) to predict the total displacement demands of simple structures. Both the Coefficient Method (CM) and the Capacity Spectrum Method (CSM) were calibrated to obtain the exact inelastic response displacements for near-fault (NF) and far-fault (FF) shaking. As a result of dynamic inelastic analyses of single degree of freedom bilinear oscillators McRae and Tagawa (2002) indicates that, oscillators with demands estimated by the CM, and with fundamental periods less than about 0.8 s, were not affected significantly by near-fault shaking effects. For longer fundamental period oscillators, oscillator strengths may need to be increased by more than 60% to account for inelastic shaking effects from NF sites in the region of positive directivity compared to that for shaking from Far Fault (FF) or NF near-epicenter sites for the same target displacement ductility. NF shaking did not cause significant trends in the displacement demands of oscillators evaluated by the CSM method.

A study by Kunnath et al. (2008) indicates that, studies in the past have clearly identified several potential issues that deserve additional attention. The study is undertaken with the objective of assessing the current provisions in The Caltrans Seismic Design Criteria (SDC) 2006 for incorporating vertical effects of ground motions in seismic evaluation and design of ordinary highway bridges. In the code, it is required to take into account the vertical ground motion for ordinary highway bridges where the site peak rock acceleration is 0.6 g or greater. In order to consider the vertical ground motion an equivalent static vertical load required to be applied to the superstructure to estimate the effects of vertical acceleration. The loading procedure aims to perform a separate analysis to check nominal capacity of superstructure against loading stated in SDC 006. As a result of the study, two major conclusions were found. First, vertical ground motions have significant effects on the axial force demand in columns. Second, vertical ground motions have significant effects on moment demands at the middle of the span. Particularly, for the case of the shear demand and shear capacity fluctuations. It should also be noted that axial forces vary at much higher frequencies than lateral forces. Hence, the sudden shifts in shear capacity as the column goes from compression to tension may require further investigation. On the other hand, the study concludes the amplification of negative moments in the midspan section as the primary issue that needs to be involved in the SDC-2006. In particular, the current requirement that vertical ground motions be considered only for sites where the expected peak rock acceleration is at least 0.6 g is considered not to be an adequate basis to assess the significance of vertical effects. According to Kunnath et al. (2008) a more detailed SDC criteria shall be created about the design specification for the consideration of vertical effects by means of a static load equivalent to 25% of the dead load applied in the upward direction.

Warn et al. (2008) studied vertical earthquake loads on seismic isolation systems in bridges. The study summarizes and presents sample results from earthquake simulation testing performed on a bridge model isolated with low damping rubber bearing and lead rubber bearings. Results from the testing program were used to investigate the influence of vertical excitation on the vertical load carried by the isolation system and the axial load of individual bearings. As a result of simulations, significant amplifications in the vertical response for both the low damping rubber bearing and lead rubber bearing bridge configurations were experimentally observed. However from a comparison of amplification factors for both the isolated and fixed-base configurations estimated using spectral analysis suggests the isolation system itself results in only a marginal increase in amplification over the fixed-base bridge for the model and systems considered in the study. Hence, those results suggest that the vertical flexibility of the bridge-isolation system should not be ignored for design. Use of the peak ground acceleration of the vertical component would underestimate the vertical earthquake load on the isolation system. They concluded that, the spectral analysis procedure considering the full vertical stiffness of the isolator lead to more reasonable and accurate estimates of the vertical earthquake load on the isolation system for the bridge model and isolation systems.

In this study, bridges with seismic isolation and without seismic isolation are considered. They can be classified as lightweight structures. If seismic isolation is applied, weight of the structure gains importance against vertical component of ground motions. Therefore it is considered seismically isolated bridges are needed to be investigated deeply. From this point of view, the study intends to investigate the influence of vertical earthquake excitation on the response of a briefly two types of bridges through seven earthquakes. First type of bridge is seismically isolated steel composite bridge. Second type is a regular steel composite bridge. Lead rubber bearings are used for seismic isolation. The intention of studying same bridge with seismic isolation and without seismic isolation is to be able to reach a comparison regarding influence of vertical component of earthquakes. Additionally, in order to reach more realistic and satisfactory comparisons between isolators on same bridge, a set composed of nine isolators which have different characteristic properties is used. To sum up considering many parameters stated herein several time history analyses are conducted using the structural analysis software SAP2000. As a result response data collected from the analyses is used to determine the vertical load on the piers and isolators and middle span moment on the steel girders due to the earthquake excitations. A comparison between all configurations is introduced and discussed.

2. Bridge Model and Isolators

In this study, a steel girder composite bridge is considered because it is in the group of beam type bridges. As a result, influences on bending of beam can be observed.

Also, composite steel girder bridge may be classified as relatively more lightweight than other type bridges.

The made up bridge which was investigated in an earlier study done by Eröz and DesRoches (2007), has been chosen. This is a regular steel girder bridge with RC piers and piles. The fundamental structural elements are derived from the previous study and developed through this study. After developing the bridge an initial design is performed in order to see whether the bridge is complying with the AASHTO provisions or not. For this reason, main girder and RC piers are checked against major loads applied to the bridge. For the sake of safety of initial design, AASHTO Strength I load combination limit state is used. Strength I load combination involves dead load and live load with load factors 1.25 and 1.75, respectively. After adequate number of iterations on sections, the structural elements of the bridge are finalized.

The number of span is 3 and the span length is 30.3 m. Fig. 1 and Fig. 2 show elevations of the bridge in the long and in the short axis, respectively. From top to bottom structural members and sectional properties are as follows; RC deck is 0.25 m thick. One of the most important members of the bridge is certainly steel girders. The steel girders are selected from I shaped sections with the geometric properties shown on Fig. 3. Diaphragm beam is composed of a rectangular section with a width and a height of 1.2 m. Circular RC pier has a diameter of 0.9 m and a height of 4.6 m. RC Mat foundation has plan dimensions of 3.6 m to 3.6 m with a thickness of 1.1 m. Finally, circular RC pile has a diameter of 0.45 m and a height of 4.5 m. Moreover, soil underneath the foundation is considered to be a common soil type of clayey medium dense sand with a subgrade reaction modulus of 35GPa/m.

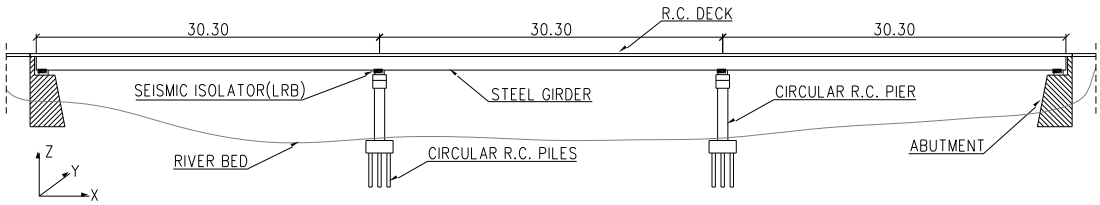

Fig. 1. Bridge elevation in long axis.

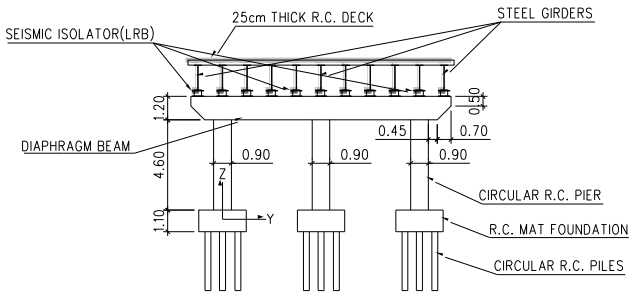

Fig. 2. Bridge elevation in short axis.

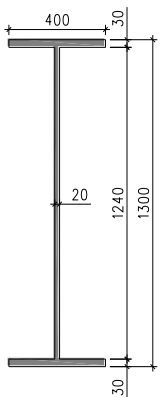

Fig. 3. I shaped steel girder's geometric properties.

In this study, isolators are modeled as nonlinear link elements. Hence, effective stiffness, damping, yield strength and post yield stiffness ratio are defined. By definition, yield strength is the force at yield of isolator. Post yield stiffness ratio stands for ratio of plastic stiffness to elastic stiffness. This ratio is usually taken as 0.1 for design purposes. The basic characteristic properties are chosen from a manufacturers catalog cut-sheet. Furthermore, other mentioned properties for nonlinear analyses are calculated to be used on the analyses program. 9 different commercially available isolators are investigated in the study. All isolators are chosen from LRB in order to investigate the response with damping. The overall diameters, rubber thicknesses and layers, lead core diameters and all mounting plate properties differ from one isolator to other. Hence, a wide range of isolators are used in the study. Table 1 shows the characteristic properties and calculated additional properties of the isolators which are used for modeling. On the table bold letters and numbers show the calculated properties and the rest of parameters are taken from the manufacturer's cut-sheet. Additionally, the labels of the commercially available isolators are show as ISO-XX where XX is suffix starting from 01 to 09. Therefore the difference that comes out in results may be distinguished easily.

3. Ground Motion Sets

Earthquakes (EQ) are generally grouped in accordance with three properties; peak ground accelerations (PGA) and peak ground velocities (PGV), soil classifications and possession of directivity. In this study, soil classifications and possession of directivity are considered as constant parameters and PGA and PGV vary to investigate response of the bridge under different conditions.

Soil classification is described as an important parameter for an EQ since soil properties directly have influences on propagation waves generated by ground motions. Hence, it is decided to choose EQs whose site classes are same, for a reasonable comparison different EQs.

In the study, the soil classification criteria of USGS is preferred since the EQs record source Peer Strong Motion Database directly gives soil classification as per USGS and it is chosen as EQs record source. Moreover, a soil class of "C" as per USGS classification is selected for all chosen EQs and stations.

Table 1. Characteristic properties of the selected isolators.

Isolator ID	Isolator Diameter D_I (mm)	Lead Diameter D_L (mm)	Post Yield Stiffness K_d (kN/mm)	Elastic Stiffness K_e (kN/mm)	Compression Stiffness K_v (kN/mm)	Effective Stiffness K_{eff} (kN/mm)	Characteristic Strength Q_d (kN)	Yield Strength F_y (kN)	Maximum Displacement u_{max} (mm)
ISO-01	355	0-100	0.20	2.00	100.00	0.85	65.00	72.22	150
ISO-02	455	0-125	0.30	3.00	100.00	0.96	110.00	122.22	250
ISO-03	570	0-180	0.50	5.00	500.00	1.25	180.00	200.00	360
ISO-04	800	0-230	0.70	7.00	1000.00	1.48	265.00	294.44	510
ISO-05	900	0-255	0.70	7.00	1400.00	1.65	355.00	394.44	560
ISO-06	1050	0-305	0.90	9.00	2100.00	2.13	580.00	644.44	710
ISO-07	1260	0-355	1.20	12.00	3700.00	2.60	755.00	838.89	810
ISO-08	1360	0-380	1.40	14.00	5100.00	2.95	890.00	988.89	860
ISO-09	1550	0-405	1.80	18.00	6500.00	3.49	1025.00	1138.89	910

EQs are classified as being near fault ground motions involving directivity. A dependable source is used to see the EQs classified as near fault ground motions involving directivity. The source is a previous study done by MacRae and Tagawa (2002) which investigates methods to estimate some specific structures using far-fault and near-fault directivity record sets. The near fault directivity record sets in MacRae and Tagawa (2002) are considered to be a dependable list of near fault ground motions involving directivity.

PGAs and PGVs are very important for grouping EQs. Three components (two horizontal and one vertical) of the EQs are used in the study. The selected EQs' lateral components and vertical components are in the range of 0.268 g to 0.897 g, and 0.242 g to 0.586 g, respectively, regarding PGA. On the other hand, their horizontal components and vertical components are in the range of 46,9 cm/s to 109,3 cm/s and 18,4 cm/s to 38,5 cm/s, respectively, regarding PGV. Seven EQs are considered in this study in order to provide adequate range of ground acceleration and ground velocity. They are sorted by the ratio of SRSS of horizontal peak accelerations to vertical peak acceleration. As a result, a normalized EQs property ratio is formed to be used while constituting comparisons of results. Table 2 presents the properties of the selected ground motions within the specified selection criterions.

4. Analysis Procedure

Three types of analysis cases are defined in the program. These are linear static, linear modal and nonlinear modal history (FNA) cases. Linear static type is used to define dead load and live load cases. Linear modal type is used to define Ritz-vector mode shape analysis case. Finally, the FNA type is used to define EQ load cases. Since FNA is a faster sort of time history analysis (THA), in order to be able to perform several runs this method is used. All cases started with a zero condition to discard effect of each analysis case to each other. For Ritz-vector case a tri-axial acceleration load is defined, since it is strictly required to define particular loads for this type of analysis. In addition to load definition, maximum number of modes is set as 17 to make sure 90% mass participation in each orthogonal direction. Two different FNA cases are created for each EQ. One of them is created to observe the influence of only horizontal components of EQs and named with suffix "…+H". Additionally, other one is created to observe the influence of both horizontal and vertical components of EQs and named with suffix "…+HV".

Modal damping is chosen as 5% constant damping for all of the FNA cases. Also, number of output time steps and output step sizes are chosen considering the EQ data time step and length. A total history time of 15 seconds is specified for each EQ.

In the analysis, combinations are defined in accordance with strength criteria stated in AASHTO Section 3. Each analysis case involves only effects due to its defined load or EQ. This is why combinations are defined. They are aimed to be used for combining effects due to different case. The combinations are grouped into two: Strength-I and Extreme Event-I. Strength-I has one sub-item including dead load (DL) and live load (LL). On the other hand, Extreme Event-I has 15 sub-items. 14 of them are generated from DL, LL and EQs and one is from DL and LL. Extreme Event-I is abbreviated to read Comb1 to Comb7. Also, type of combination for all of them is selected as linear add.

Table 2. Selected ground motion sets.

Earthquake	Location	Station	USGS Soil Class	Direction	A_p (g)	V_p (cm/s)	A_p / V_p (1/s)	$A_{p,HOR}$ (g)	$A_{p,HOR,max}$ / $A_{p,VERT}$	$A_{p,HOR}$ / $A_{p,VERT}$
Imperial (15/10/79)	California/ USA	El Centro Array #7	C	140 (UX)	0.338	47.617	6.963	0.57	0.851	1.054
				230 (UY)	0.463	109.261	4.157			
				Up (UZ)	0.544	26.310	20.284			
Imperial (15/10/79)	California/ USA	El Centro Array #5	C	140 (UX)	0.519	46.857	10.866	0.64	0.966	1.197
				230 (UY)	0.379	90.549	4.106			
				Up (UZ)	0.537	38.522	13.675			
Northridge (17/01/94)	California/ USA	Newhall	C	90 (UX)	0.583	74.878	7.638	0.83	1.077	1.514
				360 (UY)	0.590	96.879	5.974			
				Up (UZ)	0.548	31.532	17.049			
Düzce (12/11/99)	Turkey	Düzce	C	180 (UX)	0.348	59.990	5.691	0.64	1.499	1.788
				270 (UY)	0.535	83.506	6.285			
				Up (UZ)	0.357	22.605	15.493			
Kocaeli (17/08/99)	Turkey	Yarımca	C	60 (UX)	0.268	65.740	3.999	0.44	1.442	1.818
				330 (UY)	0.349	62.177	5.506			
				Up (UZ)	0.242	30.814	7.704			
Northridge (17/01/94)	California/ USA	Sylmar	C	52 (UX)	0.612	117.432	5.113	1.09	1.531	1.853
				142 (UY)	0.897	102.208	8.609			
				Up (UZ)	0.586	34.587	16.621			
Erzincan (13/03/92)	Turkey	Erzincan	C	EW (UX)	0.496	64.282	7.569	0.72	2.077	2.883
				NS (UY)	0.515	83.959	6.017			
				Up (UZ)	0.248	18.373	13.242			

5. Comparison of Results

5.1. Modal analysis

Initially, modal analysis outputs are given such as fundamental periods of each orthogonal direction for all mathematical models. Table 3 presents the fundamental periods of the models with predefined isolator and connection property. All modal outputs are calculated using Ritz-Vector analysis.

Table 3. Fundamental periods of the bridge models.

	Fundamental Period (s)		
Model	UX	UY	UZ
SCB1	1.046	0.937	0.285
SCB2	1.000	0.889	0.284
SCB3	0.911	0.794	0.276
SCB4	0.860	0.740	0.275
SCB5	0.829	0.708	0.275
SCB6	0.762	0.642	0.275
SCB7	0.715	0.597	0.274
SCB8	0.687	0.572	0.274
SCB9	0.651	0.541	0.274
SCB-Fix	0.080	0.210	0.253

5.2. Steel girder midspan moment

Nine steel girder bridge models are generated using nine different commercially available lead rubber bearings. Outputs from these models are normalized with each other to provide a complete investigation about influences of LRBs on girder midspan moment.

Fig. 4 illustrates the H/HV ratios of girder midspan moments with respect to K_{eff}/K_v for seven different EQ data and average of them. Fig. 5 shows that girder midspan moment of the bridge systems does not change with K_{eff}/K_v ratios for the same EQ data. If one use the average result of the seven EQ data for design purposes, the value of H/HV will be 0.72. This means including vertical ground motion in the analysis increases girder midspan moment by 40%.

Fig. 5 illustrates the H/HV ratios of girder midspan moments with respect to $A_{p,HOR}/A_{p,VERT}$ for nine different rubber isolators. It is obvious in this figure that all isolators H/HV curves' fitting on each other which reveals isolator property doesn't have a significant effect on the girder midspan moments in steel girder bridges.

5.3. Bridge systems with and without seismic isolation

The model of the composite steel girder bridge with seismic isolation is reconstructed as a steel girder bridge without seismic isolation. Basically, the reconstruction includes replacement of the isolators at the connections

of diaphragm beams and steel girders with rigid links. On the issue of replacement, main objective is enabling axial force transfer from girders to piers or vice versa.

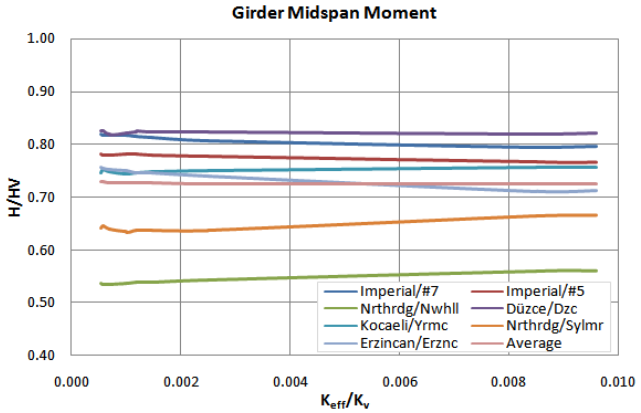

Fig. 4. Girder midspan moment ratios of the bridges with respect to K_{eff}/K_v.

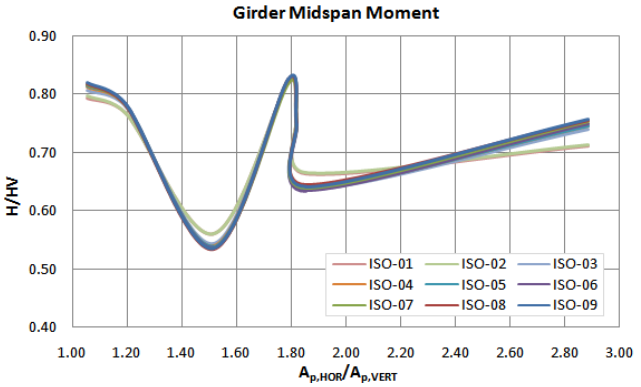

Fig. 5. Girder midspan moment ratios of the bridges with respect to $A_{p,HOR}/A_{p,VERT}$.

Fig. 6 and Fig. 7 present the H/HV ratios of girder midspan moments and pier axial loads with respect to $A_{p,HOR}/A_{p,VERT}$, respectively. On both figures, H/HV ratios of the bridge with seismic isolation show the mean member force ratios from the bridge models with nine different isolators. On the other hand H/HV ratios of the bridge without seismic isolation show output from only one bridge.

Fig. 6 shows that the H/HV ratios of the bridge with seismic isolation are slightly higher than the H/HV ratios of the bridge without seismic isolation. Since, the results calculated by horizontal EQ components (H) in the bridge with seismic isolation is close to the same sort of results in the bridge with seismic isolation, the difference between the H/HV ratios depends on the change of HV value (results calculated with the inclusion of vertical EQ components). Therefore, use of isolation system on a bridge causes significant increase in girder midspan moment in most of the load cases. The rate of increase is approximately 0.9%.

Fig. 7 shows that H/HV ratios of the bridge with seismic isolation are smaller than the H/HV ratios of the bridge without seismic isolation. The discussion in the paragraph above regarding the effects of horizontal and vertical EQ components on H and HV is also acceptable for the pier axial force. Hence, use of isolation system on a bridge causes significant decrease in pier axial force in most of the load cases, although the girder midspan moment increases. The decrease in the pier axial force can be as high as 11%.

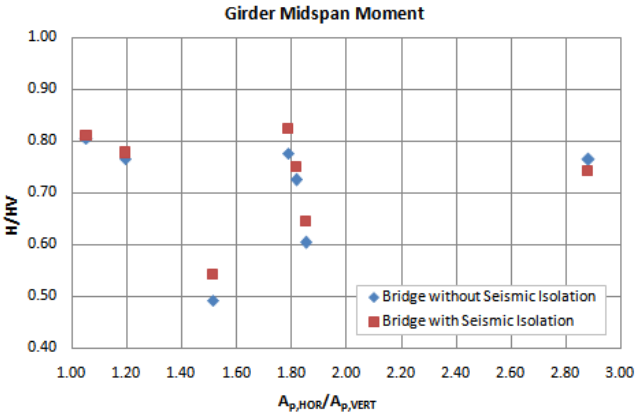

Fig. 6. Girder midspan moment ratios of the bridges with and without seismic isolation.

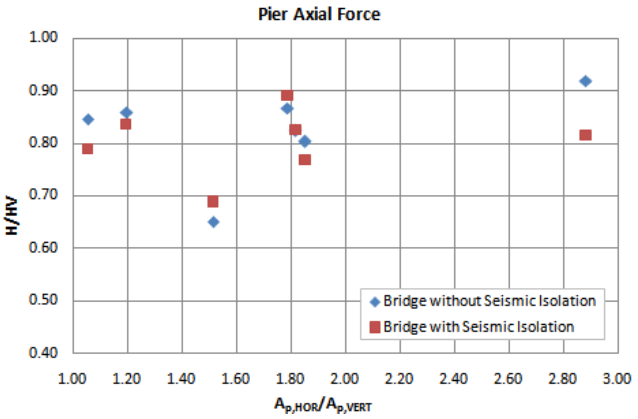

Fig. 7. Pier axial force ratios of the bridges with and without seismic isolation.

6. Conclusions

The main objective of this study was to investigate the influences of vertical ground motion on the bridges with and without seismic isolation. After a brief introduction on seismic isolation and devices, more specific information on seismic isolation on bridges was presented. Besides this, all required information on performing this numerical study was introduced one by one. The study was carried out using a steel girder composite bridge and nine LRBs with different characteristic properties. Nine mathematical bridge models with and without seismic isolation were built. Moreover, seven different EQ data in same site class were selected. Two horizontal and one vertical components of the EQs were used in the analysis of bridges using FNA in the SAP2000 software. Finally, numerical results were obtained and introduced. The member forces presented for comparison are girder midspan moment, pier axial force and isolator axial force.

This study reveals that;

- The bridges with seismic isolation are not as vulnerable as the bridges without seismic isolation according to the fundamental periods on the response spectrums regarding the vertical component of the EQs.
- The vertical components of the EQs are not producing resonance in seismically isolated bridges for the ground motion data chosen in this study.
- Vertical ground motion affects the girder midspan moment significantly.
- Disregarding the vertical ground motion from the analysis leads to mean underestimation of 27% of girder midspan moment.
- The bridge systems with different isolators have the same H/HV ratio of the girder midspan moment for same combination. Also, varying K_{eff}/K_v ratio doesn't have a significant effect on the girder midspan moments. Hence, isolator property doesn't have a significant effect in steel girder bridge analyzed in this study.
- Use of isolation system on a bridge causes significant increase in girder midspan moment in most of the load cases. The rate of increase fluctuates with the $A_{p,HOR}/A_{p,VERT}$ ratio in a range of 0.8% to 9.5%.

REFERENCES

AASHTO LRFD (2007). Bridge Design Specifications. American Association of State Highway and Transportation Official, Washington, DC.

Applied Technology Council (1996). Seismic evaluation and retrofit of concrete buildings, volume 1 (ATC 40), report No. SSC 96-01.

Bowles JE (1988). Foundation Analysis and Design. McGraw-Hill, New York.

California Department of Transportation Technical Publications, Graphics and Outreach Services Branch (2006) Seismic Design Criteria.

Eröz M, DesRoches R (2007). Bridge seismic response as a function of the friction pendulum system (FPS) modeling assumptions. *Engineering Structures*, 30(11), 3024-3212.

FEMA 273 (1997). Prestandard and Commentary for the Seismic Rehabilitation of Buildings. American Society of Civil Engineers, Federal Emergency Management Agency, Washington, DC.

FEMA 356 (2001). Prestandard and Commentary for the Seismic Rehabilitation of Buildings. American Society of Civil Engineers, Federal Emergency Management Agency, Washington, DC.

Kunnath SK, Erduran E, Chai YH, Yashinsky M (2008). Effect of near-fault vertical ground motions on seismic response of highway overcrossings. *Journal of Bridge Engineering*, 13(3), 282–290.

McRae GA, Tagawa H (2002) Methods to estimate displacements of PG&E structures. A final report on research conducted under PG&E/PEER research program, PG&E/PEER Task No: 505.

Pacific Earthquake Engineering Research Center (PEER) (2000). The regents of the University of California, PEER strong ground motion database, http://peer.berkeley.edu/smcat/search.html.

Warn GP, Whittaker AS (2008). Vertical earthquake loads on seismic isolation systems in Bridges. *ASCE Journal of Structural Engineering*, 134 (11), 1696-1704.

Challenge Journal of Structural Mechanics

Envelope analysis equations for two-span continuous girder bridges

Daud Abdoh *

Department of Civil Engineering, University of Jordan, 11942 Amman, Jordan

ABSTRACT

In this paper, envelope analysis equations for two-span continuous girder bridges were presented by deriving the analysis equation for uniformly distributed loading, concentrated loading and moving loads (single and multiple wheel loads). Most bridge engineers are using special software's to find the moment, shear and deflection envelopes for bridge girder, the complexity for this analysis increasing with the number of spans, most of cases are one-span and two-span continuous bridge, the two-span continuous bridge is more complicated which was presented in this paper, the same methodology can be applied in one-span bridge. The objective of this paper was to give all the bridge engineers direct equations for complete analysis (moment, shear and deflection) for two-span continuous bridge with more accuracy than most bridge software's by adapting continuous moving of wheel loads rather than using interval check distance to move the concentrated loads as in most of bridge software's. Pinned end boundary condition was presented here. The results were showed that shear envelope, moment envelope and maximum envelope deflection values were obtained by direct equations for two-span continuous girder bridges under single and multiple moving loads.

ARTICLE INFO

Article history:
Received 23 May 2015
Accepted 14 July 2015

Keywords:
Computational analysis
Envelope analysis
Continuous girder bridge
Two-span girder bridge
Moving load

1. Introduction

Earthquake analysis of the bridge design that won an international design competition, in which aesthetics played an important role. (Wieland and Malla, 2015). In order to reflect this phenomena analysis envelope equations (moment, shear and deflection) for two-span continuous girder bridge was derived on four stages, based on direct integration method that depends on solving linear equations to obtain the values of unknown integration constants coming from each integration process.

The chain of integration processes starting from loading to shear to moment to slope and finally to deflection, will produce one integration constant on each integration step, these unknown constants defines the analysis equations (moment, shear and deflection), the formulation of solving equations based on geometry of bridge girder, loading and boundary conditions.

The first stage was to derive the analysis equations for uniformly distributed loading, these loads mainly represent the own weight of bridge girder, super imposed dead loads and lane live loads.

The first stage was to derive the analysis equations for uniformly distributed loading, these loads mainly represent the own weight of bridge girder, super imposed dead loads and lane live loads.

The second stage was to derive the analysis equations for single concentrated load located in any specified location for any value on each span.

The third stage was to derive the envelope analysis equations for a single moving load based on the concentrated load analysis equations (second stage).

The fourth stage was to derive the envelope analysis equations for multiple moving load based on envelope analysis equations for single moving load (third stage), the motion of moving load will be continuous in third and fourth stages giving more accurate results.

2. Sign Convention

Load downward was assumed to be positive, load upward was negative, positive shear was upward, negative shear was downward, positive moment was concave

* *Corresponding author*. Tel.: +966-59-9409355 ; Fax: +962-79-6988920 ; E-mail address: daud_abdo@yahoo.com (D. Abdoh)
ISSN: 2149-8024 / DOI: http://dx.doi.org/10.20528/cjsmec.2015.07.025

down (tension at top), negative moment was concave up (compression at top), positive slope for counterclockwise rotation, negative slope for clockwise rotation, negative deflection was downward, positive deflection was upward.

3. First Stage (Uniformly Distributed Load)

The integration of uniformly load for each span gives a linear equation of shear, the integration of shear gives the second order polynomial equation for moment, the integration of moment gives slope equation as third order polynomial, and finally the integration of this slope results in deflection equation as 4th polynomial order equation, as follows:

$$V_1(X) = W_1 \times X + C_1\,, \tag{1}$$

$$M_1(X) = \frac{W_1 \times X^2}{2} + C_1 \times X + C_2\,, \tag{2}$$

$$\theta_1(X) = \frac{W_1 \times X^3}{6 \times EI} + \frac{C_1 \times X^2}{2 \times EI} + \frac{C_2 \times X}{EI} + \frac{C_3}{EI}\,, \tag{3}$$

$$\Delta_1(X) = \frac{W_1 \times X^4}{24 \times EI} + \frac{C_1 \times X^3}{6 \times EI} + \frac{C_2 \times X^2}{2 \times EI} + \frac{C_3 \times X}{EI} + \frac{C_4}{EI}\,, \tag{4}$$

$$V_2(X) = W_2 \times X + C_5\,, \tag{5}$$

$$M_2(X) = \frac{W_2 \times X^2}{2} + C_5 \times X + C_6\,, \tag{6}$$

$$\theta_2(X) = \frac{W_2 \times X^3}{6 \times EI} + \frac{C_5 \times X^2}{2 \times EI} + \frac{C_6 \times X}{EI} + \frac{C_7}{EI}\,, \tag{7}$$

$$\Delta_2(X) = \frac{W_2 \times X^4}{24 \times EI} + \frac{C_5 \times X^3}{6 \times EI} + \frac{C_6 \times X^2}{2 \times EI} + \frac{C_7 \times X}{EI} + \frac{C_8}{EI}\,. \tag{8}$$

In these equations, W_1 and W_2 are the uniformly distributed load on span 1 and 2, respectively; C_1 to C_8 is the integration constants; X is the distance from start of span 1 or 2 to required point of analysis; EI is the flexural registry of the span section, modulus of elasticity multiplied by moment of inertia around the moment axis; L_1 and L_2 are span 1 and 2 lengths, respectively,

Refer to Fig. 1 for loading, shear, moment, slope and deflection diagrams for two-span continuous girder bridges with uniformly distributed loads.

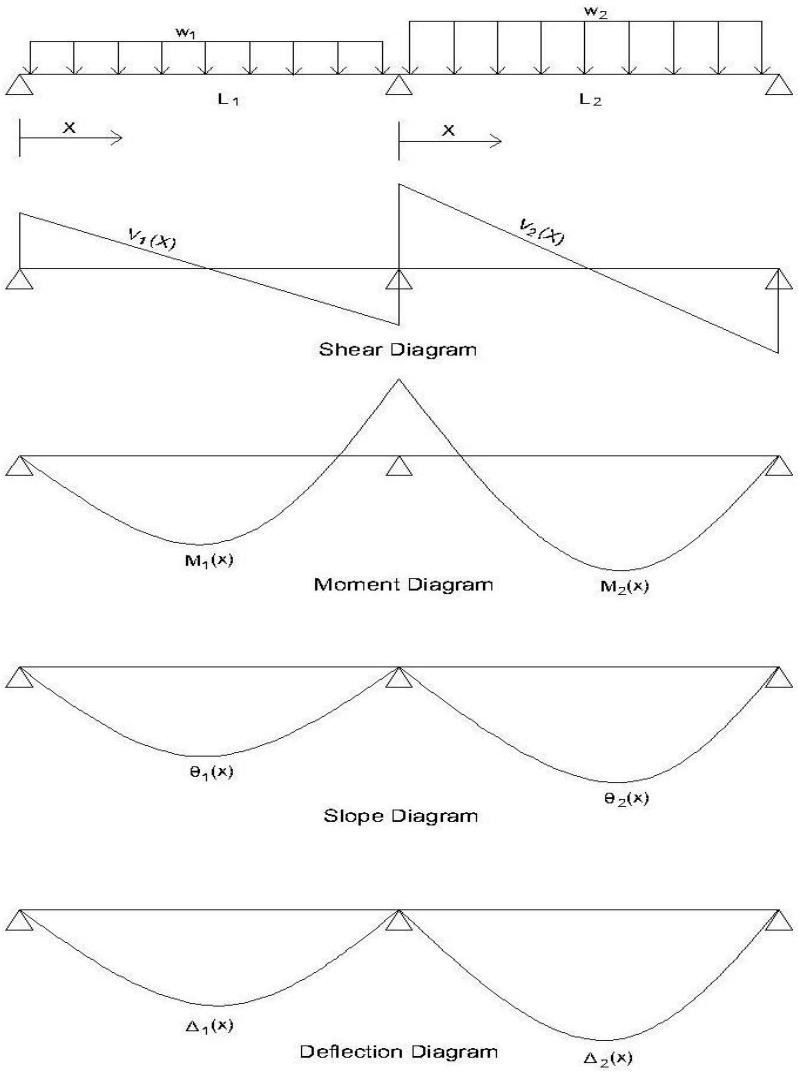

Fig. 1. Loading and analysis diagrams (shear, moment, slope and deflection) for uniformly distributed loading.

As shown, each integration process leads to one integration constant, the number of these unknown constants is eight which equals to number of spans (two) multiplied by four (number of integration constants for each step), to solve these constants, same number of equations must be formulated based on geometry, loading and boundary conditions as follows:

Moment at end span 1 is equal the moment at start span 2 (moment continuity at support).

$$\frac{W1\times L_1^2}{2} + C_1 \times L_1 + C_2 - C_6 = 0\,. \quad (9)$$

Slope at end of span 1 is equal the slope at start of span 2 (rotation continuity at support).

$$\frac{W_1\times L_1^3}{6\times EI} + \frac{C_1\times L_1^2}{2\times EI} + \frac{C_2\times L_1}{EI} + \frac{C_3}{EI} - \frac{C_7}{EI} = 0\,. \quad (10)$$

Deflection at end of span 1 is equal zero:

$$\frac{W_1\times L_1^4}{24\times EI} + \frac{C_1\times L_1^3}{6\times EI} + \frac{C_2\times L_1^2}{2\times EI} + \frac{C_3\times L_1}{EI} + \frac{C_4}{EI} = 0\,. \quad (11)$$

Deflection at end of span 2 is equal zero (pinned):

$$\frac{W_2\times L_2^4}{24\times EI} + \frac{C_5\times L_2^3}{6\times EI} + \frac{C_6\times L_2^2}{2\times EI} + \frac{C_7\times L_2}{EI} + \frac{C_8}{EI} = 0\,. \quad (12)$$

Moment at end of span 2 is equal zero (pinned):

$$\frac{W_2\times L_2^2}{2} + C_5 \times L_2 + C_6 = 0\,. \quad (13)$$

Moment at start of span 1 is equal zero (pinned):

$$\frac{W_1\times 0}{2} + C_1 \times 0 + C_2 = 0\,. \quad (14)$$

Deflection at start of span 1 is equal zero (pinned):

$$\frac{W_1\times 0}{24\times EI} + \frac{C_1\times 0}{6\times EI} + \frac{C_2\times 0}{2\times EI} + \frac{C_3\times 0}{EI} + \frac{C_4}{EI} = 0\,. \quad (15)$$

Deflection at start of span 2 is equal zero:

$$\frac{W_2\times 0}{24\times EI} + \frac{C_5\times 0}{6\times EI} + \frac{C_6\times 0}{2\times EI} + \frac{C_7\times 0}{EI} + \frac{C_8}{EI} = 0\,. \quad (16)$$

Solving these equations, will give the values of integration constants thus defines the analysis equations for each span as follows:

$$C_1 = \frac{3\times W_1\times L_1^3 - W_2\times L_2^3 + 4\times W_1\times L_1^2\times L_2}{8\times L_1(L_2+L_1)}, \quad (17)$$

$$C_2 = 0\,, \quad (18)$$

$$C_3 = \frac{W_1\times L_1^3 - 4\times C_1\times L_1^2}{24}, \quad (19)$$

$$C_4 = 0\,, \quad (20)$$

$$C_5 = \frac{W_1\times L_1^2 + W_2\times L_2^2 - 2\times C_1\times L_1}{2\times L_2}, \quad (21)$$

$$C_6 = \frac{2\times C_1\times L_1 - W_1\times L_1^2}{2}, \quad (22)$$

$$C_7 = \frac{8\times C_1\times L_1^2 - 3\times W_1\times L_1^3}{24}, \quad (23)$$

$$C_8 = 0\,. \quad (24)$$

4. Second Stage (Concentrated Loading)

The location of concentrated load divides the span to two, a is the distance from start of span 1 or end of span 2 to the location of this concentrated load of *P* value, the load within all three segments will be zero, thus the shear will be constant with a different value on each segment, the moment in turns to be linear, the slope is 2nd order polynomial equation and deflection is third order polynomial equation, as follows:

$$V_1(x) = C_1\,, \quad (25)$$

$$M_1(x) = C_1 \times X + C_2\,, \quad (26)$$

$$\theta_1(x) = \frac{C_1\times X^2}{2\times EI} + \frac{C_2\times X}{EI} + \frac{C_3}{EI}, \quad (27)$$

$$\Delta_1(x) = \frac{C_1\times X^3}{6\times EI} + \frac{C_2\times X^2}{2\times EI} + \frac{C_3\times X}{EI} + \frac{C_4}{EI}, \quad (28)$$

$$V_2(x) = C_5\,, \quad (29)$$

$$M_2(x) = C_5 \times X + C_6\,, \quad (30)$$

$$\theta_2(x) = \frac{C_5\times X^2}{2\times EI} + \frac{C_6\times X}{EI} + \frac{C_7}{EI}, \quad (31)$$

$$\Delta_2(x) = \frac{C_5\times X^3}{6\times EI} + \frac{C_6\times X^2}{2\times EI} + \frac{C_7\times X}{EI} + \frac{C_8}{EI}, \quad (32)$$

$$V_3(x) = C_9\,, \quad (33)$$

$$M_3(x) = C_9 \times X + C_{10}\,, \quad (34)$$

$$\theta_3(x) = \frac{C_9\times X^2}{2\times EI} + \frac{C_{10}\times X}{EI} + \frac{C_{11}}{EI}, \quad (35)$$

$$\Delta_3(x) = \frac{C_9\times X^3}{6\times EI} + \frac{C_{10}\times X^2}{2\times EI} + \frac{C_{11}\times X}{EI} + \frac{C_{12}}{EI}. \quad (36)$$

In these equations, $V_1(X)$, $V_2(X)$, $V_3(X)$ are the shear equations; $M_1(X)$, $M_2(X)$, $M_3(X)$ are the moment equations; $\theta_1(X)$, $\theta_2(X)$, $\theta_3(X)$ are the slope equations; Δ_1(X), $\Delta_2(X)$, $\Delta_3(X)$ are the deflection equations; C_1-C_{12} are the integration constants in parts 1, 2 and 3, respectively.

Refer to Fig. 2 for loading, shear, moment, slope and deflection diagrams for two-span continuous girder bridge with concentrated load.

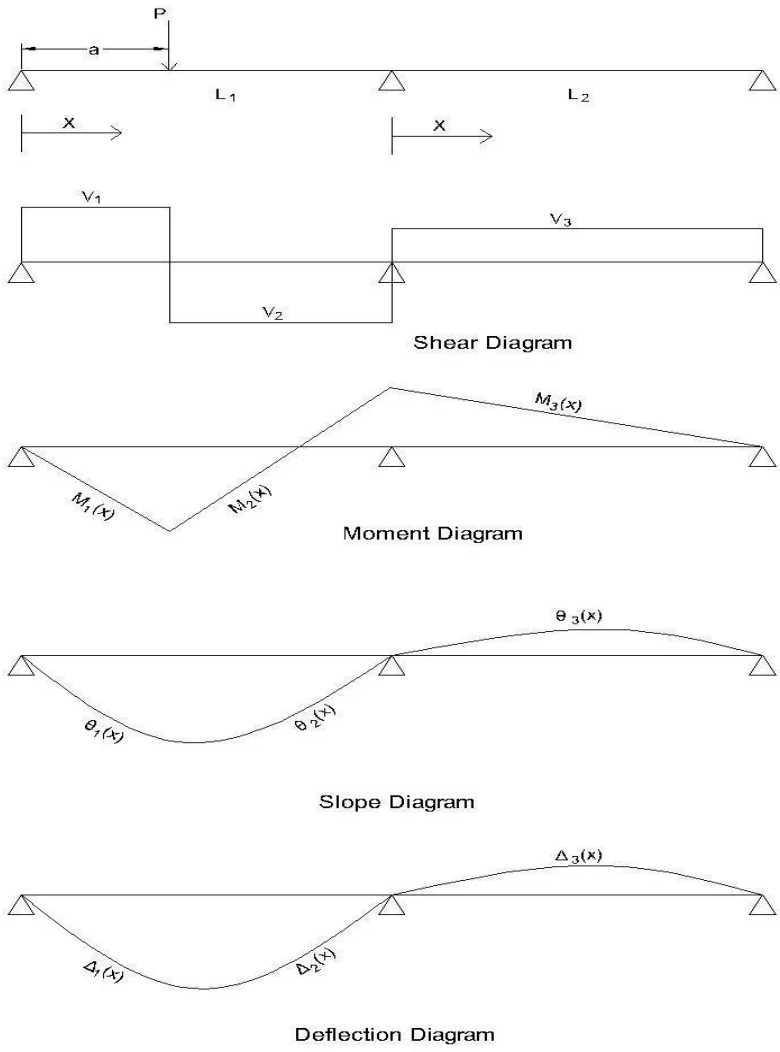

Fig. 2. Loading and analysis diagrams (shear, moment, slope and deflection) for concentrated load.

Twelve unknown constants produced to define the analysis equation for three segments in two spans, twelve equations will be formulated to solve these constants as follows:

The difference of shear at the concentrated load is equal to *P* load value:

$$C_1 - C_5 = P\,. \tag{37}$$

The moment at concentrated load is equal from two directions (moment continuity):

$$C_1 \times a + C_2 - C_6 = 0\,. \tag{38}$$

The slope at concentrated load is equal from two directions (rotation equality):

$$\frac{C_1 \times a^2}{2 \times EI} + \frac{C_2 \times a}{EI} + \frac{C_3}{EI} - \frac{C_7}{EI} = 0\,. \tag{39}$$

The deflection at concentrated load is equal from two directions:

$$\frac{C_1 \times a^3}{6 \times EI} + \frac{C_2 \times a^2}{2 \times EI} + \frac{C_3 \times a}{EI} + \frac{C_4}{EI} - \frac{C_8}{EI} = 0\,. \tag{40}$$

Moment is equal at interior support (moment continuity):

$$C_5 \times (L_1 - a) + C_6 - C_{10} = 0\,. \tag{41}$$

Slope is equal at interior support (rotation continuity):

$$\frac{C_5 \times (L_1 - a)^2}{2 \times EI} + \frac{C_6 \times (L_1 - a)}{EI} + \frac{C_7}{EI} - \frac{C_{11}}{EI} = 0\,. \tag{42}$$

Deflection at the end of span 1 is equal zero (at support):

$$\frac{C_5 \times (L_1 - a)^3}{6 \times EI} + \frac{C_6 \times (L_1 - a)^2}{2 \times EI} + \frac{C_7 \times (L_1 - a)}{EI} + \frac{C_8}{EI} = 0\,. \tag{43}$$

Moment is equal zero at end of span 2 (pinned):

$$C_9 \times L_2 + C_{10} = 0\,. \tag{44}$$

Deflection at the end of span 2 is equal zero (at support):

$$\frac{C_9 \times {L_2}^3}{6 \times EI} + \frac{C_{10} \times {L_2}^2}{2 \times EI} + \frac{C_{11} \times L_2}{EI} + \frac{C_{12}}{EI} = 0\,. \tag{45}$$

Moment is equal zero at start of span 1 (pinned):

$$C_1 \times 0 + C_2 = 0\,. \tag{46}$$

Deflection at the start of span 1 is equal zero (at support):

$$\frac{C_1\times 0}{6\times EI} + \frac{C_2\times 0}{2\times EI} + \frac{C_3\times 0}{EI} + \frac{C_4}{EI} = 0\,. \tag{47}$$

Deflection at the start of span 2 is equal zero (at support):

$$\frac{C_9\times 0}{6\times EI} + \frac{C_{10}\times 0}{2\times EI} + \frac{C_{11}\times 0}{EI} + \frac{C_{12}}{EI} = 0\,, \tag{48}$$

In these equations, a is the distance between start of span 1 to location of concentrated load if it is in span 1 or the distance between end of span 2 to location of concentrated load if it is in span 2 and P is the concentrated load.

Solving these equations will give the values of these constants as follows:

$$C_1 = P \times \left[\frac{a^3 - a(3{L_1}^2 + 2L_1L_2)}{2\times L_1^2\times(L_1+L_2)} + 1\right], \tag{49}$$

$$C_2 = 0\,, \tag{18}$$

$$C_4 = 0\,, \tag{20}$$

$$C_{10} = a \times C_1 + (C_1 - P) \times (L_1 - a)\,, \tag{50}$$

$$C_5 = C_1 - P\,, \tag{51}$$

$$C_6 = a \times C_1\,, \tag{52}$$

$$C_9 = \frac{-a\times C_1 - (C1-P)\times(L1-a)}{L_2}, \tag{53}$$

$$C_3 = \frac{-3a^2C_1 - 3\times(L_1-a)^2\times(C_1-P) - 6\times a\times C_1(L_1-a) - 2\times L_2\times a\times C_1 - 2L_2\times(C1-P)\times(L1-a)}{6}, \tag{54}$$

$$C_{11} = \frac{-L_2\times a\times C_1 - L_2\times(C_1-P)\times(L_1-a)}{3}, \tag{55}$$

$$C_{12} = 0\,, \tag{56}$$

$$C_7 = \frac{-3\times(L_1-a)^2\times(C_1-P) - 6\times a\times C_1(L_1-a) - 2\times L_2\times a\times C_1 - 2\times L_2\times(C1-P)\times(L1-a)}{6}, \tag{57}$$

$$C_8 = \frac{2\times(L_1-a)^3\times(C_1-P) + 3\times a\times C_1\times(L_1-a)^2 + 2\times L_2\times a\times C_1\times(L_1-a) + 2L_2\times(C1-P)\times(L1-a)^2}{6}. \tag{58}$$

5. Third Stage (Single Moving Load)

In this section, the analysis envelope equations were derived for single moving load for each span based on the analysis equations for a single concentrated load derived in previous section, the motion of load in span 1 starts from beginning of span 1 to end of span 1, the motion of load in span 2 starts from end of span 2 to beginning of span 2 as shown in Fig. 3.

5.1. Shear envelope equations

The maximum shear at any point in a span length when single concentrated load is moving on that span occurs when moving load acts on that point, the maximum positive and negative shear at any point is equal the positive and negative shear of the single concentrated load at this point, which means C_1 (Eq. (49)) at this point for maximum positive shear, and C_5 (Eq. (51)) at the same point for maximum negative shear, replacing a (location of concentrated load) with X as follows:

$$PVE_1(X) = P \times \left[\frac{X^3 - X\times(3\times L_1^2 + 2\times L_1\times L_2)}{2\times L_1^2\times(L_1+L_2)} + 1\right],$$

$$0 \le X \le L_1\,, \tag{59}$$

$$NVE_1(X) = P \times \left[\frac{X^3 - X\times(3\times L_1^2 + 2\times L_1\times L_2)}{2\times L_1^2\times(L_1+L_2)}\right],$$

$$0 \le X \le L_1\,. \tag{60}$$

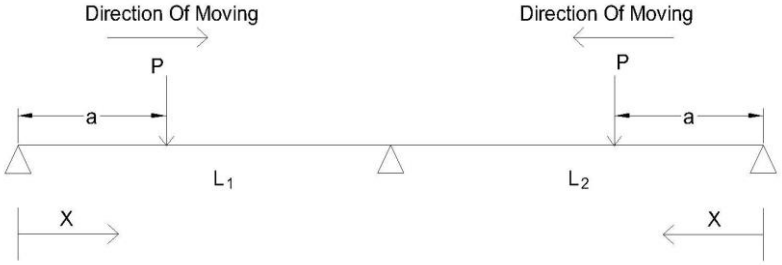

Fig. 3. Single moving load diagram.

The same equations are applicable in span 2 but replacing L_1 with L_2, and vice versa, X start from zero (end of span 2) to L_2 (start of span 2) as follows:

$$PVE_2(X) = P \times \left[\frac{X^3 - X\times(3\times L_2^2 + 2\times L_1\times L_2)}{2\times L_2^2\times(L_1+L_2)} + 1\right],$$

$$0 \le X \le L_2\,, \tag{61}$$

$$NVE_2(X) = P \times \left[\frac{X^3 - X\times(3\times L_2^2 + 2\times L_1\times L_2)}{2\times L_2^2\times(L_1+L_2)}\right],$$

$$0 \le X \le L_2\,. \tag{62}$$

In these equations, $PVE_1(X)$ is the positive shear envelope equation for span 1; $NVE_1(X)$ is the negative shear envelope equation for span 1; $PVE_2(X)$ is the positive shear envelope equation for span 2; $NVE_2(X)$ is the negative shear envelope equation for span 2.

Refer to Fig. 4 for Positive and negative shear envelope diagrams for both spans with single moving load.

5.2. Moment envelope equations

The maximum negative moment (downward) in each span at any point occurs when moving load acts on that point, replacing a with X in the moment equation for concentrated load at any point will give the moment envelope equation as 4th degree polynomial equation for each span as follows:

$$NME_1(X) = P \times X \times \left[\frac{X^3 - X(3{L_1}^2 + 2L_1L_2)}{2\times L_1^2\times(L_1+L_2)} + 1\right],$$

$$0 \le X \le L_1\,, \tag{63}$$

$$NME_2(X) = P \times X \times \left[\frac{X^3 - X(3{L_2}^2 + 2L_1L_2)}{2\times L_2^2\times(L_1+L_2)} + 1\right],$$

$$0 \le X \le L_2\,. \tag{64}$$

In these equations, $NME_1(X)$ is the negative moment envelope equation in for span 1 and $NME_2(X)$ is the negative moment envelope equation in for span 2.

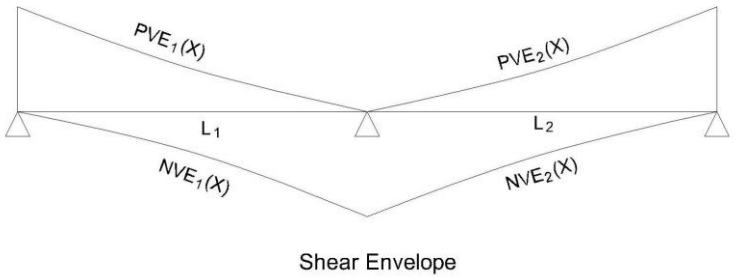

Fig. 4. Shear envelope diagram for single moving load.

The maximum positive moment will occur generally when the concentrated load acts on the other span. In case of equal span lengths (L_1=L_2),the positive moment envelope equation will be line extending from the maximum positive moment at interior support (*MPMIS*) due to moving load to the end of span (zero moment at pinned) based on the shape of positive moment equation for the concentrated load on the another span, by Replacing a with X in the moment equation for concentrated load at the location of interior support, refer to Eq. (34), and derive this equation according to X , equal this equation by zero to find the X which gives the location of moving load that producing the maximum positive moment at interior support, substituting this value in previous equation (Eq. (34)) will give the maximum positive moment at interior support. Thus defines the positive moment envelope equation as follows:

If $L_1 = L_2 = L$,

$$a = \frac{L}{\sqrt{3}}, \tag{65}$$

$$MPMIS = \frac{L\times P}{6\times\sqrt{3}}\,, \tag{66}$$

where, *MPMIS* is the maximum positive moment at interior support.

Refer to Fig. 5 for positive and negative moment envelope diagram for both spans with single moving load for equal span case.

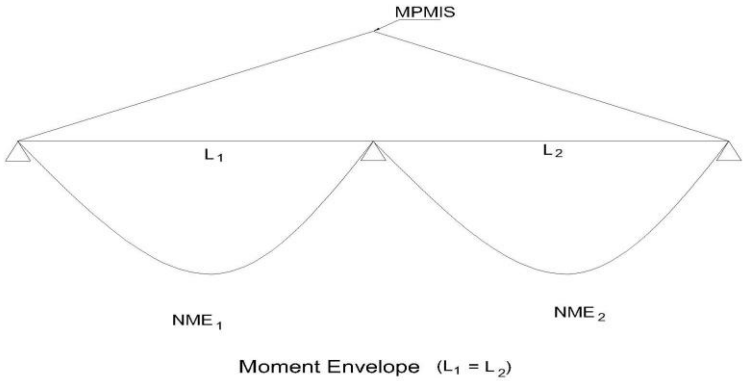

Fig. 5. Moment envelope diagram for single moving load when L_1=L_2.

In case of unequal spans, the positive moment envelope equation is divided into two lines on the longer span and one line for shorter span, due to that maximum positive moment at interior support on longer span will come from moving load on the same span not on the other one, the derivation of maximum positive moment at interior support (*MPMIS*) is derived as discussed above when moving load acts on the longer span only, the derivation of the maximum positive moment near the interior support on the longer span (*MPMNIS*) is the same as in equal span case when moving load acts on shorter span only, by deriving these values, the location of intersection of two positive moment line equations (*POI*) can be found as follows:

If $L_1 > L_2$,

$$a = \frac{L_1}{\sqrt{3}}, \tag{67}$$

$$MPMIS = \frac{L_1 \times P}{6 \times \sqrt{3}}\ , \tag{68}$$

$$MPMNIS = \frac{L_1^2 \times P}{3 \times \sqrt{3} \times (L_1 + L_2)}, \tag{69}$$

$$POI = \frac{\frac{L_1^4 - L_2^4}{3 \times \sqrt{3} \times \left(L_1^3 + L_2 \times L_1^2\right)}}{\frac{3 \times (3 \times L_1 + 2 \times L_2) - L_1}{6 \times \sqrt{3} \times (L_1 + L_2)} - \frac{2 \times L_2^2}{6 \times \sqrt{3} \times L_1 \times (L_2 + 2 \times L_1)}}, \tag{70}$$

where, *MPMNIS* is the maximum positive moment near interior support; *POI* is the point of intersection.

Refer to Fig. 6 for positive and negative moment envelope diagram for both spans with single moving load when $L_1 > L_2$.

If $L_1 < L_2$,

$$a = \frac{L_2}{\sqrt{3}}, \tag{71}$$

$$MPMIS = \frac{L_2 \times P}{6 \times \sqrt{3}}\ , \tag{72}$$

$$MPMNIS = \frac{L_2^2 \times P}{3 \times \sqrt{3} \times (L_1 + L_2)}, \tag{73}$$

$$POI = \frac{\frac{L_2^4 - L_1^4}{3 \times \sqrt{3} \times \left(L_2^3 + L_1 \times L_2^2\right)}}{\frac{3 \times (3 \times L_2 + 2 \times L_1) - L_2}{6 \times \sqrt{3} \times (L_1 + L_2)} - \frac{2 \times L_1^2}{6 \times \sqrt{3} \times L_2 \times (L_1 + 2 \times L_2)}}. \tag{74}$$

Refer to Fig. 7 for Positive and negative moment envelope diagram for both spans with single moving load when $L_1 < L_2$.

5.3. Maximum envelope deflection

During load moving, the maximum deflection at each point occurs when slope (θ) is equal zero, there is only one point on each span where maximum deflection occurs at same location of moving load, this point will be called point of maximum envelope deflection (*PMED*), this point divides the span into two parts, the first one, where the maximum deflection occurs after any required point in that part, the second part, where the maximum deflection occurs before any required point in that part, the maximum envelope deflection at each span occurs at the point of maximum envelope deflection (*PMED*).

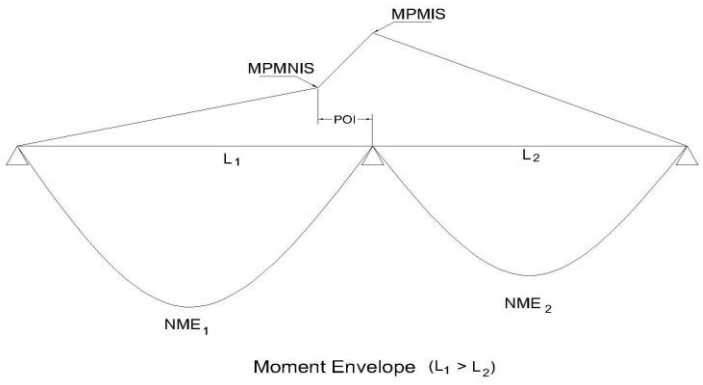

Fig. 6. Moment envelope diagram for single moving load when $L_1 > L_2$.

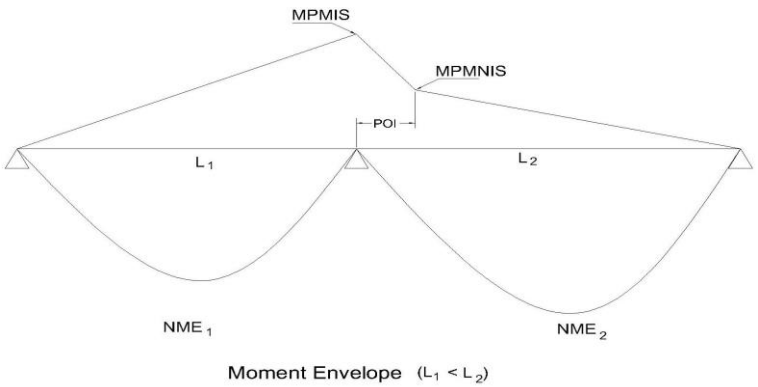

Fig. 7. Moment Envelope diagram for single moving load when $L_1 < L_2$.

The *PMED* occurs at the location of moving load where the slope value is equal zero under this load, this can be derived by equaling the slope equation at moving load location a by zero, the following demonstration is for span 1:

$$\theta_1 = \frac{C_1 \times a^2}{2 \times EI} + \frac{C_2 \times a}{EI} + \frac{C_3}{EI} = 0\,, \tag{75}$$

$$\frac{3\times a\times P\times L_1^3+3\times a^3\times P\times L_1+4\times L_1^2\times L_2\times P\times a+2\times a^3\times P\times L_2-6\times a^2\times L_1^2\times P-6\times a^2\times P\times L_2\times L_1}{12\times L_1^2+12\times L_1\times L_2} - \frac{a^2\times C_1}{2} = 0\,, \tag{76}$$

$$\frac{a\times[12\times a^2\times P\times L_1^2+8\times a^2\times P\times L_1\times L_2-12\times L_1^3\times P\times a-12\times a\times P\times L_2\times L_1^2+3\times P\times L_1^4+4\times L_1^3\times L_2\times P-3\times a^4\times P]}{12\times L_1^3+12\times L_1^2\times L_2} = 0\,, \tag{77}$$

Solving this equation to obtain the location of *PMED* directly is hard, instead of that, the variable a will be replaced with $R_1 \times L_1$ and L_2 with $R_2 \times L_1$.

$$R_1 = \frac{a}{L_1}, \tag{78}$$

$$R_2 = \frac{L_2}{L_1}, \tag{79}$$

where, R_1 is the ratio between the location of moving load (a) and span 1 length (L_1); R_2 is the ratio of span 2 length (L_2) with span 1 length (L_1).

Converting the above equation into following form:

$$Y = L_1^4 \times [12 \times R_1^2 + 8 \times R_1^2 \times R_2 - 12 \times R_1 - 12 \times R_1 \times R_2 + 3 + 4 \times R_2 - 3 \times R_1^4]\,. \tag{80}$$

Substituting R_2 with a range of values from 0.1 to 10, and finding the intersection of Y curve with X-axis for each value of R_2 to find the value of R_1 that makes the above equation is zero, arranging R_1 values with R_2 values, gives a curve that defines the relationship between span 1 length to span 2 length ratio (R_2) and the location of *PMED* as a ratio of span length where deflection is to be calculated (R_1), substituting this value in a parameter in deflection equation (Eq. (28) or Eq. (32))for concentrated load to obtain the value of *PMED*.

Refer to Fig. 8 for relationship of R_2 (X-axis) with R_1 (Y-axis) for location of point of maximum deflection (*PMED*).

The same equations and curve used to derive the point of maximum envelope deflection *PMED* in span1 was used in span 2 by replacing L_1 with L_2 and vice versa as follows:

$$R_1 = \frac{a}{L_2}, \tag{81}$$

$$R_2 = \frac{L_1}{L_2}. \tag{82}$$

In case of equal span length (L_1=L_2=L), R_1 is equal 0.46875, Substituting a=0.46875×L in X and a in Eq. (28) or Eq. (32) (and in corresponding integration constants equations) gives the same value of *PMED* for both spans 1 and 2.

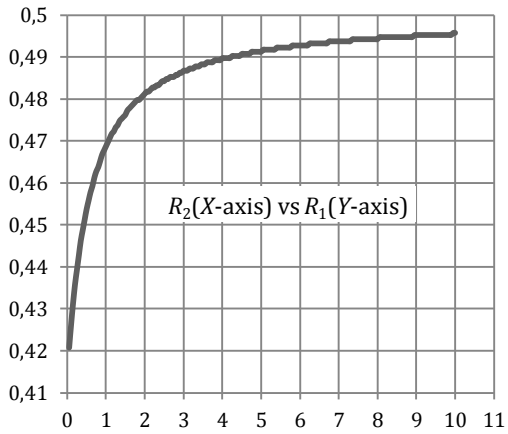

Fig. 8. Relationship between R_2 and R_1 for single moving load.

6. Fourth Stage (Multiple Moving Load)

In this stage, Analysis envelope equations for multiple loads will be derived based on the single load derivations, refer to Fig. 9 for three moving loads diagram.

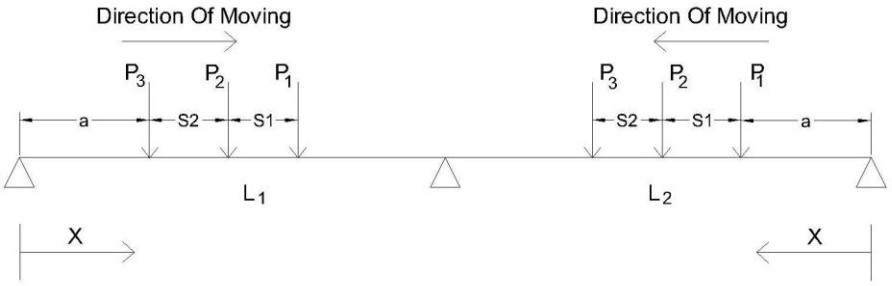

Fig. 9. Three moving loads diagram.

6.1. Shear envelope equations

The maximum positive shear at any point in span 1 due to moving of multiple loads occurs when the last load (P_3) acts on it as follows:

$$P(X) = \sum_{N=1}^{M} P_N \times \left[\frac{\left(X+\sum_{N}^{M-1} S_N\right)^3 - \left(X+\sum_{N}^{M-1} S_N\right) \times \left(3\times L_1^2 + 2\times L_1 \times L_2\right)}{2\times L_1^2 \times (L_1+L_2)} + 1 \right] \ , \ 0 \le X \le L_1 \ . \tag{83}$$

The maximum negative shear at any point in span 1 due to moving of multiple loads occurs when the first load acts (P_1) on it as follows:

$$NVE_1(X) = \sum_{N=1}^{M} P_N \times \left[\frac{\left(X-\sum_{1}^{N-1} S_N\right)^3 - \left(X-\sum_{1}^{N-1} S_N\right) \times \left(3\times L_1^2 + 2\times L_1 \times L_2\right)}{2\times L_1^2 \times (L_1+L_2)} \right] \ , \ 0 \le X \le L_1 \ . \tag{84}$$

The maximum positive shear at any point in span 2 due to moving of multiple loads occurs when the first load (P_1) acts on it as follows:

$$PVE_2(X) = \sum_{N=1}^{M} P_N \times \left[\frac{\left(X+\sum_{1}^{N-1} S_N\right)^3 - \left(X+\sum_{1}^{N-1} S_N\right) \times \left(3\times L_2^2 + 2\times L_1 \times L_2\right)}{2\times L_2^2 \times (L_1+L_2)} + 1 \right] \ , \ L_2 \ge X \ge 0 \ . \tag{85}$$

The maximum negative shear at any point in span 2 due to moving of multiple loads occurs when the last load (P_3) acts on it as follows:

$$NVE_2(X) = \sum_{N=1}^{M} P_N \times \left[\frac{\left(X-\sum_{N}^{M-1} S_N\right)^3 - \left(X-\sum_{N}^{M-1} S_N\right) \times \left(3\times L_2^2 + 2\times L_1 \times L_2\right)}{2\times L_2^2 \times (L_1+L_2)} \right] \ , \ L_2 \ge X \ge 0 \ . \tag{86}$$

In these equations, $PVE_1(X)$ is the positive shear envelope equation for span 1; $NVE_1(X)$ is the negative shear envelope equation for span 1; $PVE_2(X)$ is the positive shear envelope equation for span 2; $NVE_2(X)$ is the negative shear envelope equation for span 2; S_N is the distance between N wheel axis loads; P_N is the wheel axial load number N; M is the total number of wheel loads.

6.2. Moment envelope equations

The maximum negative moment at each point on both spans, occur when one of any multiple moving load acts on it due to moment diagram shape for multiple concentrated load (vertex of moment diagram), for demonstration, three moving loads (most general wheel load, truck load) were taken, and accordingly the negative moment envelope equations were developed.

The maximum negative moment at any point on span length can be caused by one of the three moving loads acting on it directly, three moment envelope equations were developed by taking each load acting on required point, the other loads will add moment to this point according to their value and relative location to demonstrate moving load (Distance between moving loads, axis distance), each distance interval on each span, one of the three negative moment envelope equation will be maximum, thus the resultant negative moment envelope equation is the maximum of the three developed negative moment envelope equation at any point as follows ($0 \le X \le L_1$):

$$NME_{1P1}(X) = X \times \left\{ \begin{array}{c} P_1 \times \left[\frac{X^3 - X\left(3L_1{}^2 + 2L_1L_2\right)}{2\times L_1^2 \times (L_1+L_2)} + 1 \right] + P_2 \times \left[\frac{(X-S_1)^3 - (X-S_1) \times \left(3L_1{}^2 + 2L_1L_2\right)}{2\times L_1^2 \times (L_1+L_2)} + 1 \right] \\ + P_3 \times \left[\frac{(X-S_1-S_2)^3 - (X-S_1-S_2) \times \left(3L_1{}^2 + 2L_1L_2\right)}{2\times L_1^2 \times (L_1+L_2)} + 1 \right] \end{array} \right\}, \tag{87}$$

$$NME_{1P2}(X) = X \times \left\{ \begin{array}{c} P_2 \times \left[\frac{X^3 - X\left(3L_1{}^2 + 2L_1L_2\right)}{2\times L_1^2 \times (L_1+L_2)} + 1 \right] + P_1 \times \left[\frac{(X+S_1)^3 - (X+S_1) \times \left(3L_1{}^2 + 2L_1L_2\right)}{2\times L_1^2 \times (L_1+L_2)} + 1 \right] \\ + P_3 \times \left[\frac{(X-S_2)^3 - (X-S_2) \times \left(3L_1{}^2 + 2L_1L_2\right)}{2\times L_1^2 \times (L_1+L_2)} + 1 \right] \end{array} \right\}, \tag{88}$$

$$NME_{1P3}(X) = X \times \left\{ \begin{array}{c} P_3 \times \left[\frac{X^3 - X\left(3L_1{}^2 + 2L_1L_2\right)}{2\times L_1^2 \times (L_1+L_2)} + 1 \right] + P_2 \times \left[\frac{(X+S_2)^3 - (X+S_2) \times \left(3L_1{}^2 + 2L_1L_2\right)}{2\times L_1^2 \times (L_1+L_2)} + 1 \right] \\ + P_1 \times \left[\frac{(X+S_1+S_2)^3 - (X+S_1+S_2) \times \left(3L_1{}^2 + 2L_1L_2\right)}{2\times L_1^2 \times (L_1+L_2)} + 1 \right] \end{array} \right\}. \tag{89}$$

In these equations, $NME_{1P1}(X)$ is the negative moment envelope equation for span 1 as load P_1 is the main load; $NME_{1P2}(X)$ is the Negative moment envelope equation for span 1 as load P_2 is the main load; $NME_{1P3}(X)$ is the Negative moment envelope equation for span 1 as load P_3 is the main load; P_1, P_2, P_3 are the moving loads (represent vehicle axis loads); S_1, S_2 is the distance between P_1 and P_2, the distance between P_2 and P_3 respectively.

The same concept applied in span 2, by replacing L_1 with L_2 and vice versa, as follows ($0 \le X \le L_2$):

$$NME_{2P1}(X) = X \times \left\{ \begin{array}{c} P_1 \times \left[\frac{X^3 - X\left(3{L_1}^2 + 2L_1L_2\right)}{2 \times L_2^2 \times (L_1 + L_2)} + 1 \right] + P_2 \times \left[\frac{(X+S_1)^3 - (X+S_1) \times \left(3{L_1}^2 + 2L_1L_2\right)}{2 \times L_2^2 \times (L_1 + L_2)} + 1 \right] \\ + P_3 \times \left[\frac{(X+S_1+S_2)^3 - (X+S_1+S_2) \times \left(3{L_1}^2 + 2L_1L_2\right)}{2 \times L_2^2 \times (L_1 + L_2)} + 1 \right] \end{array} \right\}, \tag{90}$$

$$NME_{2P2}(X) = X \times \left\{ \begin{array}{c} P_2 \times \left[\frac{X^3 - X\left(3{L_1}^2 + 2L_1L_2\right)}{2 \times L_2^2 \times (L_1 + L_2)} + 1 \right] + P_1 \times \left[\frac{(X-S_1)^3 - (X-S_1) \times \left(3{L_1}^2 + 2L_1L_2\right)}{2 \times L_2^2 \times (L_1 + L_2)} + 1 \right] \\ + P_3 \times \left[\frac{(X+S_2)^3 - (X+S_2) \times \left(3{L_1}^2 + 2L_1L_2\right)}{2 \times L_2^2 \times (L_1 + L_2)} + 1 \right] \end{array} \right\}, \tag{91}$$

$$NME_{2P3}(X) = X \times \left\{ \begin{array}{c} P_3 \times \left[\frac{X^3 - X\left(3{L_1}^2 + 2L_1L_2\right)}{2 \times L_2^2 \times (L_1 + L_2)} + 1 \right] + P_2 \times \left[\frac{(X-S_2)^3 - (X-S_2) \times \left(3{L_1}^2 + 2L_1L_2\right)}{2 \times L_2^2 \times (L_1 + L_2)} + 1 \right] \\ + P_1 \times \left[\frac{(X-S_1-S_2)^3 - (X-S_1-S_2) \times \left(3{L_1}^2 + 2L_1L_2\right)}{2 \times L_2^2 \times (L_1 + L_2)} + 1 \right] \end{array} \right\}. \tag{92}$$

For the positive moment envelope equation for multiple moving loads, another approach was followed which is to consider the location of multiple loads as the same of the location of centroid of these loads, to calculate the maximum positive moment at interior support (*MPMIS*), centroid of multiple loads put on a distance as given by Eqs. (65), (67) or (71) depending which span is longer, MPMIS is equal the sum of moments caused by each load on their specific location as described in moment equation of concentrated load case, to calculate the maximum positive moment near interior support (*MPMNIS*), the centroid of multiple load put on *POI* as defined in Eqs. (70) or (74) according to span length case. *MPMNIS* is equal the sum of moments caused by each load on their specific location according to moment equation for concentrated load case.

6.3. Maximum envelope deflection

To calculate the maximum envelope deflection for multiple moving load, the centroid of these loads are put on the point of maximum envelope deflection (*PMED*) as shown in section 5.3 according to span length case, then the deflection was calculated by summing the deflection caused by each load on their specified location at *PMED* point as shown in deflection equations for concentrated load.

7. Conclusions

Bridge engineers can follow the equations presented in this paper to conduct complete analysis for two-span continuous girder bridge in uniformly distributed loading and wheel loading for any number of axis loads without using a software with more accuracy, making the bridge girder analysis more practical and accurate.

The future challenge in this field is to find direct analysis envelope equations for girder bridges with more than two spans with wider boundary conditions such as support settlement or deformation in the bearing pad.

References

Barker R, Puckett J (2013). Design of Highway Bridges: An LRFD Approach (2nd edition). John Wiley & Sons Inc., New York.

Fu CC, Wang S (2014). Computational Analysis and Design of Bridge Structures. CRC Press, Boca Raton.

Gambhir ML (2011). Fundamentals of Structural Mechanics and Analysis. Prentice-Hall Inc., Englewood Cliffs, NJ.

Hibbeler RC (2005). Mechanics of Materials (6th edition). Prentice-Hall Inc., Englewood Cliffs, NJ.

Liew JYR, Shanmugam NE (2005). Structural Analysis. *In: Chen WF, Lui EM, editors. Handbook of Structural Engineering* (*2nd edition*). CRC Press, Boca Raton.

Rattan SS (2008). Strength of Materials. McGraw-Hill, New York.

Wieland M, Malla S (2015). Earthquake design of a viaduct with full seismic isolation of bridge deck. *Challenge Journal of Structural Mechanics*, 1(1), 27–31.

Challenge Journal of Structural Mechanics

Warning time analysis for emergency response in Sakarya city, Turkey against possible Marmara earthquake

Hüseyin Serdar Küyük *

Department of Civil Engineering, Sakarya University, 54187 Sakarya, Turkey
Department of Earthquake Engineering, Kandilli Observatory and Earthquake Engineering Institute, Bogaziçi University, 34684 Istanbul, Turkey

ABSTRACT

Sakarya, one of the biggest cities in the Marmara prefecture, with 835 thousand population has suffered severe damages due to the North Anatolian Fault System (NAFS) which is a major active right lateral-moving fault in northern Anatolia running along the tectonic boundary between the Eurasian Plate and the Anatolian Plate. One of the biggest disasters was on 17 August 1999 Izmit earthquake with M_w 7.4. The occurrence and the source information of huge events in the region indicate that an earthquake is expecting in near future from the underneath of the Marmara Sea. Therefore, this seismically vulnerable city needs urgent strong motion prediction and reliable Earthquake Early Warning System. The city is preparing now for further NAFS earthquakes and it is essential to inform society about the warning time of a possible imminent earthquake so that precautionary actions can be taken by the government officials, companies and individuals. This study highlights available warning time for the city. Warning time is calculated by considering the theoretic P- and S- wave velocities for Marmara region. Results indicate that Sakarya will have approximately 37.9 second in average with 7.4 second standard deviation before the arrival of strong shaking to the city.

ARTICLE INFO

Article history:
Received 28 May 2015
Accepted 12 July 2015

Keywords:
Warning time
Earthquake early warning
North Anatolian fault
Marmara earthquakes

1. Introduction

The Marmara region, north-east of Turkey, is bounded by approximately longitudes of 26° to 31° and latitudes of 40° to 41°30'. It has a number of structural highlands and basins such as the Kocaeli, Strandja, Rhodope, Ganos, Gelibolu, Kapıdağ, Uludağ and Armutlu blocks and the intervening fault-controlled basins to sea ways, such as the Izmit-Sapanca, Adapazarı, Geyve, İznik, Gemlik, İnegöl, Bursa, Saros and Ergene basins, the Sea of Marmara, and the Dardanelles to Bosphorus.

Seismicity of the Marmara region is comparatively high as pointed out by both the historical and recent devastative earthquakes. 18 historical earthquakes with intensities of IX to X in the period of 29 AD to 1894, and 13 recent earthquakes with magnitudes of 6.1 to 7.4 in the period of 1912 to 1999 occurred in the Marmara region. These statistics correspond to the occurrence of an approximately 1/100 years historical and 1/7 years recent destructive earthquakes in the Marmara region (Koçyiğit, 2000). Since, more or less one to fourth of Turkey's population and most of industry are built-in in this region, this high rate of seismicity has a critical importance for the earthquake hazard (Fig. 1). The high seismicity and earthquake hazard is due to two contemporaneous neotectonic regimes and related structures in the region. These are the strike-slip and extensional neotectonic regimes characterized by a right lateral strike-slip fault system (the western section of NAFS) and an oblique-slip normal fault zone (Le Pichon et al., 2001).

In both historical and instrumental periods, various fault segments mainly both the North Marmara sub-fault system to the South Marmara sub-fault system reactivated and resulted in large devastative earthquakes. All

* *Corresponding author*. Tel.: +90-264-2955674 ; Fax: +90-264-3460359 ; E-mail address: skuyuk@sakarya.edu.tr (H. S. Küyük)
ISSN: 2149-8024 / DOI: http://dx.doi.org/10.20528/cjsmec.2015.07.024

of these fault segments are capable to produce large and destructive earthquakes and they could be sources of near future earthquakes in the Marmara region (Koçyiğit, 2000).

One of the largest disasters was on 17 August 1999 Golcuk earthquake with M_w 7.4. The occurrence of huge events in the area indicate that a likely earthquake is forthcoming in near future from the underneath of the Marmara Sea. Adapazari, located between Duzce and Golcuk, affected the most from the last catastrophe. It is expected that the next earthquake also will cause enormous consequences. This seismically vulnerable city needs urgent reliable Earthquake Early Warning System. The city is preparing now for further NAFS earthquakes and it is essential to inform society about the warning time of a possible imminent earthquake so that precautionary actions can be taken by the government officials, companies and individuals.

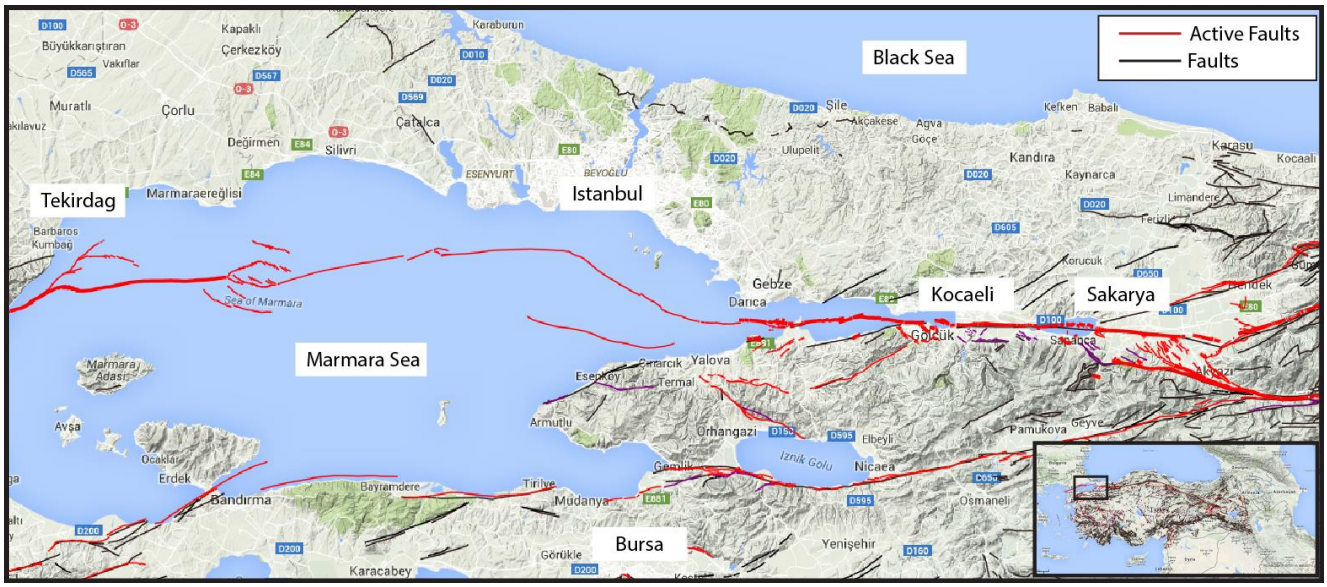

Fig. 1. Active faults segments at Marmara region with long-term seismic gaps (Emre et al., 2013).

Early warning systems give warnings of upcoming danger by rapid estimation of the earthquake source parameters such as magnitude and epicenter (Kuyuk and Allen, 2013a). To do so, systems use the capability of modern real-time systems to process and transmit information faster than seismic wave's propagation (up to 8 km/s). The possible warning time is usually in the range of up to 70 seconds (in Mexico), depending on the distances between seismic source, seismic sensor and user sites (Bose et al., 2014; Kuyuk et al., 2013b).

There have been several expressions used in the literature for this time interval, namely warning time. Various authors used "Alert time", "Warning time", "Available time" in different meanings but the same intentions (Cua and Heaton, 2007). Another difference is the considerations about occurrence of S wave or peak ground motion as a start of strong shaking. Generally "alert time" is defined as onset of P-wave in a nearest station to the fault. The warning time is then the difference between the alert time and the estimated time of S wave for a given location need to be alerted (Kuyuk and Allen, 2013b).

In this study, the available time analysis of likely upcoming offshore earthquake from Marmara Sea is investigated. Available time analysis is performed for Sakarya city by theoretical P- S- wave velocities using three locations Gebze, Kocaeli and Sakarya. P-P wave and S-S wave time difference between near and far sites also investigated. This study could contribute valuable information to public and seismic hazard studies.

2. Methodology

The available warning time of an earthquake Δt can be defined by the time interval between the detection of the P-wave by a sensor in near field and the arrival of energy carrying S-waves at the user site. The epicentral distance E_{user} of the first detection site, E_{user} of the user site and focal depth of earthquake z, the warning time Δt can be estimated by

$$\Delta t = \frac{\sqrt{(E_{user}^2+z^2)}}{v_s} - \frac{\sqrt{(E_{sensor}^2+z^2)}}{v_p} - t_{decision} - t_{transmission}\ , \quad (1)$$

where v_p and v_s are the P and S-wave average velocities and $t_{decision}$, $t_{transmission}$ are the time needed for decision of data processing and data transmission times. These two times are separated here to indicate that transmission is more related to technological problem where decision time is related how the decision maker wants to sure the level of earthquake destructivity.

The warning time depends mainly on two factors: the relative distance of stations to epicenter and velocity of the waves in the region and technical/decisional factors (Horiuchi et al., 2005). The alert of a P wave is generally available after 0.2 seconds of waveform reach the nearest station. Processing delay is assumed as 0.4 seconds (Kuyuk and Motosaka, 2009). This is stands for the transmission of waveform from nearest station to operation center of network.

Current seismic infrastructure with the development of communication technology develops a variable packet for the packetization of waveform data so that delay decreased to the insignificant level. The transmission of data to the processing center is generally less than 0.2 second (Motosaka et al., 2008). The processing time for the transmission can be negligible due to high performance computers.

P and S-wave average velocities (v_p and v_s) are depend on soil structure of earth. Travel time tables for different waves and paths (P, S, PS, PP etc.) through the earth were obtaining repeated observations. Various studies have been done to find out the velocities of P and S wave for the Marmara region due to the attractive and complex structure. The crustal structure and velocity variations in the crust have been examined by using the earthquake and controlled source data with different methods. The review of these studies has been done by Kalafat et al. (1987) and Küleli et al. (1996). It was assumed that average S-wave velocity is 3.69 km/sec and average P-wave velocity is 5.8 km/sec based on previous studies in the region.

Assurance and accuracy of the hazard prediction increases with time after an earthquake, while the time of available warning decreasing. Therefore it is important to calculate the probability of available time in a region where destructivity earthquakes are most likely happens. Here I assessed the distribution of warning times for many likely earthquakes in Marmara offshore earthquakes of Turkey (Fig. 2).

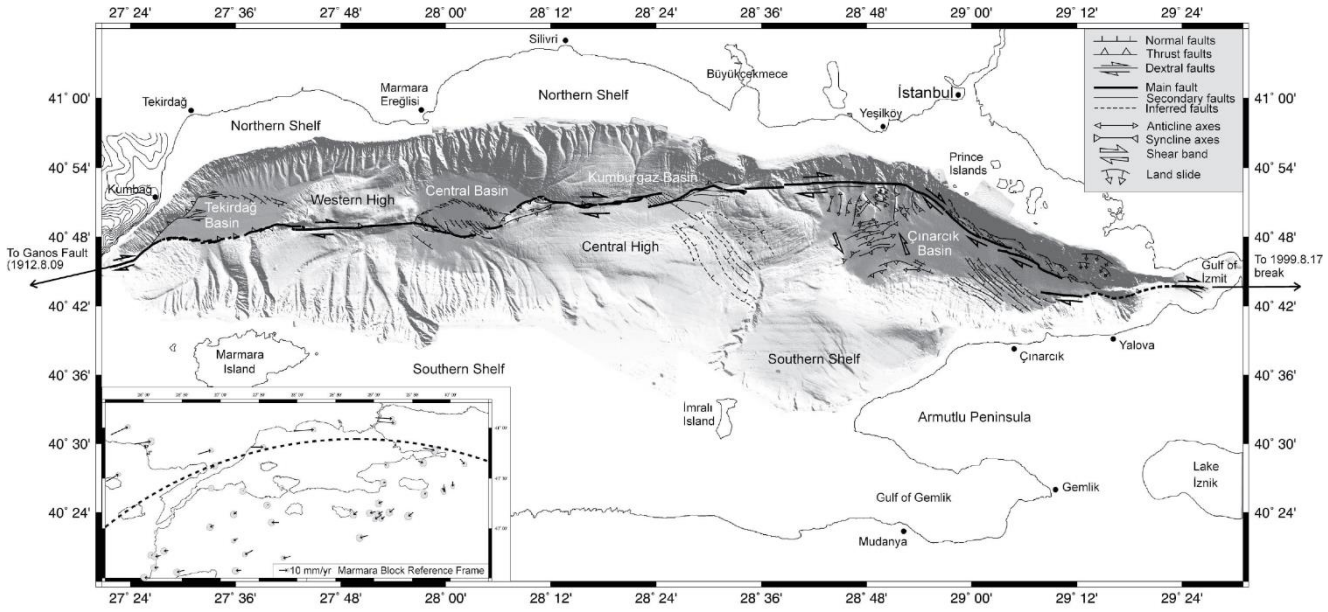

Fig. 2. Bathymetric map of the Marmara Trough with the main active structures (Le Pichon et al., 2001).
(Main active faults are shown by thick black lines. The width of the lines refers to the relative importance of the faults.)

A window bounded by 40.6 - 40.9 latitude and 27. 5 - 29.5 degrees longitude was considered for the earthquake source. Sources were located with a time interval between 0.1 degree (about 11 km) in latitude and longitude and 10 to 30 km in depth with 10 km interval depths (three layers, Fig. 3 and Fig. 4) based on point source assumption. Therefore in the simulation there were totally 252 earthquake considered in the source area. Two stations GBZ, IZT, (the nearest inland points of strong ground motion network in the region) and SKR, located in Sakarya city were investigated for the available time analysis (Fig. 2, Table 1). These stations are operated by strong ground motion network, Disaster and Emergency Management Presidency (AFAD) Turkey. It was assumed that stations are providing online waveform as earthquake early warning system.

3. Results and Discussions

I investigated the onset time differences of P-wave between Gebze (GBZ) / Izmit (IZT) and Sakarya (SKR) (Fig. 5). This shows how many seconds it takes P-wave to arrive Sakarya after passing GBZ or IZT. GBZ station is closer to source area than IZT station. Therefore time difference for GBZ is much higher than the IZT station (Fig. 5(a-b)). Hypocenteral distances are the distance between GBZ station and the earthquake point source. After 100 km, the time difference of P-wave arrivals comes to a constant interval between 17 to 18 seconds. Time variance is large for the near source earthquake (varies between 12 to 17 seconds). The results in Fig. 5(b) show the same patterns with smaller time values due to smaller relative distance between IZT and SKR station. As a result there is minimum 7.8 seconds between onsets of P-waves.

Table 1. The coordinates of investigated stations.

Station Code	Longitude	Latitude
GBZ	29.45003	40.78627
IZT	29.91721	40.76650
SKT	30.38005	40.73707

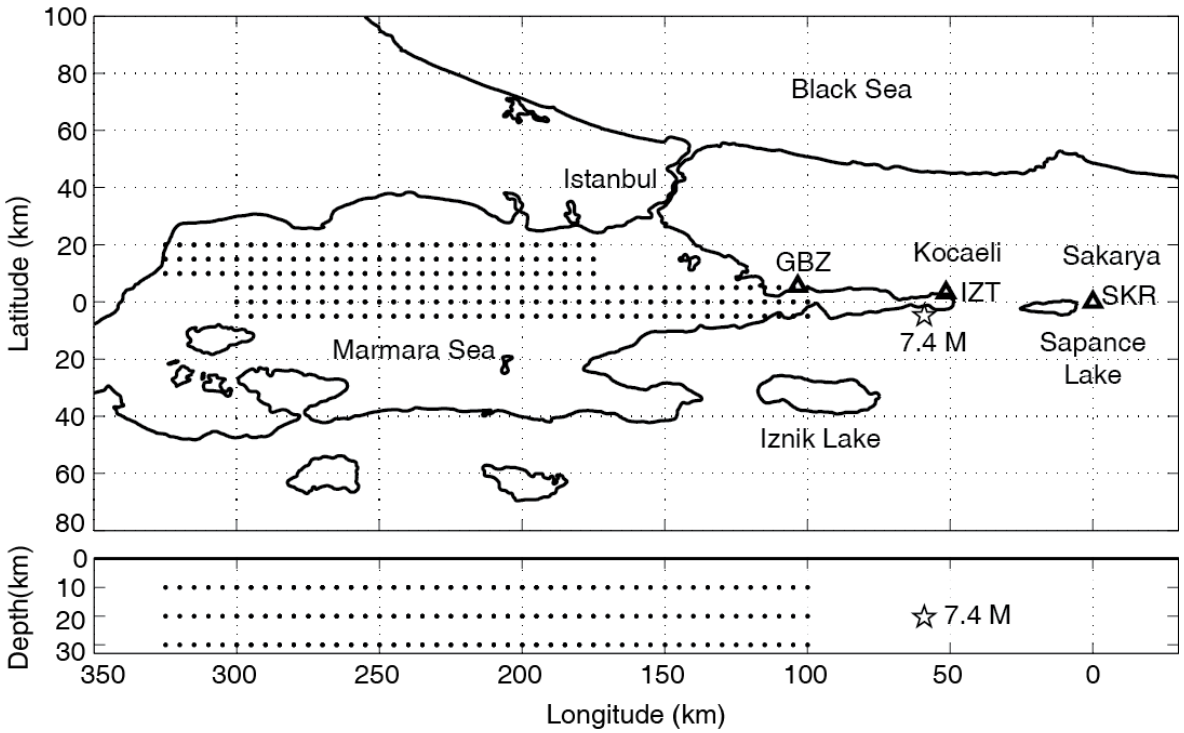

Fig. 3. The Marmara Sea and environment. Location of three stations; Sakarya (SKR), Izmit/Kocaeli (IZT), Gebze/Kocaeli (GBZ).
(Dots are the location of point source earthquakes. Star indicates the Golcuk/Izmit earthquake.)

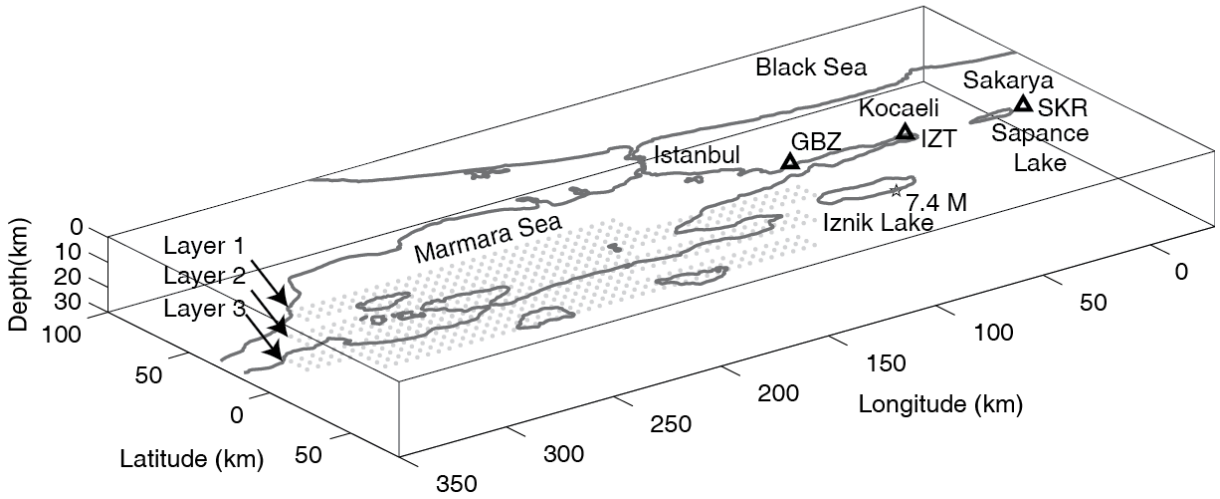

Fig. 4. The Marmara Sea and environment in 3D. Layers shows the interval of assumed point source earthquakes.

The arrivals of S-waves are calculated between GBZ/IZT and SKR stations (Fig. 6). Horizontal axis shows the hyponcentral distance from GBZ station. We observed same pattern as previous P-P wave analysis. There is minimum 18 seconds for Sakarya available after the S waves hit the GBZ station. In addition, there is minimum 12.4 seconds after detection of S-wave in Izmit to reach Sakarya city. Therefore there would be considerable warning time for Sakarya even after S wave detection in Izmit.

The available time for Sakarya according to Eq. (1) by assuming transmission and process time is zero, are shown in Fig. 7. Same as above, available times are as a function of hypocentral distance to GBZ station. The available time increase almost linearly with distance. The minimum available time is 21.9 seconds and maximum is 49.5 seconds where the average is the 37.9±7.4 seconds (Fig. 7(a)). By omitting GBZ station and assuming IZT station is the only one station, the minimum available time is 18 seconds and maximum is the 40.6 seconds with the average 29.5±6.7 seconds.

Although I dismissed the time needed to solve source parameters of an earthquake, there will be sufficient time to warn the Sakarya city. Because in existing network based earthquake early warning systems such as California ShakeAlert EEWS, 8 seconds in averages is

needed in order to find the source parameters of an earthquake (Kuyuk et al., 2014). On the other hand the EEWS of Japan gives the earthquake source information less than 6 second in averages after detection of earthquake (Kuyuk et al., 2008). Therefore even the processing and transmission times are subtracted from available times, remaining seconds are promising for a threshold based early warning systems.

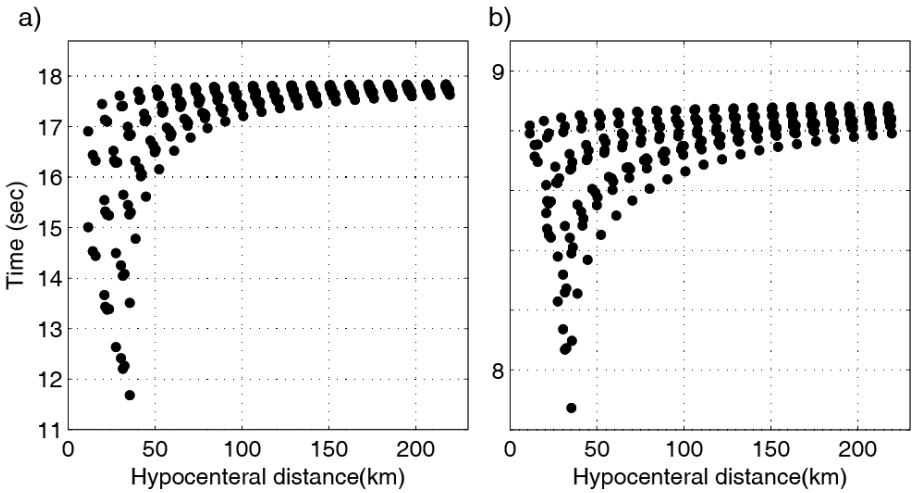

Fig. 5. The time difference of arrival of P-waves for two stations a) GBZ to SKR b) IZT to SKR.

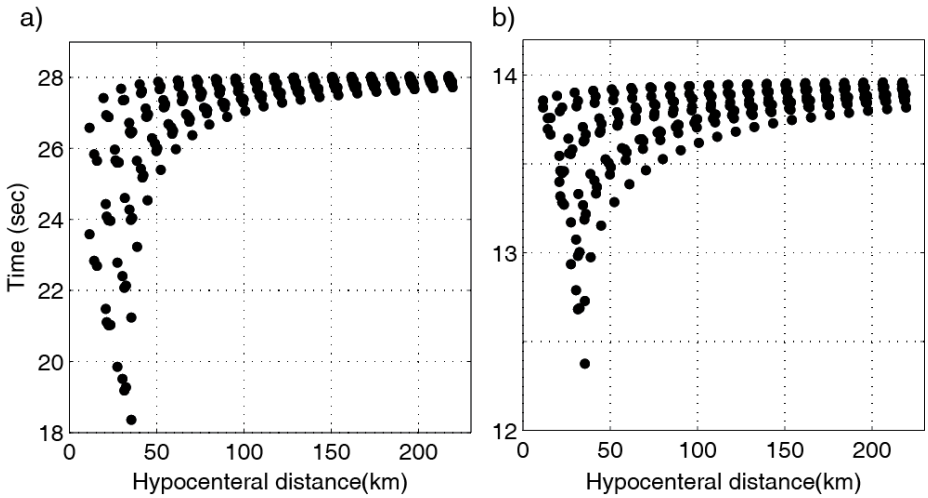

Fig. 6. The time difference of arrival of S-waves for two stations a) GBZ to SKR b) IZT to SKR.

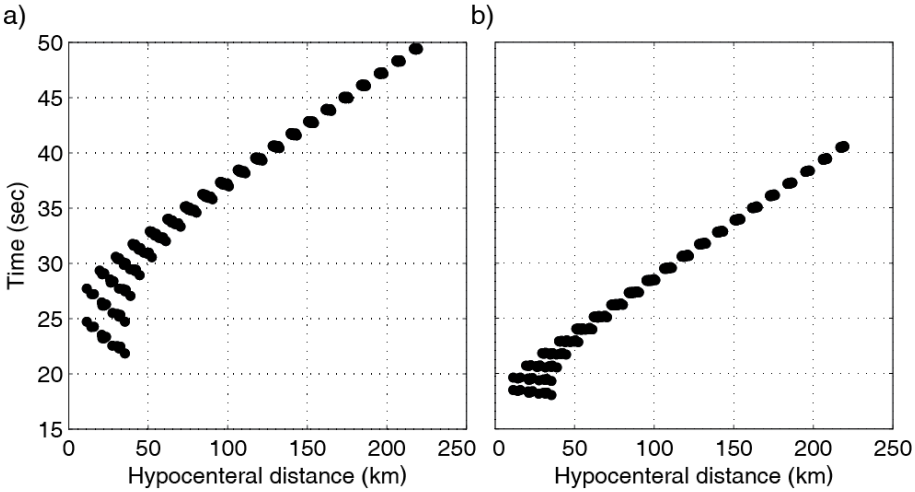

Fig. 7. The available time for Sakarya city. Time difference onset of P wave of a) GBZ b) IZT and S wave arrival to SKR stations. Hypocenteral distance are from GBZ stations.

One of the semiconductor companies in Miyagi Prefecture, Japan declared that they have a capability to stop their product line in their factory in three seconds (Kuyuk et al., 2008). Therefore for similar companies located in Sakarya city would be able to stop the production in any case of Marmara offshore earthquakes based on this study. About 30 seconds of available time would be sufficiently enough in order take some important countermeasures against expecting Marmara earthquake.

The conducted analysis in this study is fundamental research based on theoretic P and S wave velocities. The warning times might change by assuming different velocities. More detailed analysis is needed based on real recorded waveforms in order to validate theoretical results. However similar studies should be performed for other cities in earthquake prone region.

4. Conclusions

Over the earthquake history of Northwestern Turkey, Marmara region has been the site of several destructive earthquakes. It would be possible to inform individuals, government and the private companies about the warning time of next Marmara offshore earthquake if the city has an earthquake early warning system. Moreover, precautionary actions could be taken by the society and government for the next probable upcoming earthquake. Citizens living in their habitats could prepare themselves mentally and physically by real-time earthquake early warning system. Government could prepare real-time disaster prevention strategies for the city. For this purpose, the available time analysis performed for Sakarya City against approaching Marmara offshore earthquakes by using the existing seismic network geometry is presented in this study. Warning times are determined using the theoretic P- and S- wave velocities for Marmara region. Results indicate that Sakarya has about 37.9±7.4 second warning time in average before the strong shaking reach the city.

REFERENCES

Böse M, Allen R, Brown H, Gua G, Fischer M, Hauksson E, Jordan T (2014). CISN Shake Alert: An earthquake early warning demonstration system for California. *In: Wenzel F, Zschau J, editors. Early Warning for Geological Disasters.* Springer Inc., Berlin Heidelberg, Germany. 49-69.

Cua G, Heaton T (2007). The virtual seismologist (VS) method: A bayesian approach to earthquake early warning, in Seismic early warning. *In: Gasparini P, Manfredi G, Zschau J, editors. Seismic Early Warning.* Springer Inc., Berlin Heidelberg, Germany. 85-132.

Disaster & Emergency Management Authority (2010). Strong ground motion database of Turkey. Republic of Turkey Prime Ministry, Ankara, http://daphne.deprem.gov.tr.

Emre O, Duman TY, Özalp S, Elmacı H, Olgun Ş, Şaroğlu F (2013). 1/1.125.000 ölçekli Türkiye diri fay haritası. *Maden Tetkik ve Arama Genel Müdürlüğü Özel Yayınlar Serisi*, Ankara, Turkey (in Turkish).

Horiuchi S, Negishi H, Abe K, Kamimura A, Fujinawa Y (2005). An Automatic Processing System for Broadcasting Earthquake Alarms. *Bulletin of the Seismological Society of America* 95(2), 708-718.

Kalafat D, Gürbüz C, Üçer SB (1987). Batı Türkiye'de kabuk ve üst manto yapısının araştırılması. *Deprem Araştırma Bülteni*, 59, 43-64 (in Turkish).

Koçyiğit A (2000). Segmentation, kinematics and seismicity of the North Anatolian fault system in Marmara Sea region. *NATO Advanced Research Seminar*, 17-18.

Kuleli HS, Gürbüz C, Horasan G, Gülen L (1996). Seismic velocity distribution in the Aegean region. *Eos, Transactions, American Geophysical Union*, 77, 476-477.

Kuyuk HS, Motosaka M (2009). Real-time ground motion forecasting using front-site waveform data based on artificial neural network. *Journal of Disaster Research*, 4(4).

Kuyuk HS, Motosaka M (2009). Forward spectral forecasting of ground motion with the information of earthquake early warning systems for structural control. *Journal of Japan Association for Earthquake Engineering*, 9(3).

Kuyuk HS, Motosaka M (2008). Development of an integrated early warning and structural monitoring system to real time earthquake information, Part 3: Ground motion prediction using artificial neural network. *Tohoku Journal of Natural Disaster Science*, 44, 23-29.

Kuyuk HS, Motosaka M, Homma M (2008). Spectral forecasting of earthquake ground motion using regional and national earthquake early warning systems for advanced engineering application against approaching Miyagi-ken Oki earthquakes. *14th World Conference on Earthquake Engineering*, China.

Kuyuk HS, Motosaka M, Homma M (2008). Available warning time for emergency response in Sendai city, Japan against Miyagi-oki subduction earthquakes based on national and regional earthquake early warning system. *14th World Conference on Earthquake Engineering*, China.

Kuyuk HS, Motosaka M (2008). Ground motion forecasting using a hybrid earthquake early warning system based on artificial neural network: A case study for miyagi-ken Oki earthquakes. *Meeting of Architectural Institute of Japan*, Hiroshima, Japan.

Kuyuk, HS, Motosaka M, Homma M (2008). Forecasting parameters of earthquake ground motion using regional and national earthquake early warning systems with artificial neural network for Miyagi-oki subduction earthquakes. *International Conference on Earthquake Engineering and Disaster Mitigation*, Jakarta, Indonesia.

Kuyuk HS, Allen RM (2013a). A global approach to provide magnitude estimates for earthquake early warning alerts. *Geophysical Research Letters*, 40(24), 6329-6333.

Kuyuk HS, Allen RM (2013b). Optimal seismic network density for earthquake early warning: A case study from California. *Seismological Research Letters*, 84(6), 946-954.

Kuyuk HS, Allen RM, Brown H, Hellweg M, Henson I, Neuhauser D (2014). ElarmS-2: Designing a network-based earthquake early warning system for California. *Bulletin of the Seismological Society of America*, 104(1), 162-173.

Le Pichon X, Şengör AMC, Demirbağ E, Rangin C, İmren C, Armijo R, Görür N, Çağatay N, Mercier de Lepinay B, Meyer B, Saatçılar R, Tok B (2001). The active main Marmara fault. *Earth and Planetary Science Letters*, *192*(4), 595-616.

Motosaka M, Homma M, Kuyuk HS, Arrecis F (2008). Development of an integrated early warning and structural monitoring system to real time earthquake information. *AIJ Journal of Technology and Design*, 14, 28.

Okada T, Umino N, Ito Y, Matsuzawa T, Hasegawa A, Kamiyama M (2001). Source processes of 15 September 1998 M 5.0 Sendai, Northeastern Japan, earthquake and its M 3.8 foreshock by waveform inversion. *Bulletin of the Seismological Society of America*, 91(6), 1607-1618.

Zor E (2002). The Shear Wave Velocity Structure of the Eastern Marmara Region by Using Receiver Function Analysis. *Ph.D. thesis*, Boğaziçi University, Turkey.

Challenge Journal of Structural Mechanics

Minimum weight design of prestressed concrete beams by a modified grid search technique

İsmail Hakkı Çağatay *

Department of Civil Engineering, Çukurova University, 01330 Adana, Turkey

ABSTRACT

In this study, a computer program, which employs modified grid search optimization technique, has been developed for the minimum weight of prestressed concrete beams under flexure. Optimum values of prestressing force, eccentricity and cross-sectional dimensions are determined subject to constraints on the design variables and stresses. The developed computer program offers a rapid practical and interactive method for realizing optimum design of beams of general I-shaped cross-section with eight geometrical design variables. The computer program can assist a designer in producing efficient designs rapidly and easily. Two examples, one of which is available in the literature and the other is modified form of it, have been solved for minimum cross-sectional area designs and the results were found to be in good agreement.

ARTICLE INFO

Article history:
Received 8 May 2015
Accepted 23 June 2015

Keywords:
Optimum
Prestressed concrete
Flexure
Minimum weight design
Grid search

1. Introduction

Optimization is generally defined as the best condition. For prestressed concrete, the best condition can be defined as to find the minimum cross-section, minimum prestressing or minimum cost of a beam. Several analytical studies of optimum design of prestressed beams have been reported in the literature (Morris, 1978; Taylor, 1987; Cohn and MacRae, 1983; Jones, 1984; Saouma and Murad, 1984; Birkeland, 1974; Fereig, 1994; Wang, 1970; Kirsh, 1972). In these studies, linear programming methods and non-linear programming procedures such as gradient methods have been used as optimization techniques. However, the grid search optimization method, which is simple and effective for programming, has not been used for the optimization of prestressed concrete beams before.

In the present study, a modified grid search optimization method (Çağatay, 1996) has been applied to the prestressed concrete beam. The advantages of the method can be defined as: with no restriction on the number and type of constraints on the design variables and stresses.

The proposed method is applied to an example problem available in the literature and the results are in good agreement.

A computer program has been developed employing the modified grid search optimization method, which can assist a designer in producing efficient designs rapidly and easily.

2. Problem Formulation

In general, most papers on prestressed concrete beam design and optimization deal with idealized I beam section with six dimensions (Morris, 1978; Taylor, 1987; Cohn and MacRae, 1983; Jones, 1984) due to simplicity. But, here, the method has been formulated for a general I shaped cross-section with eight geometrical design variables denoted by X_1 through X_8 as shown in Fig. 1. The variables X_7 and X_8 are calculated as a function of m, which is the slope of the top and bottom flanges of the cross-section, as shown in Fig. 1.

If the m value is chosen to be zero, the cross-section of the beam turns into an idealized I-beam. Also, additional design variables X_9 and X_{10} are considered, which represent the eccentricity and the prestressing force, respectively. In the figure, Y_t and Y_b are the distances of the top and bottom fibers of the cross-section from the center of gravity of concrete section (*c.g.c.*), and h denotes the total depth of the cross-section.

* *Corresponding author*. Tel.: +90-322-3386784 ; Fax: +90-322-3386702 ; E-mail address: hcagatay@cu.edu.tr (İ. H. Çağatay)
ISSN: 2149-8024 / DOI: http://dx.doi.org/10.20528/cjsmec.2015.06.017

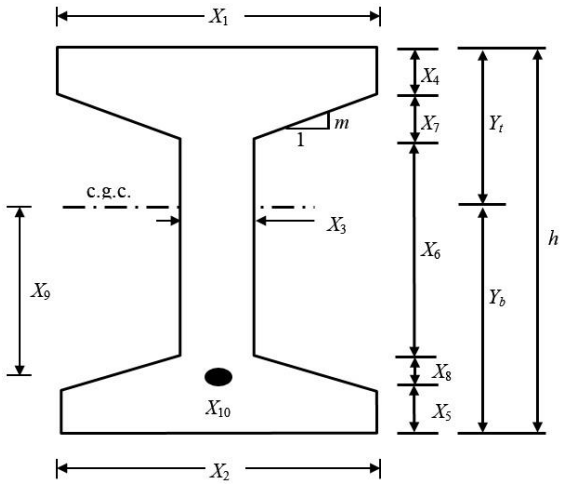

Fig. 1. Cross-section of general I-shaped PC beam.

The objective function to be minimized is denoted by $f(X)$ and the constraint functions by $g_i(X)$. The optimization problem can thus be defined as:

$$\text{Minimize} \quad f(X) = A_p \tag{1}$$

$$\text{Subject to} \quad g_i(X \leq 0) \, , \geq 0 \, , (i = 1, 2, \ldots, k) \tag{2}$$

where A_p is the cross-sectional area of prestressed concrete beam and k denotes the number of constraints. The aims of the objective function are to minimize both the cross-sectional area of prestressed concrete and find the minimum prestressing force corresponding to maximum eccentricity. To obtain the minimum prestressing force corresponding to maximum eccentricity, Magnel's graphical method has been used (Magnel, 1948).

The following constraints were considered for the optimization problem: flexural stresses, prestressing force and eccentricity, cross-sectional dimensions and ultimate moment.

2.1. Flexural stresses

There are two stages of loading to be considered. The first stage is at the transfer of prestressing force to the beam. For computing the flexural stresses at the top and bottom of the beam, following equations can be written:

$$f_{tt} = \frac{P}{A} - \frac{P\,e\,Y_t}{I} + f_{td} \, , \tag{3}$$

$$f_{tt} = \frac{P}{A} - \frac{P\,e\,Y_b}{I} - f_{bd} \, , \tag{4}$$

where f_{tt} and f_{tb} are the flexural stresses at the top and bottom of the beam and P and e are the prestressing force and the eccentricity, respectively. I and A denote the gross second moment of area and the gross area of the cross-section, respectively. f_{td} and f_{bd} are the flexural stresses at the top and bottom of the beam due to the dead load.

The second stage is at the service condition when the beam carries live loads in addition to its own weight. The following equations can be written:

$$f_{st} = \frac{P\,\alpha}{A} - \frac{P\,\alpha\,e\,Y_t}{I} + f_{td} + f_{tl} \, , \tag{5}$$

$$f_{sb} = \frac{P\alpha}{A} + \frac{P\,\alpha\,e\,Y_b}{I} - f_{bd} + f_{bl} \, , \tag{6}$$

where f_{st} and f_{sb} are the flexural stresses at the top and bottom of the beam, respectively; α is the loss factor; f_{tl} and f_{bl} are the stresses due to the live load at the top and bottom fibers, respectively.

The stresses computed by Eqs. (3-6) should not exceed the allowable stresses, which are specified in design codes. Rearranging Eqs. (3-6), and considering the allowable stresses, the following inequalities are obtained:

$$\left(-\frac{1}{A} + \frac{e\,Y_t}{I}\right)\frac{1}{(f_{IT} + f_{td})} \leq \frac{1}{P} \, , \tag{7}$$

$$\left(\frac{1}{A} + \frac{e\,Y_b}{I}\right)\frac{1}{(f_{IC} + f_{bd})} \leq \frac{1}{P} \, , \tag{8}$$

$$\left(\frac{1}{A} - \frac{e\,Y_t}{I}\right)\frac{\alpha}{(f_{FC} - f_{td} - f_{tl})} \leq \frac{1}{P} \, , \tag{9}$$

$$\left(\frac{1}{A} + \frac{e\,Y_b}{I}\right)\frac{\alpha}{(-f_{FT} + f_{bd} + f_{bl})} \geq \frac{1}{P} \, , \tag{10}$$

where f_{IT} and f_{IC} are the allowable tensile and compressive stresses in the concrete at transfer condition and f_{FC} and f_{FT} are the allowable compressive and tensile stresses in the concrete at service condition, respectively.

2.2. Prestressing force and eccentricity

For the selection of prestressing force and eccentricity, Magnel's graphical technique (Magnel, 1948) has been used and the following inequalities are obtained:

$$E_3 \geq E_1 \, , \tag{11}$$

$$E_4 \geq E_2 \, , \tag{12}$$

in which

$$E_1 = \frac{1}{(f_{IT} + f_{td})} \, , \tag{13}$$

$$E_2 = \frac{1}{(f_{IC} + f_{bd})} \, , \tag{14}$$

$$E_3 = \frac{\alpha}{(-f_{FC} + f_{td} + f_{tl})} \, , \tag{15}$$

$$E_4 = \frac{\alpha}{(-f_{FT} + f_{bd} + f_{bl})} \, . \tag{16}$$

If Eqs. (11-12) are satisfied, and then the cross-sectional area is adequate under the given loading condition. It is assumed that for maximum efficiency, the eccentricity takes its largest allowable value at mid-span (with minimum cover). Therefore,

$$e \leq Y_b - e_{cover} \, , \tag{17}$$

in which e_{cover} is the required concrete cover.

2.3. Cross-sectional dimensions

Aspect ratios of the web and flanges cannot exceed a prescribed limiting value without any conditions concerning slenderness. This limit is presently taken as 8.0.

Further constraints have also been introduced for the cross-sectional dimensions as follows:

$$(X_i)_{min} \leq X_i \leq (X_i)_{max} \quad (i = 1, 2, \dots, n)\,, \tag{18}$$

where *n* is the number of variables.

2.4. Ultimate moment

Ultimate moment design is based on the solution of the equations of equilibrium, using the equivalent rectangular stress block shown in Fig. 2. An equivalent rectangular stress block is used with ease and without loss of accuracy to calculate the compressive force and hence the flexural moment strength of the section.

Design requirement should meet the following condition:

$$\phi M_n \geq M_u\,, \tag{19}$$

where M_u is the applied factored moment at a section; ϕ is the strength reduction factor which is taken to be as 0.9.

3. Optimization Procedure

The algorithm described below was developed by Çağatay (1996) and is a modification of the one given by Walsh (1975). This modified algorithm, which follows, is going to be used in this study.

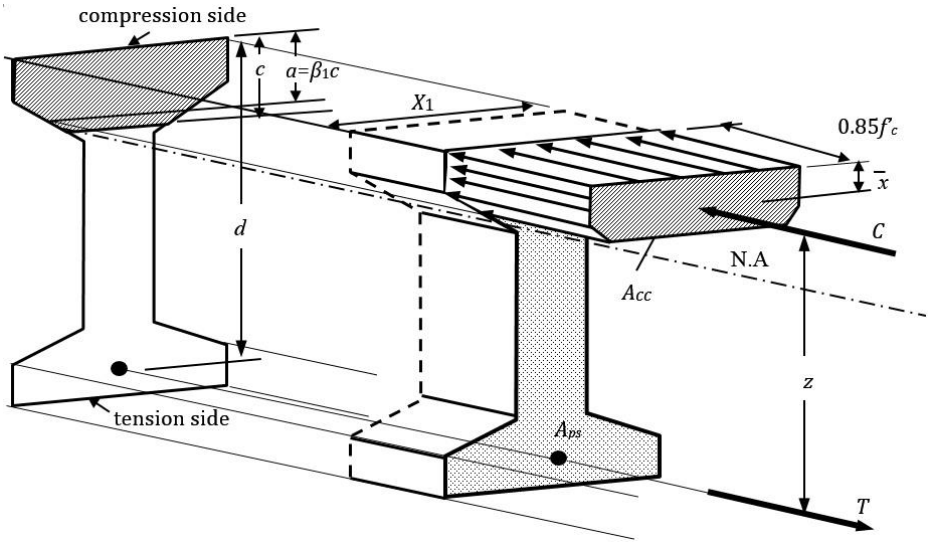

Fig. 2. Assumed stress distribution in the cross-section of the beam at ultimate limit state.

The algorithm described below was developed by Çağatay (1996) and is a modification of the one given by Walsh (1975). This modified algorithm, which follows, is going to be used in this study.

1. Start with the solution region defined by Eq. (18), in which $X_i (i = 1,2, \dots, n)$, are the design variables, $(X_i)_{min}$ and $(X_i)_{max}$ are the minimum and maximum values of the corresponding variables, respectively. Take three values for each variable in the region, two of them at the ends and the third at the midpoint. Make a search for the optimum among all possible combinations of computation points, which satisfies the constraints.
2. Reduce the solution region to half the width of the previous one. Take the range for each variable to be equal to half the range of the previous step, with two additional computation points on the two sides of the previous optimizing computation point while making sure to remain within the initial solution range.
3. Repeat step 2 until the variable set is obtained with the desired accuracy. For the accuracy criterion, different options can be used; a fixed percentage accuracy for each variable or a percentage accuracy in the least squares sense, etc. In the present study, fixed percentage accuracy criterion has been employed. That is to say, computation is continued until

$$\varepsilon_i = \frac{(X_i)_{K+1} - (X_i)_K}{(X_i)_K}\,, \tag{20}$$

$$\varepsilon_i \leq (\varepsilon_i)_{accuracy} \quad (i = 1, 2, \dots, n)\,, \tag{21}$$

where ε_i and $(\varepsilon_i)_{accuracy}$ are the limits of the respective variables.

4. Numerical Examples

4.1. Example 1

Design a simply supported beam of 16460 mm span subjected to an applied load of 23.34 kN/m. Assume the unit weight of concrete is 24 kN/m^3, allowable stresses for compression are at transfer 16.55 MPa, at service 15.51 MPa, those for tension are at transfer –1.31 MPa,

at service -2.93 MPa and loss factor is 0.85, f_c'=34 MPa, f_{pu}=1862 MPa, and e_{cover}=50 mm. For this problem, also assume that, because of clearance requirements, the overall depth of the beam, *h*, cannot exceed 914.4 mm.

This example was discussed first by Khachaturian and Gurfinkel (1969), and later by Taylor and Amirebrahimi (1987). The solutions and the comparison of the results are presented in Tables 1-2 and Table 3, respectively.

Table 1. Variables, initial values and results for Example 1.

Variables	Minimum Values (mm)	Maximum Values (mm)	Initial Values (mm)	Optimum Results (mm)
X_1	101.6	750.0	425.8	587.9
X_2	101.6	750.0	425.8	506.8
X_3	101.6	400.0	250.8	101.6
X_4	101.6	400.0	250.8	101.6
X_5	50.0	150.0	100.0	124.6
X_6	400.0	900.0	650.0	681.2

Table 2. Optimum results, the stresses at transfer and service for Example 1.

Stage	Location	Stress (MPa)	Allowable Stress (MPa)	P (kN)	E (mm)	Cross-sectional area (mm²)
Transfer	Top	-1.31	-1.31	1424.0	409.7	192103.0
	Bottom	16.16	16.55			
Service	Top	15.51	15.51			
	Bottom	-2.93	-2.93			

Table 3. Comparison of the results.

	P (kN)	E (mm)	A (mm²)
Khachaturian and Gurfinkel	1650	360.6	219999
Taylor and Amirebrahimi	1673	370.8	205160
This study	1424	409.7	192103

As seen from Table 3, the program gives the minimum cross-sectional area and the minimum prestressing force. The cross-sectional area is found 14% less than the solution of Khachaturian and Gurfinkel (1969), and 6% less than the solution given by Taylor and Amirebrahimi (1987). The overall depth of the beam is found to be 907.4 mm, which had to be less than 914.4 mm. But, Taylor and Amirebrahimi (1987) obtained this value as exceeded the aforementioned constraint.

In the present study, the prestressing force is found to be 15% less than the solution of Khachaturian and Gurfinkel (1969), and 17% less than the solution given by Taylor and Amirebrahimi (1987).

4.2. Example 2

This example has the same span and loading as Example 1, but the cross-section has a general I shape as seen in Fig. 2.

To obtain optimum solution, *m* is chosen in the range from 0 to 1.5. The optimum values are obtained when *m*=0.5. The cross-sectional area with eight dimensions is found to be 209158 mm², which is 8% more than the solution of idealized section considered in Example 1. The prestressing force is 1530 kN which is also 7% more than the value obtained for the idealized cross-section.

Table 4. Optimum results for Example 2.

X_1 (mm)	X_2 (mm)	X_3 (mm)	X_4 (mm)	X_5 (mm)	X_6 (mm)	X_7 (mm)	X_8 (mm)	P (kN)	e (mm)	Cross-sectional area (mm²)
506.8	405.5	101.6	101.6	143.1	664.6	103.3	75.9	1530	401	209158

5. Conclusions

A computer program that is capable of finding the minimum weight of a prestressed concrete beam satisfying the given constraints including flexural stresses, cover requirement, the aspect ratios for top and bottom flanges and web part of a beam and ultimate moment, based on modified grid search optimization technique, is developed and evaluated. The computer program offers a rapid, practical, and interactive method for realizing optimum design of beams of general I sections.

The program finds the optimum solution in a few iterations. Thus, a considerable saving is obtained in computational work. The program has also graphical output, which indicates Magnel diagram with feasible region, which helps in determining the prestressing force and the eccentricity values.

Two examples, one of which is available in the literature and the other is modified form of it, have been solved for minimum cross-sectional area designs and the results were found to be in good agreement.

The idealized I beam section with six dimensions gives about 10% smaller value compared with general I-shaped beam section with eight dimensions. In the case of general I section, taking 0.5 for the slope, m, yields the minimum cross-sectional area.

REFERENCES

ACI 318-95 (1995). Building Code Requirements for Reinforced and Prestressed Concrete. American Concrete Institute, Michigan, USA.

Birkeland HW (1974). How to design prestressed concrete beams of minimum cross section. *ACI Journal*, 71(12), 634-641.

Cohn MZ, MacRae J (1983). Optimization of structural concrete beams. *ASCE Journal of Structural Engineering*, 110(13), 1573-1588.

Çağatay İH (1996). Optimum Design of Prestressed Concrete Beams. *Ph.D. thesis*, Çukurova University, Adana, Turkey.

Fereig SM (1994). An application of linear programming to bridge design with standard prestressed girders. *Computers & Structures*, 50(4), 455-469.

Jones HL (1984). Minimum cost prestressed concrete beam design. *ASCE Journal of Structural Engineering*, 111(11), 2464-2478.

Khachaturian N, Gurfinkel G (1969). Prestressed Concrete. McGraw-Hill, New York.

Kirsh U (1972). Optimum design of prestressed beams. *Computers & Structures*, 2, 573-583.

Magnel G (1948). Prestressed Concrete. Concrete Publications, London.

Morris D (1978). Prestressed concrete design by linear programming. *ASCE Journal of Structural Division*, 104(ST3), 439-452.

Saouma VE, Murad RS (1984). Partially prestressed concrete beam optimization, *Journal of Structural* Engineering, 110(3), 589-604.

Taylor MA (1987). Direct design of nonprismatic prestressed beams: I. *ASCE Journal of Structural Engineering*, 113(6), 1154-1166.

Taylor MA, Amirebrahimi A (1987). Direct design of nonprismatic prestressed beams: II. *ASCE Journal of Structural Engineering*, 113(6), 1167-1184.

Walsh GR (1975). Methods of Optimization. John Wiley and Sons, London.

Wang CH (1970). Optimum design of prestressed concrete members. *ASCE Journal of Structural Division*, 96(ST7), 1525-1534.

Challenge Journal of Structural Mechanics

Reliability of concrete box culverts designed for vertical loads

Sami Oğuzhan Akbaş [a], Süleyman Bahadır Yüksel [b,*]

[a] *Department of Civil Engineering, Gazi University, 06430 Ankara, Turkey*
[b] *Department of Civil Engineering, Selçuk University, 42075 Konya, Turkey*

ABSTRACT

The design vertical loads on box culverts under embankments are commonly calculated using the soil-structure interaction factors (F_e) recommended by the American Society of Highway and Transportation Officials (AASHTO). Non-linear finite element analyses were used to update F_e given by AASHTO by considering the effects of backfill height, culvert stiffness, backfill material stiffness, backfill compaction, and the rigidity of the layer on which the culvert rests. A simplified reliability analysis was performed to determine the adequacy of safety level in AASHTO load resistance factor design (LRFD) code specifications.

ARTICLE INFO

Article history:
Received 1 May 2015
Accepted 29 June 2015

Keywords:
Soil-structure interaction
Box culverts
Reliability analysis
Finite element method

1. Introduction

Culverts are underground structures that are utilized to convey water, small vehicles, and utilities. Soil-structure interaction effects increase the complexity of stress distribution around culverts. The load that acts on the culvert may be influenced by the characteristics of the backfill and the in-situ material, the installation methodology, and the geometry and structural characteristics of the culvert itself. However, due to the large number of these structures that are being built for various purposes, a relatively simple design procedure is required for analysis and design.

Currently, the most common procedure to estimate design vertical loads on concrete box culverts is to use the soil-structure interaction factors recommended by the American Society of Highway and Transportation Officials (AASHTO). Based on the study by Akbaş and Yüksel (2007), this study examines the vertical loads on reinforced concrete box culverts under embankments using non-linear finite element analyses, considering the effects of backfill height, culvert stiffness, backfill material stiffness, backfill compaction, and the rigidity of the layer on which the culvert rests. A simplified reliability analysis is then performed to determine the adequacy of safety level for culvert design using AASHTO load resistance factor design (LRFD) code specifications.

2. AASHTO Design Methodology

According to the installation methodology, culverts can be classified as embankment or trench installations, with an embankment installation having its top projecting above the natural ground surface, and covered with an embankment. A trench installation is constructed in a narrow ditch such that its top is below the natural ground surface and then is covered with an embankment. The behavior of these two installation types are quite different. In embankment installations, the relative settlement of the soil prism directly above the structure is usually less than that of the adjacent soil prisms, the layers of soil in the central prism are subjected to an arch shape deformation, and the earth pressure on the structure is increased, which is referred to as negative arching (Vaslestad et al., 1993). On the other hand, the relative settlement of soil prism directly above the structure is more than that of the adjacent soil prisms for the trench installations. Therefore, a reverse arch shape deformation occurs in the layers of soil in the central prism, and consequently the earth pressure on the structure is reduced.

Based on their stiffnesses, culverts can further be classified as rigid or flexible. Reinforced concrete box culverts are typically considered to be rigid culverts, and are generally constructed using embankment installation methodology (Bennett et al., 2005).

* *Corresponding author*. Tel.: +90-332-2232646 ; Fax: +90-332-2410635 ; E-mail address: sbyuksel@selcuk.edu.tr (S. B. Yüksel)
ISSN: 2149-8024 / DOI: http://dx.doi.org/10.20528/cjsmec.2015.06.019

For the design vertical loadings on cast-in-place or precast concrete box culverts, the current AASHTO LRFD bridge design specifications (AASHTO, 1998) and AASHTO standard specifications for highway bridges (AASHTO, 2002) use soil-structure interaction factors based on the method developed by Spangler (1947) and on the studies initiated by Marston in 1919 at Iowa State University.

For embankment installations the soil-structure interaction factor, which is equal to the ratio of the vertical load on the culvert to the weight of the soil prism directly above it, is determined as:

$$F_e = 1 + 0.20\frac{H}{B}, \quad (1)$$

in which F_e need not be taken greater than 1.15 for installations with compacted fill at the sides, and need not be taken greater than 1.4 for uncompacted fill at the sides.

3. Finite Element Model and Its Verification

A non-linear, two-dimensional, plane strain finite element analysis of the concrete box culvert-soil system was conducted using the commercial finite element program PLAXIS. Soil behavior was represented by the Hardening-Soil model, which is an advanced model for simulating both stiff and soft soil behavior (Schanz et al., 1999). The elements representing the culvert are based on Mindlin's beam theory and they allow for beam deflection due to both bending and shearing. Each node has three degrees of freedom per node: two translational and one rotational. These elements can become plastic if a prescribed maximum bending moment or axial force is reached.

Due to symmetry, for increased computational performance, only the right-hand side of the soil-structure system was modeled. The domain was discretized using 15-noded triangular soil elements with fourth order interpolation for displacements and 5-noded beam culvert elements. A typical geometry and finite element mesh used in this study is shown in Fig. 1. There is a line of symmetry along the centre of the culvert and this was replaced by a rolling, rigid boundary. Rigid boundaries were located remote from the culvert, so as not to interfere with failure mechanisms or affect the effective stresses in the deforming zone. The boundary conditions and fixities are also shown in Fig. 1.

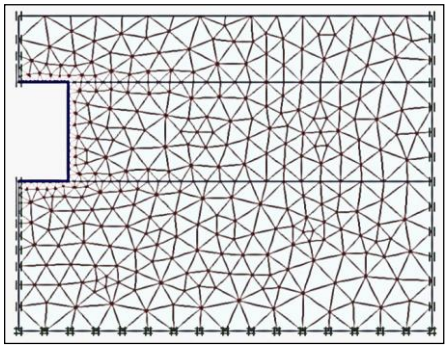

Fig. 1. Typical finite element mesh and boundary conditions.

In order to assess the validity of the soil-structure system modeling techniques and the accuracy of the finite element analysis results, a large-scale reinforced concrete box culvert tested by Dasgupta and Sengupta (1991) was reanalyzed. The details are given in Akbaş and Yüksel (2007). Both the comparison of top slab pressures as shown in Table 1, and the maximum deflections suggest that the finite element model can successfully simulate the behavior of concrete culverts.

Table 1. Undisturbed sample properties.

Pressure Cell	Dist. From Inner Face (mm)	Measured Pressure (kPa)	Calculated Pressure (kPa)
A	50	72.0	74.1
B	325	40.0	45.9
C	600	25.0	25.0

4. Updated Design Vertical Loads on Concrete Box Culverts

In this section, for various conditions, the verified finite element model was used to estimate the design vertical loads, which are calculated in terms of the soil-structure interaction factor, F_e, on concrete box culverts. The change in the vertical design load with increasing fill height expressed as the dimensionless H/B, is shown in Fig. 2, along with the soil-structure interaction factors recommended by AASHTO. Note that for each case, the soil structure interaction factor was obtained by fitting a parabolic regression equation to the shear force distribution of the top slab, and then by differentiating it to obtain the equivalent vertical load. The r^2 value was obtained to be bigger than 0.97 in all cases.

The stiffness, i.e., the thickness of the culvert was varied such that the maximum deflections obtained at the top slab are about 1/300 of the span. For reinforced concrete beam elements, the deflections are generally limited to values ranging from 1/1000 to 1/300 of the span, depending on the type and importance of the structure. Since structural integrity is the main issue for culverts, for this study, a limiting deflection of 1/300 of the span length was targeted in the analyses.

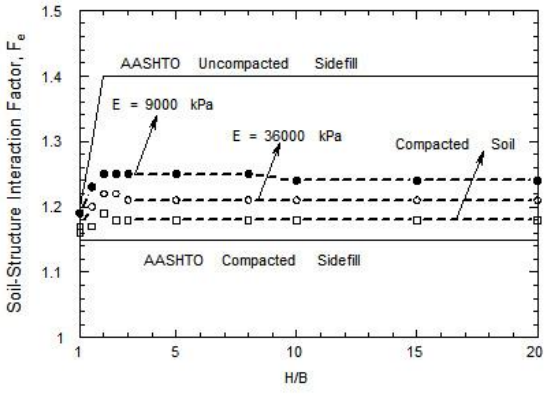

Fig. 2. Effect of soil stiffness and compaction on F_e.

The initial analyses were performed with the soil conditions specified in Dasgupta and Sengupta (1991), where the internal friction angle (ϕ') was 30°, and the modulus (E) was 9000 kPa. For these conditions, as can be seen from Fig. 2, F_e can be specified as a constant 1.25 for H/B values greater than 2. To determine the effect of soil stiffness on the vertical design load, the analyses were repeated with a much stiffer soil, with ϕ'=44°, and E=36000 kPa, respectively. It can be stated that these two soils span the usual range of conditions that can be encountered in practice. The results are also shown in Fig. 2. It can be seen that the effect of soil stiffness is minimal, and can be neglected for all practical purposes.

The effect of compaction is also investigated. Compaction not only increases the density of the soil but it also permanently increases the ratio of the horizontal to vertical pressures. Thus, it produces an effect similar to that of overconsolidation. Sherif et al. (1984) presented data for the effect of compaction on the properties of Ottawa silica sand with ϕ'=32°, and horizontal to vertical stress ratio K_o=0.466. The K_o value becomes 0.69 for a compaction effort which increases ϕ' to 38°. Using the fact that the internal friction angle is not an effective parameter for F_e, and assuming a similar increase in K_o value for the soil specified in Dasgupta and Sengupta (1991), the analyses were repeated for the compacted soil. The results are shown in Fig. 2. It can be seen that, although not by much, the effect of compaction is to reduce F_e. However, since it is difficult to quantify the effect of compaction, it is not recommended to use the reduced F_e, except for cases where compaction effort is rigorously measured. It can also be seen that the F_e values recommended by AASHTO for compacted side fills are unconservative even for compacted soil.

Although a rare occasion, a solid rock layer can be encountered immediately under the concrete box culvert. AASHTO (2002) stipulates that a special soil-structure analysis is required for "unyielding" foundations. In this section F_e values are estimated for a concrete box culvert underlain by a rigid rock layer of modulus equal to that of concrete. The results are shown in Fig. 3. It can be seen that F_e values are much higher for culverts with unyielding or "rigid" bases than those with yielding or "non-rigid" bases. Also, for culverts with unyielding bases, soil-structure interaction factors increase as the backfill heights increase. The results for culverts with unyielding bases are comparable to those obtained by Kim and Yoo (2005).

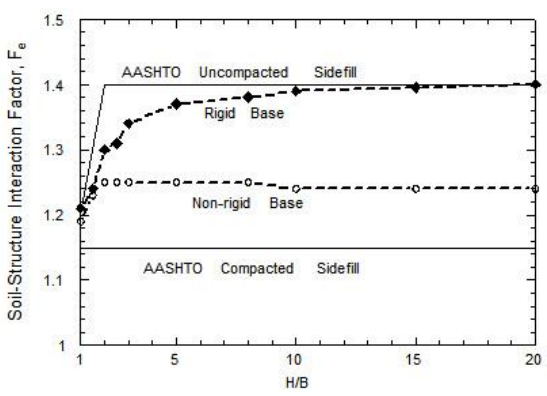

Fig. 3. Effect of rigid base on F_e.

Accordingly, F_e given by AASHTO were slightly modified as follows for culverts on a yielding base:

$$F_e = 1 + 0.20\frac{H}{B}, \tag{2}$$

in which F_e need not be taken greater than 1.18 for installations with compacted fill at the sides, and need not be taken greater than 1.25 for uncompacted fill at the sides. Also soil-structure interaction factors for culverts on unyielding bases are introduced:

$$F_e = 1.242 + \left(\frac{H}{B}\right)^{0.047}. \tag{3}$$

5. Inherent Reliability in the AASHTO LRFD Code

The safety levels in concrete box culverts designed by AASHTO LRFD code are estimated by a simplified reliability analysis. Assuming that all random variables are log-normally distributed, the reliability index (β) can be calculated as:

$$\beta = \frac{\overline{\ln R} - \overline{\ln Q}}{COV_R^2 + COV_{RQ}^2}, \tag{4}$$

in which R=resistance; Q=load; COV=coefficient of variation; and an overbar indicates a mean value. The resistance is assumed to follow the same statistics as the moment of a reinforced concrete T-beam with a bias of 1.14, and a COV of 13% (Nowak, 1995). The load is composed of two components: the soil unit weight (γ), and F_e. The COV value for soil unit weight is given to be between 3% and 20% with a mean value of 9% by Phoon and Kulhawy (1999). γ can be assumed to have a bias of 1.00 (Duncan, 2000). Assuming that the results obtained by FEM are perfectly accurate, the bias for F_e can be calculated as the ratio of equations 2 or 3 to the value obtained by AASHTO procedure.

In LRFD, a load factor of 1.3 is used for the dead load, and a resistance reduction factor of 0.9 is used for flexure. These should also be incorporated into the calculation of β. Note that a target reliability index of 3.5 was chosen for the development of the AASHTO LRFD code (Nowak, 1995).

The obtained reliability indices (β) as a function of H/B are shown in Fig. 4 for culverts on yielding and unyielding bases designed against vertical loads using AASHTO procedure. For culverts on yielding bases, inherent design reliability is higher than the target reliability except for very low values of H/B. The lowest β obtained for these culverts are about 3.1. For culverts on unyielding bases inherent design reliability is lower than the target reliability for most values of H/B, with a minimum value of about 2.9.

Although for some values of H/B, AASHTO procedure results in lower reliability index values than the specified target reliability index of 3.5, the safety level can be considered to be adequate. A lower reliability index can be justified for culverts (Bennett et al., 2005). For most cases, failure of a culvert does not directly result in a life-

safety problem although it might create serious economic consequences. Even for more important structures such as certain bridge beams in service, Nowak (1995) reported reliability indices as low as 2.0. Therefore the estimated β values above, with a minimum value of about 2.9 may be high enough.

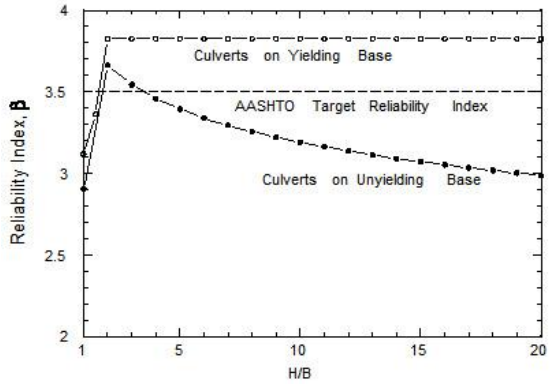

Fig. 4. Reliability indices for culverts designed by AASHTO procedure.

Note that, in addition, if the load factor is increased 5%, following the AASHTO LRFD bridge design specification (AASHTO, 1998), where it is required that the buried structures be considered as nonredundant under earth fill, the minimum value of estimated β increases to 3.2. These facts combined with the general successful behavior of culverts in practice indicate that the current methodology results in designs with high enough safety levels.

6. Conclusions

Non-linear finite element analyses were used to update the soil-structure interaction factors (F_e) for culverts on yielding and unyielding bases. The effects of backfill height, culvert stiffness, backfill material stiffness, and backfill compaction were considered. The results were then used to estimate the safety levels in concrete box culverts designed by the AASHTO LRFD code by a simplified reliability analysis. Although the obtained reliability index values for some cases are less than the target reliability index value of 3.5, it can be stated that, in general, the safety levels inherent in the culverts designed by the AASHTO code are adequate.

References

AASHTO LRFD (1998). Bridge Design Specifications (2nd edition). American Association of State Highway and Transportation Official, Washington, DC.

AASHTO LRFD (1998). Standard Specifications for Highway Bridges (17th edition). American Association of State Highway and Transportation Official, Washington, DC.

Akbaş SO, Yüksel SB (2007). Finite element analysis for the estimation of vertical design loads on reinforced concrete box culverts. *International Symposium on Advances in Earthquake and Structural Engineering*. Suleyman Demirel University, Isparta, 142-152.

Bennett RM, Wood SM, Drumm EC, Rainwater NR (2005). Vertical loads on concrete box culverts under high embankments. *Journal of Bridge Engineering*, 10(6), 643-649.

Dasgupta A, Sengupta B (1991). Large-scale model test on square box culvert backfilled with sand. *Journal of the Geotechnical Engineering Division*, 117 (1), 156-161.

Duncan JM (2000). Factors of safety and reliability in geotechnical engineering. *Journal of Geotechnical and Geoenvironmental Engineering*, 126(4), 307-316.

Kim K, Yoo CY (2005). Design loading on deeply buried box culverts. *Journal of Geotechnical and Geoenvironmental Engineering*, 131(1), 20-27.

Nowak AS (1995). Calibration of LRFD bridge code. *Journal of Structural Engineering*, 121(8), 1245-1251.

Phoon KK, Kulhawy FH (1999). Characterization of geotechnical variability. *Canadian Geotechnical Journal*, 36, 612-624.

Schanz T, Vermeer PA, Bonnier PG (1999). Formulation and verification of the Hardening-Soil model. Beyond 2000 in Computational Geotechnics, Balkema, Rotterdam.

Spangler MG (1947). Underground conduits-An appraisal of modern research. *Proceeding American Society Civil Engineering*, 73, 855-884.

Vaslestad J, Johansen TH, Holm W (1993). Load reduction on rigid culverts beneath high fills: Long-term behavior. Transportation Research Record, No. 1415, 58-68.

Challenge Journal of Structural Mechanics

Defining parameters for concrete damage plasticity model

Yusuf Sümer *, Muharrem Aktaş

Department of Civil Engineering, Sakarya University, 54187 Sakarya, Turkey

ABSTRACT

Behavior of reinforced concrete beam cannot be captured by elastic damage models or elastic-plastic constitutive laws only. When these two models coupled, load deflection behavior of reinforced concrete can be observed through numerical modeling. Thus, using concrete damage plasticity approach in finite element modeling can lead researches for sufficient numerical results when compared to experimental tests. In order to determine the material damage model of concrete, some laboratory tests are required. This paper offers an equation for damage parameter to capture damage behavior. In addition, modeling strategies are developed by checking the model sensitivity against mesh density, dilation angle and fracture energy of concrete. Finite element models are verified by three different experimental tests. In this study ABAQUS finite element software is employed to model reinforced concrete beam with concrete damage plasticity approach. This study shows that difference between the results from numerical models and experimental tests are in acceptable range.

ARTICLE INFO

Article history:
Received 14 May 2015
Accepted 11 July 2015

Keywords:
Finite element method
Reinforced concrete beam
Plastic damage model
Failure mechanisms

1. Introduction

Constitutive behavior of concrete is very difficult to capture by using elastic damage models or elastic plastic laws. In elastic damage model irreversible strains cannot be captured. It can be seen in Fig. 1(b) that a zero stress corresponds to a zero strain which makes damage value to be overestimated. On the other hand when elastic plastic relation is adopted the strain will be overestimated since the unloading curve will follow the elastic slope (Fig. 1(c)). Concrete Damage Plasticity (CDP) model which combines these two approaches can capture the constitutive behavior of experimental unloading (Fig. 1(a)) (Jason et al., 2004).

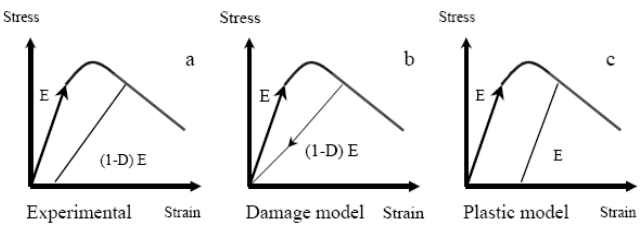

Fig. 1. Elastic plastic damage law (Jason et al., 2004).

In this model two main failure mechanisms are assumed: tensile cracking and compressive crushing of the concrete. The evolution of the yield surface is controlled by tensile and compressive equivalent plastic strains. In the following sections main assumptions about this model will be discussed in detail. In this study, developing a finite element model along with required parameters is discussed. ABAQUS nonlinear finite element commercial software package is employed. All the modeling parameters are validated by experimental results.

2. Material Constitutive Behaviors

Numerical models for the constituent material properties are described in this section.

2.1. Concrete model

CDP is one of the possible constitutive models to predict the constitutive behavior of concrete. It describes the constitutive behavior of concrete by introducing scalar damage variables. Tensile and compressive response of concrete can be characterized by CDP in Fig. 2.

* *Corresponding author*. Tel.: +90-264-2696908 ; Fax: +90-264-2956424 ; E-mail address: ysumer@sakarya.edu.tr (Y. Sümer)
ISSN: 2149-8024 / DOI: http://dx.doi.org/10.20528/cjsmec.2015.07.023

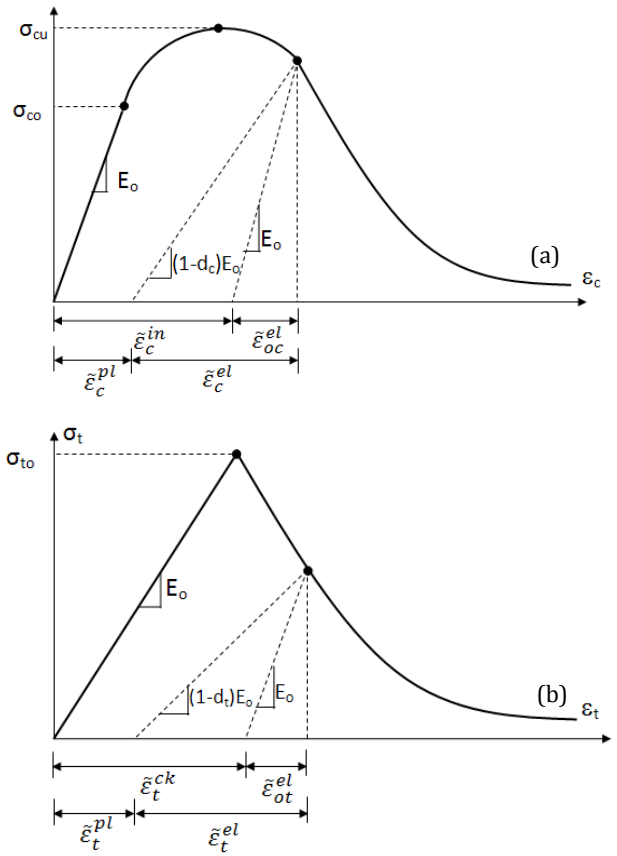

Fig. 2. Behavior of concrete under axial compressive (a) and tension(b) strength (Abaqus User Manual, 2008).

As shown in Fig. 2, the unloaded response of concrete specimen seems to be weakened because the elastic stiffness of the material appears to be damaged or degraded. The degradation of the elastic stiffness on the strain softening branch of the stress-strain curve is characterized by two damage variables, d_t and d_c, which can take values from zero to one. Zero represents the undamaged material where one represents total loss of strength (Abaqus User Manual, 2008). E_0 is the initial (undamaged) elastic stiffness of the material and $\varepsilon_c^{\sim pl}$, $\varepsilon_t^{\sim pl}$, $\varepsilon_c^{\sim in}$, $\varepsilon_t^{\sim in}$ are compressive plastic strain, tensile plastic strain, compressive inelastic strain and tensile inelastic strain respectively. The stress-strain relations under uniaxial tension and compression are taken into account in Eq. (1) and Eq. (2).

$$\sigma_t = (1 - d_t) \cdot E_0 \cdot (\varepsilon_t - \varepsilon_t^{\sim pl}), \quad (1)$$

$$\sigma_c = (1 - d_c) \cdot E_0 \cdot (\varepsilon_c - \varepsilon_c^{\sim pl}). \quad (2)$$

Interface behavior between rebar and concrete is modeled by implementing tension stiffening in the concrete modeling to simulate load transfer across the cracks through the rebar. Tension stiffening also allows to model strain- softening behavior for cracked concrete. Thus it is necessary to define Tension stiffening in CDP model. ABAQUS allows us to specify Tension Stiffening by post failure stress-strain relation or by applying a fracture energy cracking criterion (Abaqus User Manual, 2008).

There is a mesh sensitivity problem when cracking failure in not distributed evenly. This phenomenon exists when there is no reinforcement in significant regions of the model. To overcome this unreasonable mesh sensitivity problem Hillerborg's (1976) fracture energy approach can be used instead of post failure stress-strain relation (Hillerborg et al., 1976). In this approach; the amount of energy (G_F) which is required to open a unit area of crack is assumed as a material property. Thus; concrete's brittle behavior is defined by stress-displacement response rather than a stress-strain response. Specifying the post failure stress versus corresponding cracking displacement is enough to describe this approach as shown in Fig. 3(a-b) (Abaqus User Manual, 2008).

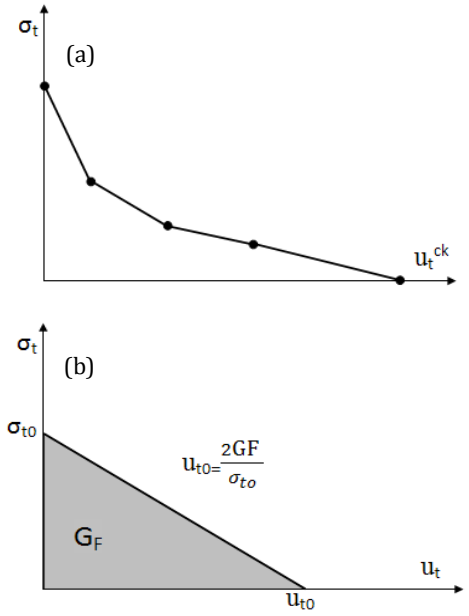

Fig. 3. Post failure stress-strain relation with fracture energy approach (Abaqus User Manual, 2008).

As an alternative, G_F can be implemented directly as a material property. However in this case, a linear loss of strength after cracking is assumed (Fig. 3(b)). From CDP perspective, ABAQUS automatically calculates both plastic displacement values using the Eq. (3) and Eq. (4).

$$u_t^{pl} = u_t^{ck} - \frac{d_t}{(1-d_t)} \frac{\sigma_t l_0}{E_0}, \quad (3)$$

$$\varepsilon_c^{\sim pl} = \varepsilon_c^{\sim in} - \frac{d_c}{(1-d_c)} \frac{\sigma_c}{E_0}. \quad (4)$$

From these equations "effective" tensile and compressive cohesion stresses ($\bar{\sigma}_t, \bar{\sigma}_c$) can be defined as:

$$\bar{\sigma}_t = \frac{\sigma_t}{(1-d_t)} = E_0(u_t - u_t^{pl}), \quad (5)$$

$$\bar{\sigma}_c = \frac{\sigma_c}{(1-d_c)} = E_0(\varepsilon_c - \varepsilon_c^{\sim pl}). \quad (6)$$

The effective cohesion stresses determines the size of the yield (or failure) surface (see Fig. 4). In Abaqus the parameters required to define the yield surface consists

of four constitutive parameters. The Poisson's ratio controls the volume changes of concrete for stresses below the critical value which is the onset of inelastic behavior. Once the critical stress value is reached concrete exhibits an increase in plastic volume under pressure (Chen, 1982). This behavior is taken into account by defining a parameter called the angle of dilation. In CDP model ψ is the dilation angle measured in the p-q plane at high confining pressure and in this study it is determined with sensitivity analysis. ϵ is an eccentricity of the plastic potential surface with default value of 0.1. The ratio of initial biaxial compressive yield stress to initial uniaxial compressive yield stress, σ_{b0}/σ_{c0}, with default value of 1.16. Finally K_c is the ratio of the second stress invariant on the tensile meridian to compressive meridian at initial yield with default value of 2/3 (Abaqus User Manual, 2008). The parameter K_c should be defined based on the full triaxial tests of concrete, moreover biaxial laboratory test is necessary to define the value of σ_{b0}/σ_{c0}. This paper does not discuss the identification procedure for parameters ϵ, σ_{b0}/σ_{c0}, and K_c because tests that are going to be verified in this study do not have such information. Thus, default values are accepted in this study.

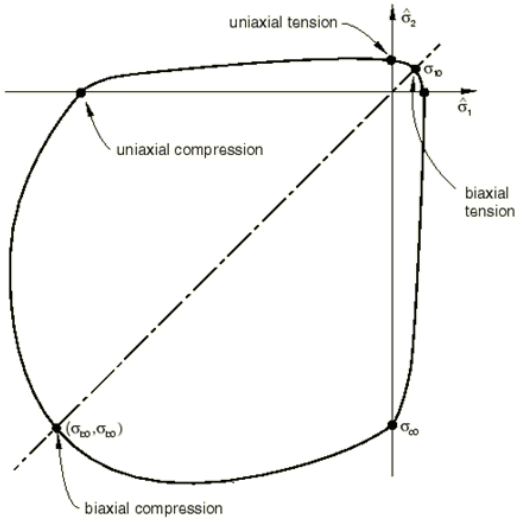

Fig. 4. Biaxial yield surface in CDP Model (Abaqus User Manual, 2008).

2.1.1. Uniaxial tension and compression stress behavior of test model

Since the compression and tension stress behavior of the experimental test specimens are not reported these relations are created by using mathematical models from literature. The compressive behavior of concrete is obtained by employing Hognestad probala along with linear descending branch. However the crushing of concrete is affected by the closed stirrups and some modifications are made for concrete in compression according to CEB-FIP MC90 (Fig. 5(a)) (CEB-FIB, 1993). Equation of the parabola is shown in Eq. (7) where σ is the compressive stress, f_{cu} is ultimate compressive stress, ε_c^* is the peak compressive strain, E is the elastic modulus and f_c^* is the modified compressive strength. Details of this model can be found in Arduini et al., 1997.

$$\sigma = f_c^* \left(\frac{2\varepsilon}{\varepsilon} - \left[\frac{\varepsilon}{\varepsilon_c^*} \right]^2 \right). \quad (7)$$

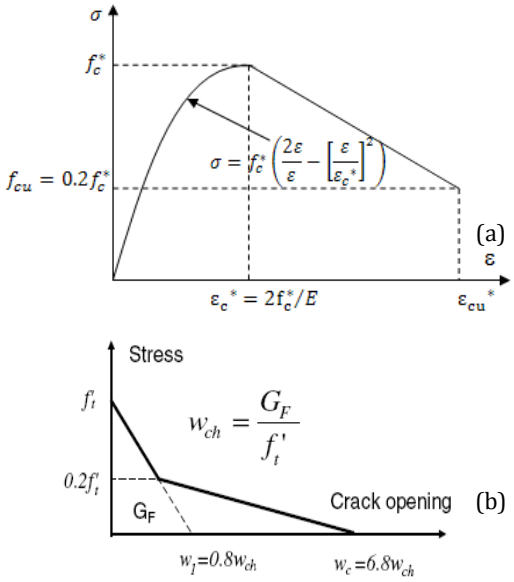

Fig. 5. Stress-strain behavior of concrete under uniaxial compression and tension a) Hognestad concrete compressive behavior b) Bilinear tensile behavior.

For tensile behavior of concrete, bilinear model is adopted as plotted in Fig. 5(b) (Coronado and Lopez, 2006). Crack opening (w_c) is calculated as a ratio of the total external energy supply (G_F) per unit area required to create, propagate and fully break a Mode I crack in concrete. However; Mode I tensile fracture energy of concrete is defined as a function of the concrete compressive strength, f_c^*, in CEB-FIP MC90 (CEB-FIB, 1993) as shown in Eq. (8). In this equation G_{fo} is a coefficient related to the maximum aggregate size (d_{max}). Several values are given in Table 1.

$$G_F = G_{fo} \left(\frac{f_c^*}{10} \right)^{0.7}. \quad (8)$$

Table 1. Aggregate size-based fracture coefficients (Rots, 1988).

Maximum aggregate size d_{max} (mm)	Coefficient G_{fo} (J/m²)
8	25
16	30
32	58

Thus, uniaxial tension and compression stress behavior are defined by using above mathematical models. These mathematical models are not enough to define CDP model. As mentioned above damage parameters are required to specify the CDP model. But these damage parameters are not reported for the experiments that are going to be verified in this study. Most of the reinforced concrete flexural test reports in the literature are also

missing this information. Because to define these damage parameters, some laboratory tests in material level should be done in advance. In this study damage parameter for concrete compressive behavior is obtained from a verification problem given in ABAQUS verification manual. By applying curve fitting method to this example a third degree polynomial curve as in Eq. (9) is obtained for this corresponding damage parameter (Fig. 6(a)). Then the very same equation is applied to get the damage parameter for the test cases that are going to be verified in this study. Also tension damage parameter is obtained by following the same behavior of example material given in ABAQUS verification manual (Fig. 6(b)).

$$y = 2E + 0.6x^3 - 41740x^2 + 324.x + 0.0052\,. \qquad (9)$$

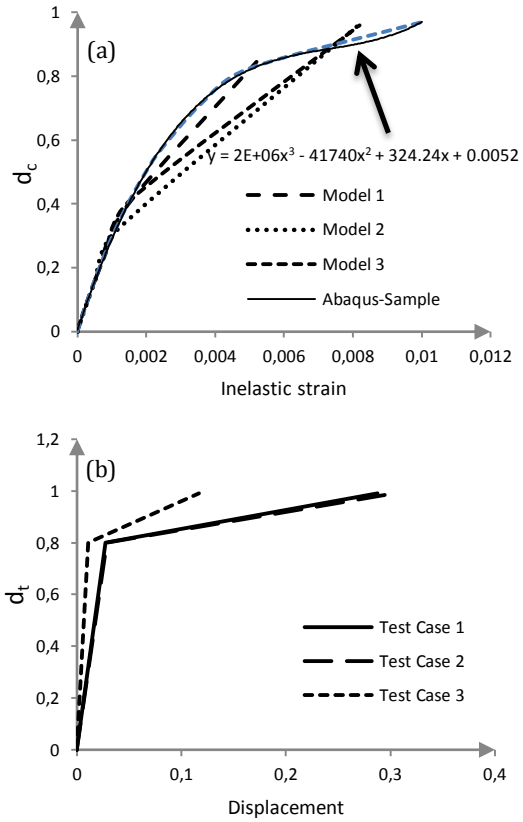

Fig. 6. Compression and tension damage parameters used in the models a) Compression damage parameter b) Tension damage parameter.

2.2. Uniaxial tension behavior of steel

The stress–strain curve of the reinforcing bar is assumed to be elastic perfectly plastic as shown in Fig. 7. In this model material yields under constant load. The parameters needed to specify this behavior are the modulus of elasticity (E_s), poisson ratio (υ) and yield stress (f_y).

3. Verification Test Group

Developing the finite element model strategies for reinforced concrete beam is verified by the experiment studies. A total of 3 beams with different mechanical properties from different researchers, were selected for verification purpose. All the beams are tested under four point load. Test layout and material properties for each experiment are given in Figure 8 and Table 2. All the details of Test Case 1, Test Case 2, and Test Case 3 can be found in Arduini et al. (1997), Benjeddou et al. (2007) and Sharif et al. (1994) respectively.

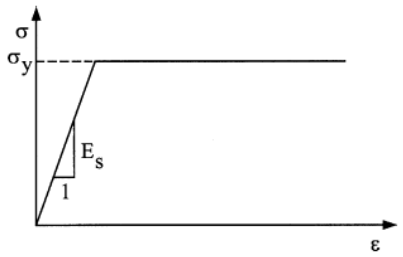

Fig. 7. Elastic perfectly plastic model for steel reinforcing bars.

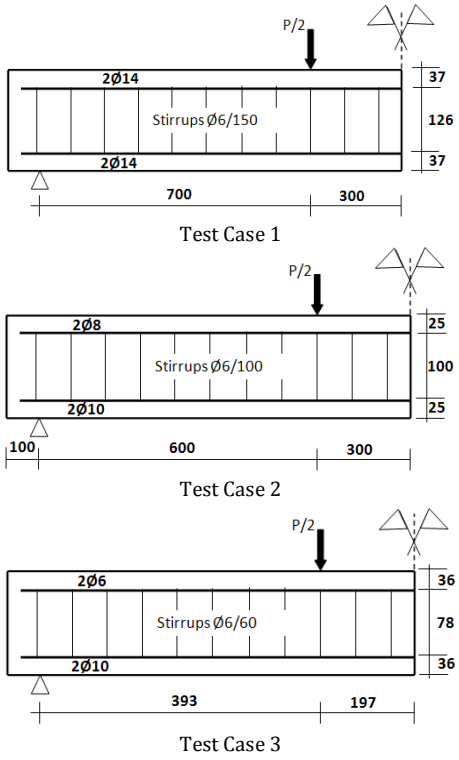

Fig. 8. Layout of test beam (dimensions are mm).

4. Finite Element Modeling

The non-linear finite element software package, ABAQUS, is employed for numerical analysis. Since there is no computational expense all the beams are modeled with full geometry in 2 dimensions (Fig. 9). Steel bars are embedded in concrete with the same degrees of freedom which also means that there is a perfect bond between concrete and steel. The advantage of the embedded model is that it allows independent choice of the concrete mesh. Concrete is modeled by using four-noded plain strain element with reduced integration formulation. Since first order elements use linear interpolation to obtain nodal displacements, the edges of these elements are unable to curve under bending resulting in

shear rather than bending deformation. This phenomenon is known as shear locking (Abaqus User Manual, 2008). To overcome this problem element with reduced integration formula is employed. All the beams are loaded by displacement control in the vertical direction. Finite element members and typical finite element mesh geometry employed in this study can be seen in Table 3 and Fig. 9.

Table 2. Material properties of test beams.

Test Case	Beam Ref. No	Width, Height, Shear span (mm)	E (GPa)	υ (-)	f_c' (MPa)	f_y (Rebar) (MPa)	f_t (MPa)	d_{max} (mm)
1	A1	200-200-2000	25	0.2	33	400	2.6	-
2	CB1	120-150-1800	30	-	21	400	1.8	16
3	P1	150-150-1180	27	-	37.7	450	-	-

Table 3. Finite element types.

Material	Description	Code	Additional information
Concrete	Four-noded plain strain	CPE4R	Reduced integration
Steel	Two-noded truss	T2D2	Embedded

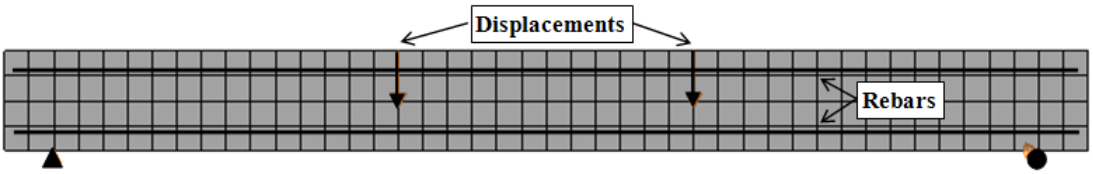

Fig. 9. Typical finite element mesh of numerical models.

5. Results and Discussions

5.1. Test Case 1 (Arduini et al., 1997)

It is clear that, the finite element simulation is very capable of capturing the experimentally observed loading trends and magnitudes for the entire loading range. For this test case, models with finer mesh captures the test result better than the models with course mesh (Fig. 10(a)). The best result is obtained with 50 mm mesh. The value for dilation angle for reinforced concrete in literature is given as 30° (Lubliner et al., 1989). Based on this information angle of dilation is varied to see the sensitivity of the results against it. Plots show that the results are not varying dramatically as the dilation angle changes (Fig. 10(b)). The best result is observed at 37°. As discussed before G_F depends on the diameter of aggregate (Eq. (8)). Since the aggregate diameter is not reported in test report this value is also changed to see how it affects the results. With the best results obtained from both mesh sensitivity and the dilation angle analysis, G_F is calculated for different aggregate diameter and result are plotted in Fig. 10(c).

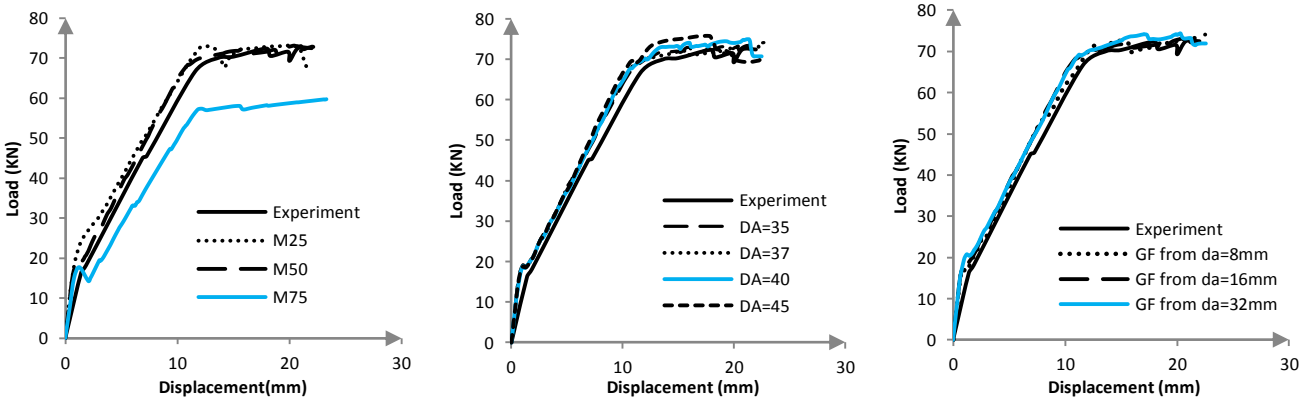

a) Mesh sensitivity b) Dilation angle sensitivity c) Fracture energy sensitivity

Fig. 10. Numerical results for Test Case 1.

5.2. Test Case 2 (Benjeddou et al., 2007)

Similar results are also observed in this test case. However; models with finer mesh has more rigid behavior than models with course mesh. But still the difference is in the acceptable range. Also 50 mm mesh gives the best results as in Test Case 1 (Fig. 11(a)). Since it is found that the models are not dilation angle sensitive, in this model values for dilation angles are changed into 30° and 50° to seek for further different values. But still it is found that the behavior can be captured within the range of the dilation angle value reported in the literature (Fig. 11(b)). Also it is clear from this test case that modeling is not very sensitive to G_F value (Fig. 11(c)).

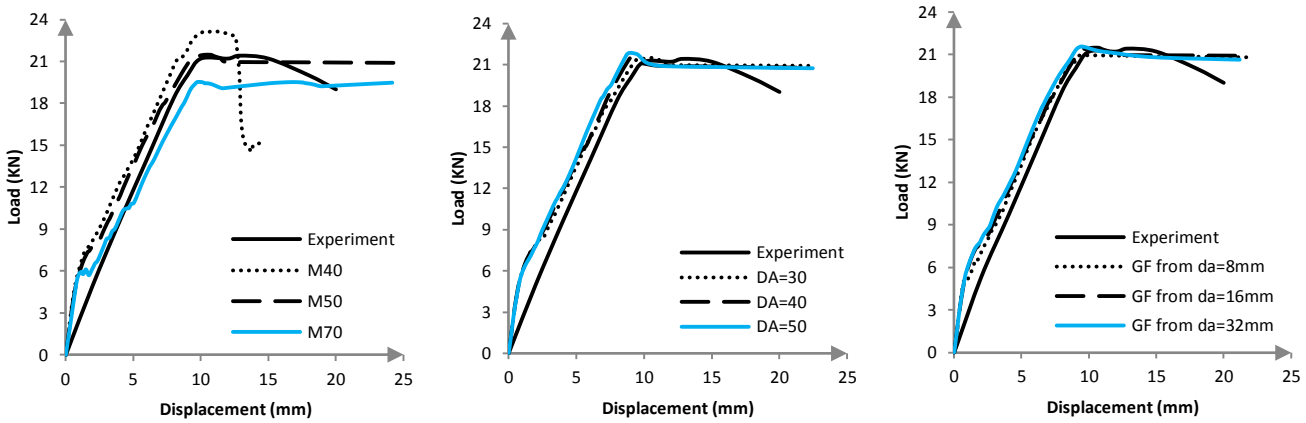

a) Mesh sensitivity b) Dilation angle sensitivity c) Fracture energy sensitivity

Fig. 11. Numerical results for Test Case 2.

5.3. Test Case 3 (Sharif et al., 1994)

This test case gives different results from other test cases. In this model some of the material properties are not reported in the test report. For example; f_t value is not reported in the test report. f_t value is calculated according to ACI (ACI 318, 1999). Unreported critical values such as elastic modulus, f_c and f_t change the results dramatically. But still the finite element simulation is capable of capturing the loading trends. In this case mesh with 25 mm captures the results of the experiment (Fig. 12(a)). But mesh with 50 mm model gives unrealistic results. Authors think that this is much related to the unreported diameter value of aggregate. Because in this case, the results are also very sensitive to G_F unlike other cases (Fig. 12(c)). The mesh should be selected with a dimension that should include the continuum properties of the material. Dilation angle of 30° captures the best results in this test case (Fig. 12(b)).

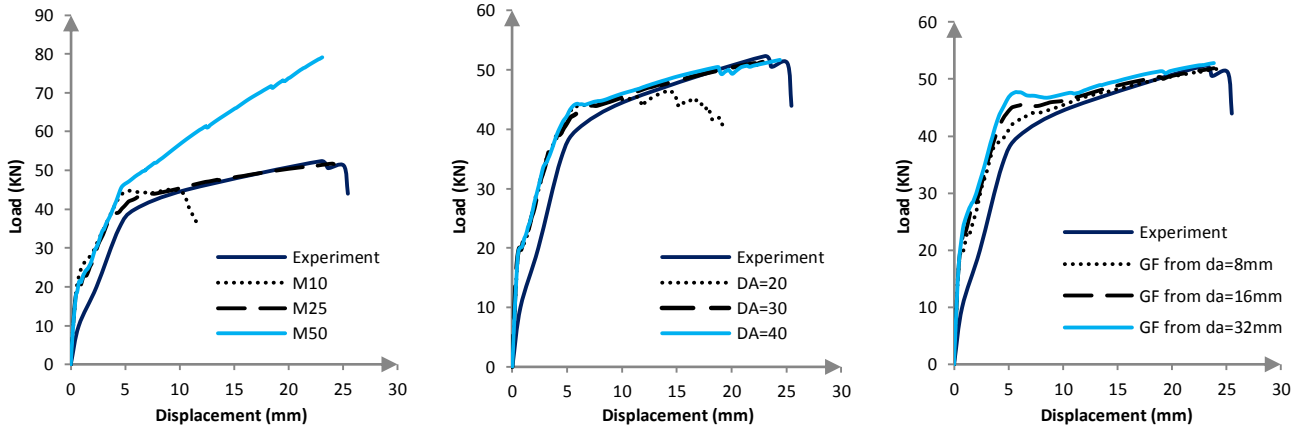

a) Mesh sensitivity b) Dilation angle sensitivity c) Fracture energy sensitivity

Fig. 12. Numerical results for Test Case 3.

Table 4 compares the experimental yield loads and deflections with those obtained from the finite element analysis for three test cases. As can be seen in Table 4, the predicted yield load and deflections for Test Case 1 and Test Case 2 is nearly same with experimental results. However, yield load is %7 higher than experimental result for the Test Case 3. According to these results, proposed finite-element model proves its capability to accurately predict the load–deflection relationships of the reinforced concrete beams.

Table 4. Comparison of results.

	Test Case 1		Test Case 2		Test Case 3	
	Yield Load (kN)	Deflection (mm)	Yield Load (kN)	Deflection (mm)	Yield Load (kN)	Deflection (mm)
Experiment	70	13.65	21.2	10	40	5.93
Finite Element	70.9	13.64	21.4	9.4	42.8	5.95
Numeric/Experiment	1.01	1.00	1.00	0.94	1.07	1.00

6. Conclusions

Three different experimental tests are verified by using modeling strategies explained in the previous sections. Results show that experimentally observed loading trends and magnitudes for entire loading range of RC beams can be captured by employing CDP modeling approach. Basically mesh density, dilation angle and concrete fracture energy are calibrated to develop modeling strategies. It is obvious that if material properties and geometrical information about real test are given in detail then numerical models give better results than those with missing information. Also this study proves that defining damage parameters for compression behavior with proposed equation gives satisfactory results. But this equation can be improved with real test results for further investigations.

References

ABAQUS (2008). User's Manual, Version 6.8, Hibbitt, Karlsson&Sorensen, Inc., Pawtucket, Rhode Island, USA.

ACI 318-99 (1999). Building Code Requirements for Structural Concrete and Commentary. American Concrete Institute, Detroit, MI.

Arduini M, Di Tommaso A, Nanni A (1997). Brittle failure in FRP plate and sheet bonded beams. *ACI Structural Journal*, 94 (4), 363-70.

Benjeddou O, Ouezdou BM, Bedday A (2007). Damaged RC beams repaired by bonding of CFRP laminates. *Construction and Building Materials*, 21(6), 1301-1310.

Chen WF (1982). Plasticity in Reinforced Concrete, XV. New York: McGraw-Hill, 474.

Comite Euro-International du Beton (1993). CEB-FIP Model Code 1990 (CEB-FIP MC90). *Bulletin D'Information*, No. 215, Lausanne.

Coronado CA, Lopez MM (2006). Sensitivity analysis of reinforced concrete beams strengthened with FRP laminates. *Cement and Concrete Composites*, 28(1), 102–114.

Hillerborg A, Modeer M, Petersson PE (1976). Analysis of crack formation and crack growth in concrete by means of fracture mechanics and finite elements. *Cement and Concrete Research*, 6, 773–782.

Jason L, Pijaudier-Cabot G, Huerta A, Ghavamian S (2004). Damage and plasticity for concrete behavior. *European Congress on Computational Methods in Applied Sciences and Engineering*, Jyväskylä.

Lubliner J, Oliver J, Oller S, Onate E (1989). Plastic-damage model for concrete. *International Journal of Solids Structures*, 25(3), 299–326.

Rots JG (1988). Computational Modeling of Concrete Fracture. *Ph.D. thesis*, Delft University of Technology, Delft, Netherlands.

Sharif A, Al-Sulaimani GJ, Basunbul IA, Baluch MH, Ghaleb BN (1994). Strengthening of initially loaded reinforced concrete beams using FRP plates. *ACI Structural Journal*, 91(2), 160-16.